An optical emission spectroscopic study of laser-induced Zn and ZnO plasma

Benjamin S. Truscott

A thesis submitted to the University of Bristol in accordance with the requirements for the award of the degree of Doctor of Philosophy in the Faculty of Science

School of Chemistry

March 2013

ABSTRACT

Laser-induced Zn and ZnO plasma plumes, produced using nanosecond optical pulses in the irradiance range ≈ 1–10 GW/cm^2, have been investigated by time-resolved imaging optical emission spectroscopy. The intensity and spatial distribution of emission from electronically excited atomic and ionic species were monitored, both *in vacuo* and in the presence of oxygen, and the influence of varying irradiance on these properties was studied. Quasi-Maxwellian velocities were observed for (Zn^{0})* and (Zn^{1+})* (the latter Coulomb-shifted by ≈ 20 eV), and emission intensity for these species scaled sub-linearly with irradiance, suggesting that ablation proceeds primarily *via* a field-assisted phase explosion-like mechanism for both target materials despite their dissimilar thermal and electronic properties. (Zn^{2+})* and (Zn^{3+})* were also observed, with these species possessing surprisingly large translational kinetic energies of up to ≈ 1.5 keV, in addition to substantial (≫ 10 eV) electronic excitation, placing them near to their respective ionization limits. This was understood to be the result of electron impact ionization within a plasma strongly heated by inverse bremsstrahlung absorption, coupled with a dynamic Coulomb acceleration process driven by thermally-induced space charge. Emission lifetimes exceeded those expected given the relevant Einstein *A*-coefficients (where known) and did not depend on the particular transition chosen for analysis, indicating continuing excitation by collisional energy/charge transfer from the higher ions even after laser irradiation had ceased. Ambient oxygen was found to promote the collisional and/or reactive quenching of (Zn^{2+})* and (Zn^{3+})*, while also scavenging hot electrons and thereby preventing the formation of a space charge layer, thus reducing the degree of Coulomb acceleration imparted. Evidence of electron-ion recombination was also noted in the presence of the background gas, which interestingly resulted in the enhancement of emission in particular due to a two-electron, one-photon transition of (Zn^{1+})* analogous to that of (Cd^{1+})* responsible for 325 nm HeCd laser emission, which otherwise was only weakly observed.

ACKNOWLEDGEMENTS

The experience of a graduate student is an uncommon one, in that we each enter into an environment and a discipline both of which have for us been hitherto almost unknown, equipped with an desire for knowledge and yet only partly conscious of the extent of our self-assured naivety. The initial shock of encountering our own limitations is scarcely tempered by the realization, not only in an abstract philosophical sense but also as a practical reality, that the idealistic notions of truth or understanding have no meaning for the scientific enterprise, and that it is through doubt, not confidence, that empirical progress is achieved. Firstly, therefore, I wish to express my deepest gratitude to Mike for a great many perceptive suggestions and productive discussions, as well as for all of the insight, experience, honest advice, understanding, and reassurance that he has offered me as part of his magnanimous supervision. Particular thanks are also due to Colin for his extremely generous extended loan of the spectrograph and intensified CCD, without which abundant high-quality experimental data, only part of which is presented here, would not have been available at a time when usable results were badly needed.

I have often thought it a pleasant sociological curiosity that, on joining a research group, one arrives, through common objectives and shared experience, among compatriots; yet, several years later, although almost none of the original cohort might remain, the feeling is of having constantly been surrounded by friends. Thus, I would like to thank my colleagues, past and present, all of whom I do indeed consider friends, for the opportunity to collaborate on many fascinating problems; for interesting, and occasionally heated, discussions; and for their enthusiastic support and companionship in general.

AUTHOR'S DECLARATION

I declare that the work presented in this thesis was carried out in accordance with the requirements of the University's Regulations and Code of Practice for Research Degree Programmes, and that it has not been submitted for any other academic award at this or any other university. Except where specifically indicated, this work is the author's own, and was carried out between October 2008 and May 2012 under the supervision of Professor M. N. R. Ashfold, FRS. All opinions expressed herein are those of the author and should not be taken to represent the views of any other party.

SIGNED: DATE:

Science does not rest upon solid bedrock. The bold structure of its theories rises, as it were, above a swamp. It is like a building erected on piles. The piles are driven down from above into the swamp, but not down to any natural or 'given' base; and when we cease our attempts to drive our piles into a deeper layer, it is not because we have reached firm ground. We simply stop when we are satisfied that they are firm enough to carry the structure, at least for the time being.

Karl Popper, in *The Logic of Scientific Discovery*

CHAPTER 1: INTRODUCTION

1.1 IONIZED GASES AND PLASMA

The term *plasma*, in the sense of an ionized gas in which, at long range, the positive and negative charges are (nearly) balanced, was first used in 1928 by Langmuir in discussing the thermalization of initially monochromatic electron beams on passing through such a medium.[1] That is, the thermal energy of a plasma is of the same order as the ionization potential of the constituent atoms, so that, in a hierarchy of states of matter differentiated according to their characteristic kinetic energies, plasma occupies the fourth position after the solid, liquid, and (neutral atomic or molecular) gas phases.[2] Complete ionization is not, however, a defining feature of plasma: neither the absence of mutually bound electrons and nuclei, nor even that of neutral species, are necessary attributes, although both of these situations are possible.

Plasma is ubiquitous on astrophysical scales; indeed, the majority of extant matter is found in this state, with the physics of (for example) the solar photosphere being in some sense comparable to that of the Earth's magnetosphere, despite temperature and density varying over many orders of magnitude between these situations. Plasma properties and behaviour are governed instead primarily by short-range Coulomb interactions, which however are screened out at long distance due to charge mobility.[a] Since electron mobility is normally much greater than that of the ions, the former tends to dominate in practice. The screening length, or Debye length, is thus given by

$$\lambda_{\mathrm{D}} = \sqrt{\frac{\varepsilon_0 \hat{T}}{n_{\mathrm{e}} e}} \qquad \text{Equation 1.1}$$

where ε_0 is the vacuum permittivity, e is the electron charge, and n_{e} and $\hat{T}$ are, respectively, the number density of free electrons and the electron temperature in eV.

[a] It should be noted that magnetic fields, which clearly are not screened by the same mechanism, are still able to influence collective behaviour on large length scales. Although this is important in many cases, we assume here both that no external magnetic field acts on the plasma and that no current flows within it.

1.2 LASER-INDUCED PLASMA

The archetypal method for the creation of artificial plasma is the production of an electric discharge within a suitably chosen medium (most typically a gas). Dielectric breakdown of insulators can in general be achieved by the application of a sufficiently strong electric field, although the detailed ionization mechanism is highly material-specific.[b] Both static and time-varying fields can be employed for this purpose, with d.c. and radio frequency (RF) excitation representing the most common regimes in practice, although electric discharges may also be produced using fields of significantly higher (e.g. optical) frequencies. Pulsed lasers provide a straightforward means of access to very high excitation power densities ($\gtrsim 1$ GW/cm^2), so that the electric field under which breakdown occurs can readily be made extremely intense. As a result, laser-induced plasma may be obtained not only in gaseous media but also in solids and liquids, including those of relatively high dielectric strength, such as benzene. For a laser beam with intensity (or irradiance) I, the electric field amplitude is given by[3]

$$|E| = \sqrt{\frac{2I}{n\varepsilon_0 c}} \qquad \text{Equation 1.2}$$

where n is the refractive index of the substrate through which the beam propagates, with typically $1 \leq n \leq 3$. For $n \approx 2$ (as for e.g. ZnO at 532 nm[4]) and with a modest irradiance of $I \approx 1$ GW/cm^2 we have $|E| \approx 10^5$–10^6 V/cm, which already exceeds the dielectric strength of almost all materials. Furthermore, yet stronger fields ($\geq 10^8$ V/cm) are achievable with ultra-short (sub-picosecond) pulsed lasers, these being sufficient to cause the breakdown of strongly nonpolarizable solids, e.g. diamond (dielectric strength $\approx 10^7$ V/cm) and perhaps even conductive media such as bulk metals.[c] Several different modes of interaction between the laser field and

[b] While the dissipation of the potential energy of the applied field into the (conductive) plasma may subsequently heat the latter sufficiently that thermal ionization becomes significant (or even dominant) overall, we first concern ourselves here with the initial transition to the plasma state.

[c] As pointed out by Rukhadze and Yusupaliev[5], an exceedingly strong electric field is required for dielectric breakdown to dominate over avalanche or thermal ionization processes in metals. Indeed, both Hashida *et al.*[6] and Bulgakova *et al.*[7] have argued that in practice this process is facilitated by field enhancement at the metallic surface even under conditions of very high irradiance

electrons present in the discharge medium are responsible for plasma formation, as will be discussed in the following paragraphs.

Broadly, breakdown is initiated by, and proceeds through, the production of free charge carriers in dielectric materials additional to those due to defects or thermal fluctuations. It is important to note that valence electrons can be excited either directly into the ionization continuum or, alternatively, into relatively weakly bound (delocalized) states in the conduction band where they couple strongly to the laser field and may undergo inverse bremsstrahlung absorption and subsequent collisional energy transfer (Joule heating). Here we explicitly distinguish between conduction band to continuum, valence band to conduction band, and valence band to continuum transitions, only the first of which (corresponding to photoelectron emission) is applicable to metals. In any case, the principal modes of excitation are single- or multiphoton absorption and impact with pre-existing free electrons (whether present in the conduction band or entirely unbound) that are accelerated in the applied field. Clearly, if irradiation is sustained for sufficiently long (in practice, $\gtrsim 1$ ps for most dielectrics), these electrons may themselves be accelerated to sufficiently high energies as to give rise to further excitations, so that the initial population is eclipsed by that due to avalanche multiplication. In general, all of these processes can occur simultaneously, with each operating either independently or synergistically with one or more others. As a result, the character of the breakdown process cannot easily be assigned *a priori*, since the probability of ionization *via* each mechanism depends on the properties of both the exciting radiation (irradiance, frequency, and pulse duration) and the material (in particular the band gap, density of states in the conduction band, and work function).

Epifanov[8] has reviewed avalanche ionization as it applies to the formation of laser-induced plasma, noting that the critical electric field strength for dielectric breakdown *via* this mechanism is proportional to the laser frequency (for a given material) and essentially independent of pulse duration above ≈ 1 ns. Pronko *et al.*[9] have examined the wavelength (786 and 1064 nm) and pulse duration (80 fs–9 ns)

($\approx 10^{20}$ W/cm^2). Dielectric breakdown of bulk conductors therefore represents a somewhat exotic phenomenon and, for that reason, will not be considered further in the present work.

dependence of the irradiance (hence electric field strength) required to induce this process in silicon, in order to characterize the ionization process as primarily due to either multiphoton absorption or avalanche multiplication. The breakdown threshold was found to increase with frequency, and these authors therefore concluded that avalanche ionization predominates under such conditions. The electrons responsible for seeding the process were assumed in this case to be formed by one-photon band-to-band transitions, since both of the photon energies investigated ($\hbar\omega$ = 1.17 and 1.58 eV) exceeded the Si band gap (E_{gap} = 1.12 eV). Furthermore, the threshold field was seen to increase with decreasing pulse duration, as expected in the short- and ultrashort-pulse regime where the finite ionization time cannot be neglected. However, it should be noted that the strength of the laser field decreases more rapidly for longer pulses than is compensated by any reduction in the breakdown threshold, so that the critical *energy density* (i.e. fluence) still increases with pulse length. As pointed out by Pronko *et al.*, laser-induced breakdown was also found by Du *et al.*[10] to proceed by an avalanche mechanism for deep sub-bandgap excitation ($\hbar\omega$ = 1.59 eV vs. $E_{gap} \approx 9$ eV) of SiO_2, with the initial population of conduction band electrons then resulting from either multiphoton absorption or thermal excitation, depending on the laser pulse duration.

In contrast, Vaidyanathan *et al.*[11] considered theoretically the continuous-wave irradiation of some alkali halides (E_{gap} = 8.6–13.6 eV) at several wavelengths between 355 and 1064 nm ($\hbar\omega$ = 1.17–3.49 eV), finding that, in general, both multiphoton and avalanche excitation processes are applicable, with the dominant mechanism depending somewhat sensitively on the excitation frequency. In particular, they observed that the probability of breakdown due to multiphoton absorption (calculated following Keldysh[d]) exceeds that due to avalanche multiplication for the near-resonant case of $\hbar\omega \approx E_{gap}/4$, finding reasonable agreement with experiment despite the requirement for four-photon absorption. Since the Keldysh formalism predicts significant enhancement of the multiphoton ionization probability due to resonance with intermediate states (here, the lowest-lying conduction band), this conclusion

[d] The formula for the multiphoton absorption probability, derived by Keldysh according to a theoretical model of valence- to conduction-band transitions in direct-gap crystals, is straightforward to evaluate but quite complicated in form. The reader is hence referred to either the account given by Vaidyanathan *et al.*[11] or the original work by Keldysh.[12]

probably generalizes to $E_{gap} \approx n\hbar\omega$, at least for $n \in \{1, 2, 3\}$. Resonances with excitonic (e.g. defect) states may also contribute, and the situation whereby $E_{gap}/2 < \hbar\omega < E_{gap}$ has been studied in some detail for cubic crystals by Mahan,[13] who found that the multiphoton absorption probability then scales linearly with frequency for semiconductors and quadratically for wide-bandgap materials.

A quantitative distinction between the dielectric, conductive, and plasma states can be made based on the free electron density. Efficient inverse bremsstrahlung absorption (IBA) of power by a plasma from an oscillating electric field is possible only with n_e close to a critical value, which may be calculated for a particular laser wavelength from the (electron-dominated) *plasma frequency*,

$$\omega_p = \sqrt{\frac{n_e e^2}{m_e \varepsilon_0}} \qquad \text{Equation 1.3}$$

where m_e is the mass of the electron. Setting $\omega_p = \omega = 2\pi c/\lambda$, we obtain for $\lambda = 355$ nm the result that $n_e = 8.85 \times 10^{21}/\text{cm}^3$. It should be noted that this value is much smaller than the typical conduction-band electron density in metals; for example, $n_e = 1.32 \times 10^{23}/\text{cm}^3$ for solid Zn. In general, therefore, dense conductors such as metals and (especially) highly ionized solid-density plasmas possess high reflectivity at optical frequencies and undergo absorption of radiation by Joule heating or plasma IBA (which are physically analogous processes) only at the surface. The skin depth ($1/e$ penetration distance) for radiation of angular frequency ω has been given by Conrads and Schmidt[14] as

$$\delta = \sqrt{\frac{2\rho}{\mu\omega}} = \frac{c}{\omega_p}\sqrt{\frac{2\nu_e}{\omega}} \qquad \text{Equation 1.4}$$

where ρ is resistivity, μ is absolute magnetic permeability (with $\mu \approx \mu_0$ for most non-ferromagnetic materials), and ν_e is the electron collision frequency. Again, for metallic Zn ($\rho = 5.964 \times 10^{-8}\ \Omega\cdot\text{m}$), we have $\delta = 4.23$ nm at $\lambda = 355$ nm, while conversely δ is large for insulators (e.g. ZnO), corresponding to the case of small free electron density and thus high optical transmission. Plasma clearly occupies an

intermediate position on this scale, with Vaidyanathan *et al.* choosing $n_e = 10^{18}/cm^3$ as their criterion for dielectric breakdown. Conrads and Schmidt have also given an expression for the volumetric power absorption, i.e.

$$\frac{P_{abs}}{V} = \frac{n_e}{2}\frac{e^2}{m_e \nu_e}\frac{\nu_e^{\,2}}{\nu_e^{\,2} + \omega^2}|E|^2 \qquad \text{Equation 1.5}$$

which indicates that significant coupling to the laser field can be expected only when ν_e is large,[e] as well as showing that, in general, the optical density (opacity) is greater at longer wavelengths. However, combining Equation 1.2 and Equation 1.5 with the additional relation

$$n = \sqrt{1 - \frac{\omega_p^{\,2}}{\omega^2}} \qquad \text{Equation 1.6}$$

yields

$$\frac{P_{abs}}{V} = \frac{\omega}{c}\frac{n_e e^2}{\sqrt{m_e \varepsilon_0}}\frac{\nu_e}{\nu_e^{\,2} + \omega^2}\sqrt{\frac{1}{m_e \varepsilon_0 \omega^2 - n_e e^2}}I \qquad \text{Equation 1.7}$$

which clearly (cf. Equation 1.3) requires $\omega > \omega_p$ in order to be well defined, thus indicating a definite lower limit for the allowable excitation frequency and signifying more clearly the reflection of the incident radiation when this condition is not fulfilled.

To model the scaling of this absorption with laser wavelength and irradiance, we introduce some simplifying assumptions that are not wholly realistic (except perhaps for the sparse outer extremities of the plasma, where the irradiance and ionization fraction are greatest; see later) but which allow the plasma pressure and volume to be removed from consideration for the time being. Setting the plasma pressure equal to the opposing radiation pressure, i.e.

[e] P_{abs} is maximized with $\nu_e \approx \omega/(2\pi)$. For visible and UV wavelengths, this frequency is around 50–100 THz.

$$p = n_e e\hat{T} = \frac{I}{c} \qquad \text{Equation 1.8}$$

and taking the plasma to be fully ionized and the electron–ion collision rate to be[15]

$$\nu_e \approx \frac{e^{5/2} n_e}{32\pi\varepsilon_0^{\,2}\sqrt{2m_e\hat{T}^3}} \qquad \text{Equation 1.9}$$

we find that, to a first approximation,

$$P_{abs} \sim N_e I^2 \lambda^2 \hat{T}^{-5/2} \qquad \text{Equation 1.10}$$

where N_e is the number of electrons present at a certain location within the plasma that is subject to irradiance I. This shows a strong dependence on (the reciprocal of) electron temperature, and a somewhat weaker scaling with wavelength; however, it is important to note that the electron temperature is itself a function of (integrated) irradiance, and therefore Equation 1.10 describes the relative importance of the parameters only in a local and instantaneous sense. It should also be acknowledged that the confinement implied by Equation 1.8 is rather tenuous in reality (if it exists at all), since the radiation pressure encountered in this work (33.4 kPa GW^{-1} cm^{-2}, i.e. ≈ ⅓–3 atm for I = 1–10 GW/cm^2) provides only very limited resistance to the expansion of the plasma. For example, with an electron temperature of between 1 and 10 eV, the radiation pressure at I = 5 GW/cm^2 is balanced by the outward pressure for a free electron density of 10^{17}–10^{18}/cm^3. Given that the initial Zn atom density (as will be seen later) probably exceeds 10^{21}/cm^3, this figure may easily be exceeded even in a weakly ionized plasma. Moreover, if thermal equilibrium is assumed actually to be achieved, the plasma pressure must reflect that of a gas of at least 10^{21} particles/cm^3 at a temperature of up to 10 eV. Since the resulting values, i.e. potentially greater than 1 GPa, are far in excess of any realistic estimate of the radiation pressure, significant departures from the scaling given by Equation 1.10 are to be expected in regions of high electron density and/or temperature.

Mora[16] has given a more rigorous (though also rather involved) description, finding that, averaged over the entire (expanding) plasma, the absorption fraction goes as $I\lambda^4$ rather than $I\lambda^2$. The remaining discrepancy with respect to the exponent of I is not significant, however: we note that since

$$I = \frac{P}{A} \qquad \text{Equation 1.11}$$

where A is the irradiated area, Equation 1.10 may also be written, under approximation to a homogeneous plasma, as

$$\frac{P_{\text{abs}}}{P} = \alpha \sim \frac{N_{\text{e}}}{A} I\lambda^2 \hat{T}^{-5/2} \qquad \text{Equation 1.12}$$

where α is the absorption coefficient and N_e/A is the areal electron density.

More importantly, very different predictions arise after considering the competing electron–neutral (e–n) inverse bremsstrahlung process and the influence of IBA on the electron temperature, although a useful analytical treatment of these effects is most likely unfeasible. Bogaerts and Chen[17] have presented a detailed numerical model that demonstrates that e–n IBA in the dense plasma near the target surface always dominates over absorption *via* the electron–ion (e–i) mechanism, so that in fact the distinction between the latter scaling with λ^2 or λ^4 becomes unimportant overall.[f] Rather, these authors find that, due to the overriding influence of stimulated e–n bremsstrahlung emission, the total absorbed fraction of laser radiation is (roughly) *inversely* proportional to wavelength, such that at $\lambda = 1064$ nm there is no longer any net e–n IBA. Figure 20 from ref. 17, duplicated below as Figure 1.1, shows the percentage of incident radiation absorbed due to e–n/e–i IB and photoionization (PI) processes at several wavelengths and over an irradiance range typical for laser-induced plasma. Nonetheless, as we shall see later, time- and volume-averaged absorption coefficients such as those discussed here are not sufficient for a comprehensive description of the coupling of laser energy into the plasma, and

[f] Indeed, Bogaerts and Chen suggest yet another relationship, taking the e–i IBA coefficient to be proportional to λ^3.

several regimes exist in practice due to the very large ionization fraction, density, and temperature gradients involved.

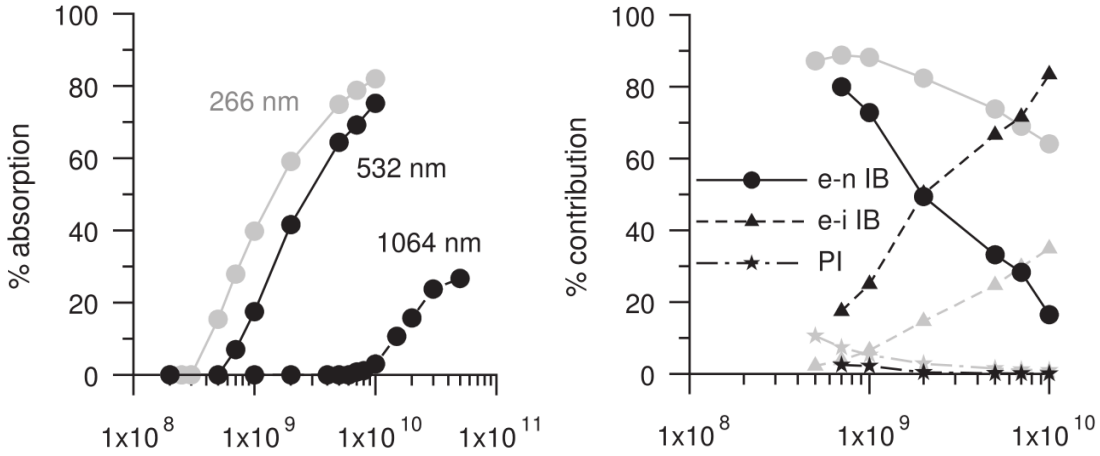

Figure 1.1: Reproduction of Figure 20 from ref. 17 describing the coupling of incident radiation into laser-induced plasma according to the model of Bogaerts and Chen. Left: overall percentage absorption. Right: contributions to the total absorption by inverse bremsstrahlung and photoionization processes at 266 and 532 nm. At 1064 nm, e–i IB represents the sole absorption mechanism, which therefore is not shown graphically. The horizontal scale is irradiance in W/cm^2.

1.3 ATOMIC SPECTROSCOPY

1.3.1 THE SPECTRA OF HYDROGENIC ATOMS

Despite its formulation on an empirical basis prior to the ascendancy of modern quantum mechanics, the Bohr model accounts reasonably accurately for the spectra of one-electron atoms, and, by virtue of its simplicity, often represents a useful first-order approximation even in cases for which the semiclassical theory cannot be expected to hold in detail. Here, we follow Herzberg's presentation of the latter,[18] putting $\hat{e} = e/\sqrt{4\pi\varepsilon_0}$ (i.e., using Gaussian units) for brevity. The electron is assumed to occupy one of an infinite series of non-decaying circular orbits about the nucleus. For a stable classical orbit, we have the balance of forces

$$\frac{Z\hat{e}^2}{r^2} = m_e \frac{v^2}{r} \qquad \text{Equation 1.13}$$

where Z is the formal nuclear charge, m_e and $\hat{e}$ are the mass and (Gaussian) charge of the electron, respectively, and v and r are the orbital velocity and radius. Angular momentum quantization in units of $\hbar = h/(2\pi)$, with h being Planck's constant, leads to the introduction of the *principal quantum number*, n:

$$m_e v r = n\hbar \qquad \text{Equation 1.14}$$

where $n \in \mathbb{N}$. Solving Equation 1.13 and Equation 1.14 for v and r, we obtain

$$v = \frac{Z\hat{e}^2}{n\hbar} \qquad \text{Equation 1.15}$$

$$r = \frac{n^2\hbar^2}{m_e Z\hat{e}^2} \qquad \text{Equation 1.16}$$

so that the total (potential plus kinetic) energy of the orbiting electron is given by

$$\begin{aligned} E &= -\frac{Z\hat{e}^2}{r} + \frac{m_e v^2}{2} \\ &= -\frac{Z^2\hat{e}^4 m_e}{2n^2\hbar^2}. \end{aligned} \qquad \text{Equation 1.17}$$

The familiar Rydberg formula is then obtained from the difference in wavenumber between two terms having principal quantum numbers n_1 and n_2:

$$\begin{aligned} \tilde{\nu} &= \frac{1}{c}\frac{\omega}{2\pi} \\ &= \frac{1}{c}\frac{(E_{n_2} - E_{n_1})/\hbar}{2\pi} \\ &= R_\infty Z^2\left(\frac{1}{n_1^{\,2}} - \frac{1}{n_2^{\,2}}\right) \end{aligned} \qquad \text{Equation 1.18}$$

where $R_\infty = m_e\hat{e}^4/(4\pi\hbar^3 c) = m_e e^4/(8\varepsilon_0^{\,2}h^3 c) = 109\,737.316\ \text{cm}^{-1}$ is the limiting value of the Rydberg constant for an infinitely massive nucleus. For light nuclei, a small correction to R_∞ may be accomplished through substitution of the reduced mass of the electron-nucleus system, $\mu = m_e m_n/(m_e + m_n)$, in place of the electron mass m_e.

As Herzberg notes, Sommerfeld[19] was able to refine the Bohr model to account adequately for hydrogen fine structure and the spectra of the alkali metals within the semiclassical formalism. However, a complete and self-consistent treatment became possible only later through the application of wave mechanics *via* the Schrödinger equation, from which the essential results may be derived directly and without further assumptions. The latter is an eigenvalue problem posed in the nonrelativistic case as follows:

$$\hat{H}\Psi = (\hat{T} + \hat{V})\Psi = \left[\frac{\hat{p}^2}{2\mu} + V(\mathbf{x})\right]\Psi = E\Psi \qquad \text{Equation 1.19}$$

Here, $\hat{H}$ is the Hamiltonian operator, having kinetic and potential energy components $\hat{T}$ and $\hat{V}$ (with $\hat{p} = -i\hbar\nabla$ being the momentum operator, wherein ∇ is the gradient). The energies $E = E_i$ and the corresponding wavefunctions $\Psi = \Psi_i(\mathbf{x})$ are then obtained directly from the spectrum (i.e., as the eigenvalues and eigenfunctions, respectively) of $\hat{H}$. Equation 1.19 is separable (in spherical coordinates) for the one-electron potential $V(\mathbf{x}) = V(r) = -Z\hat{e}^2/r$, and admits closed-form solutions for E and $\Psi = \Psi(r, \theta, \phi)$ that are labelled by the quantum numbers n, l, and m. The important results (the derivation of which is somewhat involved and so will not be reproduced here) are that E is as given in Equation 1.17 and depends only on n, and the angular momentum quantum numbers l and m are introduced *via* the wavefunction,

$$\Psi_{nlm}(r, \theta, \phi) = R_n^l(r) \cdot Y_l^m(\theta, \phi) \qquad \text{Equation 1.20}$$

where the angular part is an orthonormal (Laplace) spherical harmonic Y_l^m and the radial part is

$$R_n^l(r) = \sqrt{\frac{(n-l-1)!}{2n(n+l)!}}\left(\frac{2Z}{na_0}\right)^{3/2} \exp\left(-\frac{Zr}{na_0}\right)\left(\frac{2Zr}{na_0}\right)^l L_{n-l-1}^{2l+1}\left(\frac{2Zr}{na_0}\right)$$

Equation 1.21

with $L_j^k(x)$ being the j^{th} associated Laguerre polynomial in x with parameter k,[g] and $a_0 = \hbar^2/(\mu e^2)$ the atomic unit of length (Bohr radius).[20] By analogy with the semiclassical construction, n is related to the mean distance of the electron from the nucleus; indeed, the expectation value

$$\langle r \rangle = \int_0^\infty r R_n^l(r)^2 r^2 dr = \frac{1}{2}[3n^2 - l(l+1)]\frac{a_0}{Z} \qquad \text{Equation 1.22}$$

is, for the $l = 0$ case, simply Equation 1.16 multiplied by a constant factor. The l and m quantum numbers, on the other hand, are associated with the total angular momentum possessed by the electron (l) and its projection along the z-axis (m); these have no parallel in the Bohr model, wherein the angular momentum depends only on n by Equation 1.14. The leading term of Equation 1.21 is well-defined only for $l \in \{0, \ldots, n-1\}$, while it can be shown that, for the spherical harmonics Y_l^m, the angular momentum vector $\mathbf{l}$ is constrained such that

$$|\mathbf{l}| = \sqrt{l(l+1)}\hbar \qquad \text{Equation 1.23}$$

$$\mathbf{l} \cdot \hat{\mathbf{k}} = m\hbar \qquad \text{Equation 1.24}$$

from which it follows that $m \in \{-l, -l+1, \ldots, l\}$.

Given the foregoing discussion, it is clear that the absorption or emission of a photon, which possesses angular momentum equal to $\sqrt{2}\hbar$ (i.e., an effective l quantum number of 1), may induce a change in l and m of at most ±1, while no such restriction exists on the change in n subject to the photon energy satisfying Equation 1.18. An additional condition arises, however, due to a symmetry constraint: Y_l^m is symmetric with respect to the coordinate inversion $x\hat{\mathbf{i}} + y\hat{\mathbf{j}} + z\hat{\mathbf{k}} \rightarrow -x\hat{\mathbf{i}} - y\hat{\mathbf{j}} - z\hat{\mathbf{k}}$ (i.e., has even parity) for l zero or even, and antisymmetric (having odd parity) otherwise. Since the parity of the photon is odd, its absorption or emission must change the parity of the atomic wavefunction, but the product of the initial, photon, and final wavefunction parities must be even in order for the transition dipole moment

[g] Sobelman employs an uncommon definition for the associated Laguerre polynomials, so the expression he provides differs slightly from that given here.

$$\boldsymbol{\mu} = \int \Psi^{*}_{n'l'm'} \hat{\boldsymbol{\mu}} \Psi_{nlm} \, d\tau \qquad \text{Equation 1.25}$$

to be nonzero (where the parity of the dipole moment operator $\hat{\boldsymbol{\mu}}$ is the same as that of the photon).[h] We thus have the further requirement that l must change by ±1, with $\Delta l = 0$ disallowed. In summary, then, the selection rules for electric dipole transitions are: $\Delta n = \pm x$, $x \in \mathbb{Z}$ arbitrary; $\Delta l \in \{-1, +1\}$; and $\Delta m \in \{-1, 0, +1\}$.

Finally, it should be noted that the dependence of the term energy only on n is an unphysical artefact of the nonrelativistic theory reviewed here; a perturbative treatment of special relativity, for example as given by Sobelman (ref. 20, §1.3.1, p. 10), is sufficient to show that the degeneracy with respect to l holds only approximately.

1.3.2 POLYELECTRONIC ATOMS

In the preceding section, we saw that the spectrum of a hydrogenic atom is fully described in terms of the values of the three quantum numbers of the electron, i.e. n, l, and m. For polyelectronic species, however, perturbative incorporation of relativistic effects within the framework of the Schrödinger equation is no longer sufficient to account for the term energies, a correct description of which requires the fully relativistic Dirac equation.[i] Since the formulation of the latter is quite involved, we note only that its exact solution is possible for one-electron systems, introducing an additional quantum number, s, which is related to the spin angular momentum vector by $|\mathbf{s}| = \sqrt{s(s+1)}\hbar$. Since $s = ½$ for an electron, with no other values possible, the projection $m_s = \boldsymbol{s}\cdot\hat{\mathbf{u}}/\hbar \in \{-½, +½\}$ (where $\hat{\mathbf{u}}$ is the unit vector defining the spin axis) is both necessary and sufficient for a complete description of $\boldsymbol{s}$. We hence refer to the z-projection of the orbital angular momentum as m_l and have, for each electron, the four quantum numbers n, l, m_l, and m_s, taking care to note that m_l and m_s refer to projections along axes that are not necessarily coincident.

[h] Although a detailed discussion of this topic is beyond the scope of the present work, the reader is directed to the comprehensive treatments given by Sobelman[20] and Corney.[21]

[i] Strictly, this applies to hydrogenic atoms also; neglecting the spin of the electron is valid only under the approximation of an infinitely massive nucleus and absent external electromagnetic fields.

Neither the Schrödinger nor the Dirac equation admits closed form solutions for polyelectronic systems in general because of the nonseparability of the associated many-body Hamiltonian. Nonetheless, the wavefunction in such cases (which can be obtained numerically) is approximately representable as a product of orthogonal two-electron wavefunctions (orbitals) that are themselves products of one-electron wavefunctions having the same n, l, and m_l quantum numbers but also depending on the spin coordinate **s** (or, equivalently, m_s). If spin-orbit coupling can be neglected, the spatial dependence of the orbitals remains essentially as given by Equation 1.20, but we have the additional postulate (due to the Pauli exclusion principle) that the total wavefunction is antisymmetric with respect to particle interchange. Since the spatial part of each orbital is symmetric, the spin part must be antisymmetric, and therefore two electrons may simultaneously occupy a given orbital only if their spins are antiparallel. The degeneracy with respect to l indicated by Equation 1.17 is strongly broken in polyelectronic atoms and, starting from ($n = \mathcal{N}$, $l = \mathcal{L}$), the terms are ordered by energy approximately as ($\mathcal{N}+1$, $\mathcal{L}-1$), …, ($\mathcal{N}+\mathcal{L}$, 0), ($\lceil \mathcal{N}/2 \rceil + 1$, $\lfloor \mathcal{N}/2 \rfloor$) (etc.).

The ordering by **l** and **s**, however, is more complex and requires consideration of the manner in which the angular momenta of the individual electrons combine to yield the total angular momentum of the atom or ion. In this regard, l and the projections m_l and m_s are insufficient, since they do not account for the relative orientation of **s** between different electrons, nor its relationship to **l**. Thus, in addition to the total orbital and spin angular momentum quantum numbers L and S, which are given by

$$\mathbf{L} = \sum_i \mathbf{l}_i \qquad \text{Equation 1.26}$$

$$\left|\mathbf{L}\right| = \sqrt{L(L+1)}\hbar \qquad \text{Equation 1.27}$$

(and similarly for **s**), we require the quantum number J associated (analogously to Equation 1.27) with the total angular momentum $\mathbf{J} = \mathbf{L} + \mathbf{S}$;[j] the permitted values of

[j] The expression $\mathbf{J} = \mathbf{L} + \mathbf{S}$ (LS coupling) is an approximation valid only in the limit of weak spin-orbit interaction. In other cases, we have instead $\mathbf{j}_i = \mathbf{l}_i + \mathbf{s}_i$, with **J** being the vector sum of the $\mathbf{j}_i$ (jj

the latter are $J \in \{L + S,\ L + S - 1,\ \ldots,\ |L - S|\}$. The ordering in energy of several terms having different values of L, S, and J may be estimated according to Hund's rules:[22]

1. Spin correlation (due to the Pauli exclusion principle) imposes a significant energy penalty on electrons with equal n, l, and m_l quantum numbers, and this is minimized for the term having the largest total spin angular momentum quantum number S.
2. The contribution of electron-electron repulsion to the term energy is usually reduced for larger L.
3. If sufficient electrons are present in the highest occupied *shell* (defined by n and l) to account for less than half of the available combinations of m_l and m_s, the term energies increase with J; otherwise, the opposite applies.

It should be noted, however, that the second rule is a heuristic that achieves only limited accuracy for excited states, while m_l and m_s are not strictly meaningful quantum numbers in this context, being valid only within the orbital approximation.

The selection rules for one-electron dipole transitions in polyelectronic species have been addressed in detail by Sobelman (ref. 20, §2.2.4, pp. 26–27/§9.2, pp. 205–216). In summary, we require a change in parity of the atomic wavefunction and that $\Delta J \in \{-1, 0, +1\}$, with the further condition that $J + J' \geq 1$, where J and J' are the initial and final values of J (since transitions $J = 0 \leftrightarrow J = 0$ would fail to conserve total angular momentum). If the validity of LS coupling can be assumed, this implies

$$\begin{aligned} \Delta l &\in \{-1, +1\} \\ \Delta S &= 0 \\ \Delta L &\in \{-1, 0, +1\} \end{aligned}$$

where furthermore $L + L' \geq 1$, again due to the momentum conservation constraint.

Finally, an issue of notation should be addressed. The values of L, S, and J are conventionally expressed *via* term symbols, which are notated as ${}^{2S+1}L_J$, where

coupling). The latter situation will not be discussed further here since it entails significant additional complication that is not relevant to the present work.

$2S + 1$ (i.e., the number of unique values of **S** possible with given S) is known as the *spin multiplicity*. Furthermore, L is denoted alphabetically following the sequence $L = 0 \rightarrow S,\ 1 \rightarrow P,\ 2 \rightarrow D,\ 3 \rightarrow F,\ 4 \rightarrow G$, continuing alphabetically (excluding J). Terms of odd parity are then distinguished by the suffix ° or subscript u, while even terms are either unqualified or subscripted g. For example, the ground states of the hydrogen atom and the Zn^{1+} ion each have one outer-shell electron with $l = 0$ and hence both obtain the term symbol ${}^2S_{½,g}$.

1.4 MOTIVATION FOR THE PRESENT STUDY

Although laser-induced plasma has been known for many years, a complete understanding of this phenomenon remains to be achieved, especially in the nanosecond-pulsed irradiation regime. This is due in large part to the strong mutual interactions between the underlying processes, many of which are intrinsically multi-scale effects that, as a result, are both difficult to reason about from first principles and present considerable challenges for numerical modelling studies. Furthermore, it is widely recognized that the stoichiometric, crystallographic, and morphological attributes of thin films and self-assembled nanostructures prepared by pulsed laser deposition (PLD) depend strongly on the process conditions employed, including the laser and backing gas parameters. However, the growth process remains relatively poorly understood, especially with respect to the reasons for the observed structural preference for discrete, epitaxially related crystals rather than homogeneous films under certain circumstances. Attempts have been made to rationalize this behaviour in terms of the identities and kinetic energies of species impinging on the deposition substrate,[23, 24] which clearly are intimately linked to the mechanisms of plasma plume formation and evolution. However, few direct studies exist of the latter in the presence of intermediate pressures ($\lesssim 0.1$ Torr) of reactive gases, as are generally employed in PLD applications. In the following chapters, an account will be given of the author's efforts toward experimentally characterizing the dynamics of laser-induced zinc and zinc oxide plasmas by means of their time- and space-resolved atomic emission spectra. In particular, the ablation plumes produced by low to moderate power density (≈ 1–10 GW/cm^2), nanosecond-pulsed irradiation of these materials at two wavelengths (355 and 532 nm) will be described, and their interaction with a static oxygen environment discussed.

1.5 SUMMARY OF ADDITIONAL RELATED WORK

A number of other materials were investigated that are not discussed here, most notably Al and Al_2O_3, for which a complete set of results was collected; Al_2O_3:ZnO was also afforded brief consideration as an intermediate case, as was Ga:ZnO, these two compositions being relevant to the PLD of doped ZnO. Mg and MgO were examined (*in vacuo* and under oxygen) for the case of 532 nm ablation only, and W/WO_3 and Mo/MoO_3 (both of which readily form nanoscale columnar crystals under PLD conditions) received a partial treatment, limited principally by the difficulty of assigning the many emission lines produced by the heavier atoms and (especially) their ions. These will be addressed in separate work.

Polarization-resolved measurements were also performed, prompted by the recent reports by R. J. Gordon and co-workers (see, for example, the publications by Liu *et al.*[25, 26]) of the near-total polarization of the continuum (bremsstrahlung) emission produced on laser ablation of silicon and aluminium. These are not included here since the present author was unable to reproduce these results for Al_2O_3, finding (in agreement with Asgill *et al.*[27]) no significant polarization of the bremsstrahlung emission. More precisely, although our initial observations seemed to be in excellent agreement with those of the previous authors, subsequent work revealed a small image shift caused by spurious refraction within the polarizing filter. Although this was sufficient to account for the apparent polarization effect, it would not have been readily apparent if (like Liu *et al.*) we had not employed an imaging spectrograph for the measurements. As a result, we believe that the initial report could have been mistaken, while the irradiance-dependence noted in the response of Liu *et al.* to the work of Asgill *et al.* can be understood as simply due to the changing size of the plasma as this parameter is varied.

Finally, we note that mass-spectrometric experiments were also attempted that were closely comparable to those performed by Leuchtner,[28] who employed a quadrupole mass filtered time-of-flight apparatus to obtain kinetic energy distributions for Zn^0 and Zn^{1+} produced during the laser ablation of ZnO. However, the application of this technique to the study of species with kinetic energies $\gg 1$ eV is subject to certain inherent difficulties that have seldom been discussed in the

literature. Most importantly, the charge state selectivity of the quadrupole mass filter strongly depends on the velocities of the ions, and extensive efforts by the present author led to the conclusion that the spurious transmission of high-energy species with non-resonant mass/charge values is a fundamental limitation of the technique. Although some reports (e.g. those by Hiroki *et al.*[29] and Du *et al.*[30]) exist of the successful analysis by this method of ions having translational kinetic energies of 10^2–10^3 eV, as are characteristic of laser ablation products, these rely on a highly atypical instrumental design that is challenging to construct. Leuchtner reported a bimodal Zn^{1+} KE distribution, assigning a secondary maximum at around 100 eV as the result of Zn^{2+}/e^- recombination. We believe that this interpretation of the data (albeit not the resulting assignment) was only fortuitously correct, since although similar observations were made in the present work (see later) our previous experience suggests that Leuchtner's time-of-flight data actually reflect the combined Zn^{1+} and Zn^{2+} KE distributions rather than that of Zn^{1+} alone. Owing to the unsatisfactory results obtained with this technique, the latter will not be discussed further in the present work.

1.6 REFERENCES

[1] "Oscillations in Ionized Gases", I. Langmuir, *Proc. Natl. Acad. Sci. USA* **14** (8), 627 (1928). DOI: 10.1073/pnas.14.8.627.

[2] J. G. Linhart, *Plasma physics*, 1st ed. (North-Holland Pub., Amsterdam, 1960)

[3] "Optical Intensity", R. Paschotta, in *Encyclopedia of Laser Physics and Technology*, *Vol. 2*, 1st ed. (Wiley-VCH, Berlin, 2008). ISBN: 978-3-527-40828-3.

[4] "Index of Refraction of ZnO", Y. S. Park and J. R. Schneider, *J. Appl. Phys.* **39** (7), 3049 (1968). DOI: 10.1063/1.1656731.

[5] "On the Feasibility of the Coulomb Explosion of a Metal", A. A. Rukhadze, U. Yusupaliev, and K. Shakhlevich (trans.), *Technical Physics* **49** (7), 933 (2004). DOI: 10.1134/1.1778872. Orig. "О возможности реализации кулоновского взрыва металла", А. А. Рухадзе и У. Юсупалиев, *Журнал Технической Физики* **74** (7), 127 (2004).

[6] "Ion emission from a metal surface through a multiphoton process and optical field ionization", M. Hashida, S. Namba, K. Okamuro, S. Tokita, and S. Sakabe, *Phys. Rev. B* **81** (11), 115422 (2010). DOI: 10.1103/PhysRevB.81.115442.

[7] "A general continuum approach to describe fast electronic transport in pulsed laser irradiated materials: The problem of Coulomb explosion", N. M. Bulgakova, R. Stoian, A. Rosenfeld, I. V. Hertel, W. Marine, and E. E. B. Campbell, *Appl. Phys. A* **81** (2), 345 (2005). DOI: 10.1007/s00339-005-3242-0.

[8] "Theory of electron-avalanche ionization induced in solids by electromagnetic waves", A. S. Epifanov, *IEEE J. Quantum Electron.* **17** (10), 2018 (1981). DOI: 10.1109/JQE.1981.1070646.

[9] "Avalanche ionization and dielectric breakdown in silicon with ultrafast laser pulses", P. P. Pronko, P. A. VanRompay, C. Horvath, F. Loesel, T. Juhasz, X. Liu, and G. Mourou, *Phys. Rev. B* **58** (5), 2387 (1998). DOI: 10.1103/PhysRevB.58.2387.

[10] "Laser–induced breakdown by impact ionization in SiO_2 with pulse widths from 7 ns to 150 fs", D. Du, X. Liu, G. Korn, J. Squier, and G. Mourou, *Appl. Phys. Lett.* **64** (23), 3071 (1994). DOI: 10.1063/1.111350.

[11] "The Relative Roles of Avalanche Multiplication and Multiphoton Absorption in Laser-Induced Damage of Dielectrics", A. Vaidyanathan, T. W. Walker, and A. H. Guenther, *IEEE J. Quantum Electron.* **16** (1), 89 (1980). DOI: JQE.1980.1070331.

[12] "Ionization in the field of a strong electromagnetic wave", L. V. Keldysh and J. G. Adashko (trans.), *Soviet Phys. JETP* **20** (5), 1307 (1965). Orig. "Ионизация в поле сильной электромагнитной волны", Л. В. Келдыш, *Журнал Экспериментальной и Теоретической Физики* **47** (5), 1945 (1964).

[13] "Theory of Two-Photon Spectroscopy in Solids", G. D. Mahan, *Phys. Rev.* **170** (3), 825 (1968). DOI: 10.1103/PhysRev.170.825.

[14] "Plasma generation and plasma sources", H. Conrads and M. Schmidt, *Plasma Sources Sci. Technol.* **9** (4), 441 (2000). DOI: 10.1088/0963-0252/9/4/301.

[15] H. Koskinen, *Plasma physics* (lecture course, Univ. Helsinki, 2012). URL: http://theory.physics.helsinki.fi/~plasma/.

[16] "Theoretical model of absorption of laser light by a plasma", P. Mora, *Phys. Fluids* **25** (6), 1051 (1982). DOI: 10.1063/1.863837.

[17] "Effect of laser parameters on laser ablation and laser-induced plasma formation: A numerical modelling investigation", A. Bogaerts and Z. Chen, *Spectrochim. Acta B* **60** (9–10), 1280 (2005). DOI: 10.1016/j.sab.2005.06.009.

[18] G. Herzberg and G. W. T. Spinks (trans.), *Atomic spectra and atomic structure*, 2nd ed. (Dover Pub., New York, 1944). Orig. *Atomspektren und Atomstruktur* (Steinkopff, Dresden, 1936). ISBN: 978-0-486-60115-1.

[19] A. Sommerfeld and H. L. Brose (trans.), *Atomic Structure and Spectral Lines*, 3rd ed. (Methuen, London, 1934). Orig. *Atombau und Spektrallinien*, 5th ed. (Vieweg, Braunschweig, 1931).

[20] I. I. Sobelman, *Atomic Spectra and Radiative Transitions*, 1st ed. (Springer-Verlag, Berlin, 1979). ISBN: 978-3-540-09082-3.

[21] A. Corney, *Atomic and Laser Spectroscopy*, 1st ed. (Clarendon Press, Oxford, 1979). ISBN: 978-0-19-851148-9.

[22] T. P. Softley, *Atomic Spectra*, 1st ed. (OUP, Oxford, 1994). ISBN: 978-0-19-855688-6.

[23] "Effect of incident fluence on the growth of ZnO nanorods by pulsed excimer laser deposition", Ye Sun, R. P. Doherty, J. L. Warren, and M. N. R. Ashfold, *Chem. Phys. Lett.* **447** (4–6), 257 (2007). DOI: 10.1016/j.cplett.2007.09.018.

[24] "Ultrathin aligned ZnO nanorod arrays grown by a novel diffusive pulsed laser deposition method", G. M. Fuge, T. M. S. Holmes, and M. N. R. Ashfold, *Chem. Phys. Lett.* **479** (1–3), 125 (2009). DOI: 10.1016/j.cplett.2009.08.008.

[25] "Observation of near total polarization in the ultrafast laser ablation of Si", Yaoming Liu, S. Singha, T. E. Witt, Yongtao Cheng, and R. J. Gordon, *Appl. Phys. Lett.* **93** (16), 161502 (2008). DOI: 10.1063/1.3000966.

[26] "Polarization and fluence dependence of the polarized emission in nanosecond laser-induced breakdown spectroscopy", J. S. Penczak, Yaoming Liu, and R. J. Gordon, *Spectrochim. Acta B* **66** (2), 186 (2011). DOI: 10.1016/j.sab.2010.12.009.

[27] "Investigation of polarization effects for nanosecond laser-induced breakdown spectroscopy", M. E. Asgill, H. Y. Moon, N. Omenetto, and D. W. Hahn, *Spectrochim. Acta B* **65** (12), 1033 (2010). DOI: 10.1016/j.sab.2010.11.010.

[28] "Mass spectrometry and photoionization studies of the ablation of ZnO: ions, neutrals, and Rydbergs", R. E. Leuchtner, *Appl. Surf. Sci.* **127–129**, 626 (1998). DOI: 10.1016/S0169-4332(97)00716-2.

[29] "Applicability of the rf-only mode in a quadrupole mass spectrometer for direct analysis of keV ions", S Hiroki, K Kaneko, and Y Murakami, *Vacuum* **46** (12), 1445 (1995). DOI: 10.1016/0042-207X(95)00168-9.

[30] "Elemental analysis with quadrupole mass filters operated in higher stability regions", Zhaohui Du, D. J. Douglas, and N. Konenkov, *J. Anal. At. Spectrom.* **14**, 1111 (1999). DOI: 10.1039/A804022B.

EXPERIMENTAL METHODS

2.1 EXCITATION

2.1.1 LASER

The laser used in this work was a flashlamp-pumped, *Q*-switched Nd:YAG device (Quanta-Ray DCR-11, Newport Spectra-Physics, Santa Clara, California), operating at a wavelength of either 532 or 355 nm, and with a pulse repetition frequency (PRF) of 2.5 Hz.[a] 532 nm (i.e., green) light was employed in the first instance due to the relative safety and ease of alignment of the visible beam, while 355 nm (UV-A) radiation was used as a closer approximation to the 248 nm (KrF*) or 193 nm (ArF*) emission produced by the exciplex lasers normally employed in pulsed laser deposition applications. Despite the smaller photon energy and relatively low efficiency of the Nd:YAG laser as compared to an exciplex device, the former was preferred in the present work for reasons of its improved repeatability due to lower timing jitter, stable and precisely controllable output power, and superior temporal and spatial beam quality.

Resonator design and beam profile

The DCR-11 is somewhat unusual in that it employs an unstable resonator design (concave total reflector, convex output coupler; see Figure 2.1) wherein the emitted beam is formed by diffraction past the output coupler, the latter being totally reflecting, but covering only the central portion of the output aperture. Such a design has advantages for pumping efficiency, beam quality at high output power, and temporal pulse shape,[1] but unlike the majority of similar lasers in current use, produces a ring- (or "doughnut"-) shaped spot in the near field. It should be noted that, in the present work, the distance over which the beam was allowed to propagate (≈ 2 m) was not sufficient for the central portion of the ring to be filled in completely, and therefore the geometry of the laser spot on reaching the target (cf. §2.2.2, page 37) was intermediate between the near-field ring shape and the far-field Gaussian profile expected of a diffraction-limited TEM_{00} beam. Figure 2.2 depicts the resonator

[a] This non-standard PRF was the result of a flashlamp frequency of 10 Hz, required for thermal stability of the resonator, but with the *Q*-switch being fired only on every fourth flashlamp shot for reasons explained later in §2.3.2 (page 40).

with a more realistic (albeit still understated) aspect ratio and demonstrates the high volume utilization of the gain medium possible with this design.

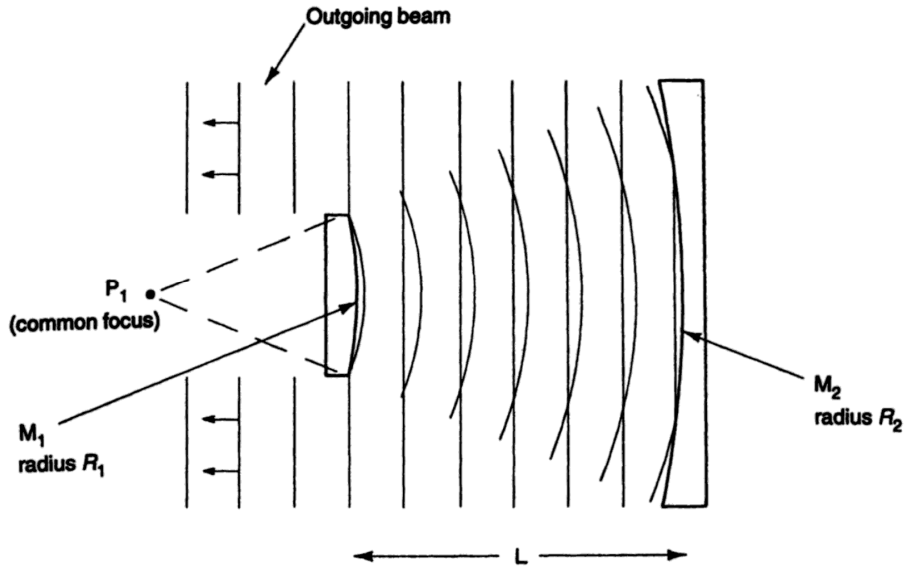

Figure 2.1: Detail of laser resonator design showing diffraction-coupled output. Image reproduced from *Solid-State Laser Engineering* by W. Koechner.[2]

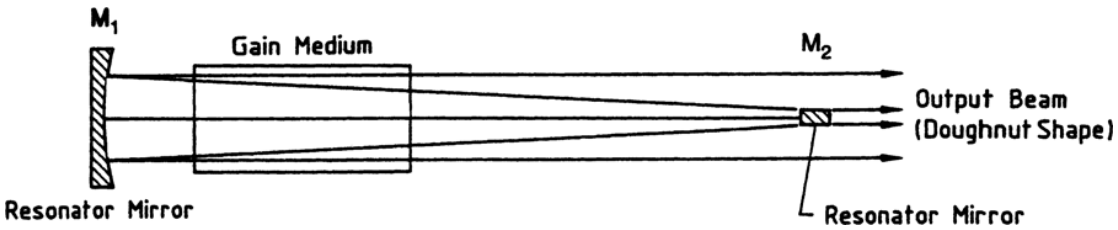

Figure 2.2: Laser resonator drawn with more realistic aspect ratio indicating position of gain medium. Also from *Solid-State Laser Engineering*.[3]

Harmonic generation

Since the wavelength of the fundamental emission from a standard Nd:YAG laser is 1064 nm, radiation of other wavelengths must be obtained by means of nonlinear optical processes such as harmonic generation or sum/difference frequency mixing. In the present case, 532 nm (second harmonic) radiation was obtained in the conventional way by direct frequency doubling of the fundamental wavelength using an extracavity phase-matched KD*P (potassium dideuterium phosphate) crystal, while 355 nm (third harmonic) radiation was produced indirectly by sum frequency mixing of the 1064 and 532 nm beams in a second and subsequent crystal of the same type. Both crystals were mounted in a sealed, temperature-stabilized assembly

(Quanta-Ray HG-2, Spectra-Physics) equipped with independent angular adjustments for each crystal and a half-wave plate (at 1064 nm, allowing for rotation of the polarization of the fundamental beam) serving as the input window. The angles of the crystals and half-wave plate were adjusted for optimum phase matching in order to obtain maximum laser pulse energy at the wavelength of interest, and the resulting (horizontal) polarization of the output followed that of the input beam, being *p*-oriented with respect to the target surface normal. Laser radiation at the fundamental and fourth harmonic (266 nm) wavelengths was not used for ablation experiments in the present work, which was due to limited applicability to pulsed laser deposition scenarios in the former case, and insufficient pulse energy in the latter.

The initially co-propagating fundamental, second, and third harmonic beams were spatially separated using a purpose-built assembly (Quanta-Ray PHS-1, Spectra-Physics) containing a Pellin-Broca prism, half-wave plates for the 532 and 355 nm wavelengths, and a beam dump into which the unwanted beams were directed. Most surfaces exhibit lower reflectance (i.e., higher absorption) of *p*-polarized radiation relative to *s*-polarized,[4] but using the half-wave plates in the PHS-1 to rotate the polarization of the excitation beam through 90° revealed no apparent dependence of ablation characteristics or plasma properties on the polarization of the incident radiation. As a result, horizontally polarized radiation was employed for all experiments discussed in the present work.

Pulse energy adjustment

On flashlamp pumping of the Nd:YAG gain medium, Nd^{3+} ions transition from their ground ($^4I_{9/2}$) electronic state into a variety of excited states, the most significant of which are the $^4F_{5/2}$ and $^2H_{9/2}$ terms, populated by absorption at around 808 nm.[5] The lower-lying metastable $^4F_{3/2}$ level is then populated by relaxation *via* internal conversion and inter-system crossing. Depending on the duration of the flashlamp pulse for a given laser and the rates of these radiationless transitions (which depend in turn on Nd^{3+} dopant concentration and the temperature of the YAG rod), a period of typically ≈ 160–240 μs elapses between the initiation of pumping and maximum population of the $^4F_{3/2}$ level. For the DCR-11 laser used in the present work, the time between pumping and maximum population inversion (i.e., the delay required

between firing the flashlamp and triggering the *Q*-switch in order to achieve maximum pulse energy) was found to be around 230 μs.

As the fluorescence lifetime of the $^4F_{3/2}$ state of Nd^{3+} is also ≈ 230 μs, it is straightforward in practice to trigger the *Q*-switch later than the optimum time in order to obtain a laser pulse of reduced energy, the initial population inversion having been diminished in the interim by spontaneous emission. The latter is not amplified, and therefore does not contribute to the formation of an optical pulse, while the resonator is in the low-*Q* state. For the DCR-11, *Q*-switch delays of between 230 and 420 μs after flashlamp firing were found to yield output pulses with stable, predictable build-up time and almost-Gaussian temporal profile that could be rapidly and repeatably varied in energy over approximately an order of magnitude using a digital pulse/delay generator (BNC model 555, Berkeley Nucleonics Corp., San Rafael, California). In contrast, varying the flashlamp power alters the heat loading of the resonator and gain medium (the thermal equilibration of which was critical to pulse energy and timing stability, and took approximately 1 hour to achieve), leading to poor repeatability and a somewhat uncertain outcome of any attempted change. It is important to note, however, that the laser pulse energy and duration are mutually (inversely) related in general (cf. Figure 2.3/Equation 2.8 and associated discussion on pp. 33–33), and consequently that the above-described procedure for power adjustment involved the simultaneous variation of both quantities during experiments. According to Bogaerts and Chen,[6] the characteristics of the laser-induced plasma obtained for given incident fluence are only weakly dependent on pulse duration, so that, provided the latter is properly considered in deriving irradiance values, we do not expect the measurements to reflect a significant confounding effect between these two factors. Indeed, parallel analyses conducted with respect to irradiance and fluence can be shown to return qualitatively similar results, albeit with quantitative differences arising for obvious reasons. The currently available literature suggests that no clear consensus has arisen in favour of either metric in experimental reports, whereas modelling studies typically quote irradiance values. The latter will be employed in the present work, principally in order to facilitate comparison with theoretical accounts, since in the author's opinion these are generally more conclusive as to the detailed physical processes underlying particular observations than the corresponding experiments.

2.1.2 LASER PULSE ENERGY AND DURATION MEASUREMENTS

Owing to the importance of correctly determining the actual laser power employed in a given experiment, a careful approach was taken toward power calibration based on combined pulse energy and duration measurements. The principal apparatus employed for this was a high-speed, large area silicon PIN photodiode (FND-100Q, Perkin-Elmer Optoelectronics, Montgomeryville, Pennsylvania) having a specified bandwidth of 350 MHz and rise/fall time of < 1 ns (10–90% or 90–10%, when operating in the photoconductive mode with reverse bias of 90 V) into a 50 Ω load. The FND-100Q was biased by means of a large[b] capacitor that was charged using a 50 V bench-top DC power supply (the response time being estimated conservatively at ≈ 1.0 ns for this bias voltage), and connected to a 500 MHz, 2 GS/s oscilloscope (WaveSurfer 454, LeCroy, Chestnut Ridge, New York) for recording and analysis of the optical signal. Using this setup, several laser pulse parameters could be measured simultaneously, namely absolute delay between the *Q*-switch trigger signal and the optical pulse (i.e., build-up time), total energy, temporal shape, and FWHM (full width at half maximum) duration. Furthermore, each of these properties could be measured either for a single laser pulse, or (more usually) averaged over all pulses produced during a given sub-experiment, with the latter approach also providing values for the errors associated with the pulse energy and duration measurements.

Although the photodiode voltage signal is (for sufficiently small photocurrent) inherently proportional to the incident optical power, in practice the constant of proportionality is not known without reference to an external standard. The average photodiode response integrated over the duration of a single laser pulse was therefore compared to the average power measured using a commercial power meter (FieldMax II-TO, equipped with a calibrated PM-10 thermopile sensor, Coherent Inc., Santa Clara, California) divided by the measured pulse repetition frequency. Clearly, it is impossible to employ a power meter of this sort when the same laser radiation that would have been absorbed in order to measure its power is instead required to impinge upon and ablate a target. As a result, the power meter was used only for

[b] That is, of sufficiently high capacitance for the rate of discharge through the photodiode to be negligible, so that the bias voltage would remain almost constant during experiments even if the capacitor was not recharged.

measurements made specifically for the purpose of transferring its calibration to the photodiode readings, and laser power during ablation experiments was instead determined solely using the photodiode, with which measurements were made of a small constant fraction of the total radiation scattered from a beam steering mirror.

Power calibration procedure

Calibrated power measurements were obtained from the as-measured photodiode signal by way of several consecutive calibrations and corrections as follows. Firstly, the relationship between the time-integrated photodiode response and pulse energy was established, and the resulting calibration applied to photodiode readings made during the experiments proper. Next, the measured FWHM pulse durations were corrected for the photodiode response time and deviations of the temporal pulse shape from Gaussianity. Finally, the values obtained for the pulse energy and true FWHM duration were combined to yield the average pulse power. The remainder of this subsection will describe each of these sub-procedures in detail.

Photodiode calibration measurements were made for several (typically 11 or 18) *Q*-switch delays. Power meter readings were taken for each of these as six consecutive five-second averages, firstly with the *Q*-switch active, and then again with it disabled (in order to determine any offset due to thermal drift). The mean and standard deviation of the mean were then determined for each set of six readings, with the latter (strictly, after correction for sample size effects, the *best unbiased estimator of the population standard deviation*) given by:

$$\hat{\sigma} = \frac{\Gamma\left(\frac{n-1}{2}\right)}{\sqrt{\frac{2}{n}}\Gamma\left(\frac{n}{2}\right)} \frac{s}{\sqrt{n}} \qquad \text{Equation 2.1}$$

where n is the sample size (here six), s is the *sample* standard deviation (having the ordinary definition, including Bessel's correction, and not to be confused with $\hat{\sigma}$), and $\Gamma(\cdot)$ is the gamma function.[7] The pulse energy for each *Q*-switch delay was then calculated as:

$$E = \frac{P_1 - P_0}{f} \pm \frac{1}{f^2}\sqrt{f^2\left(\hat{\sigma}(P_0)^2 + \hat{\sigma}(P_1)^2\right) + \left(P_0 - P_1\right)^2 s(f)^2} \quad \text{Equation 2.2}$$

where P_1 and P_0 are the means of the power measurements taken with the *Q*-switch enabled and disabled, respectively, $\hat{\sigma}(P_1)$ and $\hat{\sigma}(P_0)$ are the standard deviations of these values per Equation 2.1, f is the measured mean pulse repetition frequency, and $s(f)$ is the sample standard deviation of f.[c]

The expression for the standard error given as part of Equation 2.2, representing one standard deviation, is easily obtained through a conventional treatment of error propagation.[d] However, it is worth noting that it arose in fact, as do all such errors quoted in the present work, from a somewhat generalized formulation of the standard approach, which is rather easier to state concisely and at the same time explicitly accounts for correlation between both the measured values and the results calculated from them. In this, covariance matrices consisting of experimentally determined standard errors and their correlations are transformed using the n^{th}-order Taylor expansion of a vector-valued function of the measured values. That is:

$$\hat{\mathbf{\Sigma}} = \sum_{\alpha=1}^{n} \frac{1}{\alpha!} (\widetilde{D}_2^{\alpha}\mathbf{f})\, \mathbf{\Sigma}^{\alpha}\, (\widetilde{D}_2^{\alpha}\mathbf{f})^{\mathrm{T}} \quad \text{Equation 2.3}$$

where $\mathbf{\Sigma}$ is the covariance matrix associated with the vector of variables $\mathbf{x}$, $\mathbf{f}$ is a mapping from $\mathbf{x}$ to a vector $\mathbf{y}$ of results calculated from $\mathbf{x}$ (where $\mathbf{x}$ and $\mathbf{y}$ need not have the same dimension), and $\widetilde{D}_2^{\alpha}$ is a matrix-valued derivative operator defined so that $\widetilde{D}_2^{1} = J$, where J is the Jacobian matrix, and for higher derivatives,

$$\widetilde{D}_2^{\alpha}\mathbf{f} = (D_{\mathbf{x}}^{\alpha} \otimes \mathbf{f})_{i\ j\ \ldots}^{\ j\ j} \quad \text{Equation 2.4}$$

[c] The reason for the direct use of $s(f)$ rather than the corrected value according to Equation 2.1 is that the sample on which it was based was large enough that population size effects were insignificant.

[d] See, e.g., the Joint Committee for Guides in Metrology (JCGM) standard 100:2008(E), entitled *Guide to the expression of uncertainty in measurement*, which is available from the International Standards Organization (ISO) website at http://www.iso.org/sites/JCGM/GUM-JCGM100.htm.

where $D_{\mathbf{x}}^{\alpha}$ is the derivative operator of total order α in $\mathbf{x}$ (e.g., $D_{\mathbf{x}}^{2} = H$, where H is the Hessian matrix), $\otimes$ represents a tensor product, and i and j are summation indices according to the Einstein convention. It should be noted that analytic errors on calculated values derived in this way are exact if the sum converges absolutely (i.e., for $\mathbf{f}$ everywhere smooth and n sufficiently large), provided also that the errors on the measured values are random and normally distributed, and the magnitudes of the elements of $\boldsymbol{\Sigma}$ are small. If any of these conditions is violated, error propagation by Monte Carlo methods is likely to be more robust. However, a comparison between standard errors obtained using each of these methods for a variety of strongly nonlinear and/or divergent functions suggests that, in practice, an expansion truncated at $n = 2$ (resulting in a local quadratic approximation) is usually adequate, and analytically propagated errors deviate significantly from Monte Carlo results only with substantial errors ($\approx 10\%$) in the variables. Analytic errors were therefore employed exclusively where the validity of the underlying assumptions was not in question since they can be calculated directly from the experimentally measured values and are otherwise more easily manipulated than numerical covariance matrices.

The linear relationship between the laser pulse energies E_i measured for each calibration experiment i using the power meter and the simultaneously recorded photodiode readings A_i (integrated over each pulse and then averaged over all pulses produced while power meter readings were taken) was verified and its coefficients determined using a weighted least squares fit, with the weights specified as,

$$w_i = \frac{1}{\sigma(E_i)^2 s(A_i)^2} \qquad \text{Equation 2.5}$$

where $\sigma(E_i)$ is the standard error from Equation 2.2 and $s(A_i)$ is the sample standard deviation of the corresponding photodiode measurements. While the linearity of the photodiode was maintained over the full range of pulse energies employed and irrespective of wavelength, the power meter was found to respond sub-linearly at 355 nm for energies of > 40–50 mJ/pulse due to slight ablation of the strongly

absorbing surface of the thermopile sensor.[e] In order to account for this systematic error, the weights applied at higher pulse energies were reduced proportionally to the degree of under-reading, the latter being assessed by extrapolation (based on the photodiode readings) from the low-energy linear regime.

Parameters estimated by least squares fitting are, in general, correlated, so proper consideration must be given to the off-diagonal elements of the covariance matrix in order to obtain correct errors for values calculated using a fitted model. In this case, Equation 2.3 yields (for $n = 2$) the exact result, with the photodiode calibration and its associated error being:

$$\hat{E}_j = aA_j + b \pm \sqrt{\begin{array}{c} \tfrac{1}{2}\sigma(a)^4 + \tfrac{1}{2}s(A_j)^4 + a^2 s(A_j)^2 + {A_j}^2\sigma(a)^2 + \\ \tfrac{1}{2}\operatorname{cov}(a,b)^2 + \sigma(b)^2 + 2A_j \operatorname{cov}(a,b) \end{array}} \qquad \text{Equation 2.6}$$

where A_j and $s(A_j)$ are a photodiode measurement made during an ablation experiment j and its associated sample standard deviation, a and b are the coefficients determined from the least squares fit to the calibration data, $\sigma(a)$ and $\sigma(b)$ are the standard errors on these values, and $\operatorname{cov}(a,b)$ is their mutual covariance. The values $\hat{E}_j$ are then the calibrated pulse energies.

The values now required are the FWHM pulse durations τ_j, which were obtained almost directly from the transient photodiode signal. Two corrections were, however, applied to the measured values, with the first of these accounting for the finite photodiode response time. The true FWHM pulse duration of a Gaussian laser pulse, given an experimental FWHM τ_1 measured using a detector with response time τ_2 (specified as stated on page 27) can be shown to be:[f]

[e] Although this observation was rather disconcerting, the maximum energy density of the measured beam remained an order of magnitude below the manufacturer's stated damage threshold for the sensor, so it was assumed that the latter would not suffer any permanent loss of accuracy as a result.

[f] This relationship was determined by the author using *Mathematica* (Wolfram Research, Champaign, Illinois). The expression for the standard error of the true FWHM in terms of τ_1 and τ_2 and their errors was calculated using Equation 2.3, but is too large to present here.

$$\mathrm{FWHM} = \sqrt{{\tau_1}^2 - \frac{2{\tau_2}^2 \ln 4}{\left(\sqrt{\ln 1/0.9} - \sqrt{\ln 1/0.1}\right)^2}} \qquad \text{Equation 2.7}$$

Measured FWHM pulse durations varied between approximately 6.8 and 14.3 ns and τ_2 was considered equal to 1.00±0.05 ns, so by Equation 2.7 the absolute (relative) overestimation introduced by this method of measurement ranged from 0.07 ns (0.5%) for the longest pulses to 0.14 ns (2.2%) for the shortest. While this error is not particularly large, it is both systematic and pulse energy-dependent, since the pulse energy and duration vary together, with the shortest pulses obtained at the highest energies. Correction of the measured FWHMs was therefore considered important in order to avoid introducing a significant bias into estimates of laser power obtained from the measured pulse energies and durations together.

The second correction was necessary because the experimental FWHMs did not vary monotonically with pulse energy (*Q*-switch delay); instead, seemingly random (but repeatable) deviations from the expected trend were observed for energies greater than about 30 mJ (cf. Figure 2.3), again only for $\lambda = 355$ nm. Crucially, these fluctuations had no apparent effect on the recorded optical emission intensities, which varied smoothly. Since different distributions can exhibit equal variance without necessarily possessing the same FWHM, this effect was understood to be a result of the temporal pulse shape deviating slightly from the Gaussian profile implicitly assumed to be applicable at all energies. True variance is therefore more correctly stated in terms of an effective, rather than actual, FWHM, which was calculated as follows.

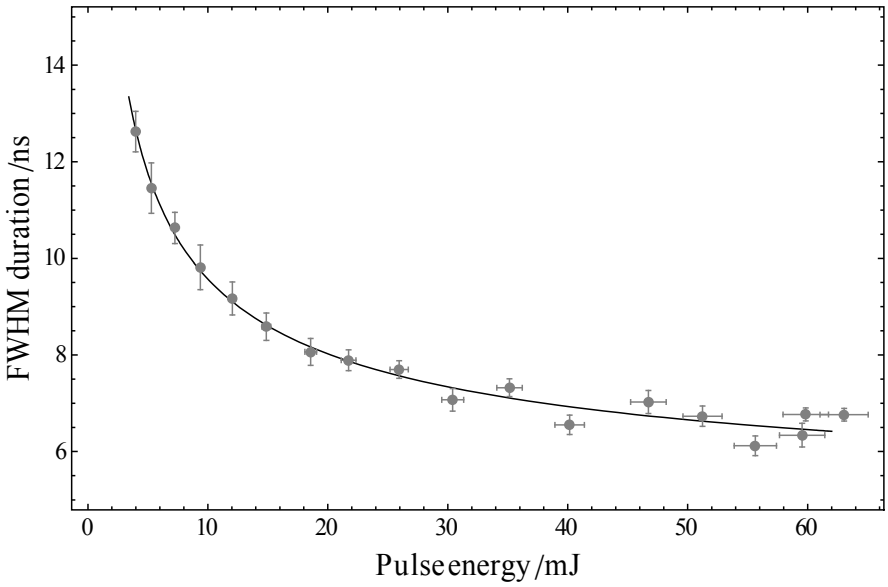

Figure 2.3: Relationship between laser pulse energy and FWHM duration for the DCR-11 operating at 355 nm. The points represent measurements at different *Q*-switch delays, while the solid line is the theoretical curve from Equation 2.8.

The theoretical relationship between the energy and duration of pulses produced by a *Q*-switched four-level laser, given by Koechner and Bass as a pair of parametric equations,[8] can be solved in terms of Lambert's *W*-function to yield the expected FWHM duration of Gaussian pulses of a given energy:

$$\mathrm{FWHM} = \frac{\tau_r}{\delta_r}\frac{-\log^2(-Z)}{Z\log(-Z)+(Z+1)\left(\log\left\{\dfrac{Z+1}{Z\log(-Z)}\right\}-1\right)}$$

$$\text{with } Z = W_{-1}\left(-\exp\left\{-\frac{\alpha+\varepsilon}{\alpha}\right\}\right) \qquad \text{Equation 2.8}$$

$$\text{and } \alpha = \hbar\omega\frac{\pi r^2}{2\sigma}\delta_r$$

Here, τ_r is the cavity round-trip time (4.6 ns for the DCR-11, which has a cavity 69 cm long), $\hbar\omega$ is the photon energy (1.86×10^{-19} J at 1064 nm), σ is the stimulated emission cross-section (2.8×10^{-19} cm^2 for a YAG rod with an Nd^{3+} dopant concentration typical for *Q*-switched operation), and ε is the pulse energy. $W_{-1}(\cdot)$ represents the $(-1)^{\text{th}}$ branch of the *W*-function, which has no closed form representation. The values of δ_r (round-trip loss) and r (effective beam radius) are both unknown and must be obtained by fitting Equation 2.8 to the data; an offset c

representing a minimum FWHM was also introduced in order to improve the result of this fitting for second or third harmonic optical pulses, to which the theoretical relationship does not strictly apply. Notwithstanding this caveat, Figure 2.3 demonstrates excellent agreement of the model with the data, especially below 30 mJ/pulse, where minimal deviation from Gaussianity was observed. "Gaussian-equivalent" FWHMs $\hat{F}_j$ were thus obtained by moving each point onto the theoretical curve while retaining the original errors (which represent the probable random, rather than systematic, deviation from the expected value).

Finally, average power (in MW) was calculated as the ratio of the calibrated pulse energy $\hat{E}_j$ to the corresponding effective pulse duration $\hat{F}_j$. Since this operation is strongly nonlinear and the error terms $\sigma(\hat{E}_j)$, $\sigma(\hat{F}_j)$, and $\mathrm{cov}(\hat{E}_j, \hat{F}_j)$ were all significant, Equation 2.3 was used with $n = 2$ to obtain the error on the result, giving

$$P_j = \hat{E}_j \big/ \hat{F}_j \pm \frac{1}{\sqrt{2}\hat{F}_j^{\,3}} \sqrt{\begin{array}{c} 2\hat{E}_j^{\,2}\hat{F}_j^{\,2}\sigma(\hat{F}_j)^2 + 2\hat{F}_j^{\,4}\sigma(\hat{E}_j)^2 + \\ \hat{F}_j^{\,2}\sigma(\hat{E}_j)^4 + (\hat{F}_j - 2\hat{E}_j)^2\sigma(\hat{F}_j)^4 + \\ 2\,\mathrm{cov}(\hat{E}_j, \hat{F}_j)^2(2\hat{E}_j^{\,2} - 2\hat{E}_j\hat{F}_j + \hat{F}_j^{\,2}) - \\ 2\hat{F}_j\,\mathrm{cov}(\hat{E}_j, \hat{F}_j)\times \\ \left(2\hat{E}_j\hat{F}_j^{\,2} + (2\hat{E}_j - \hat{F}_j)\left(\sigma(\hat{E}_j)^2 + \sigma(\hat{F}_j)^2\right)\right) \end{array}} \qquad \text{Equation 2.9}$$

which stands as an apt demonstration of the rapid growth in complexity with increasing n of explicit expressions for the error, even for such simple transformations as the division of two quantities. This does not, of course, imply that the error is itself large; indeed, with $\mathrm{cov}(\hat{E}_j, \hat{F}_j)$ negative, as in the present case, the second-order expansion will yield a tighter error bound than the linear terms alone.

2.1.3 POINTING AND FOCUSING OPTICS

An optical apparatus consisting of two dielectric mirrors (MaxMirror, Semrock, Rochester, New York)[g] and two uncoated fused silica lenses was used to direct and focus laser radiation onto the surface of the target. Both mirrors were placed in two-axis adjustable mounts with a mutual 45° angle of incidence, resulting in a Z-shaped arrangement that allowed the beam to be "walked" onto the desired propagation axis. The lenses had equal and opposite focal lengths (250 and −250 mm, respectively) and were employed together as a beam condenser in an afocal converging-diverging (Galilean) telescopic configuration. Additionally, the second (diverging) lens was mounted on a micrometer-driven translation stage so that the position of the focus, nominally at the target surface, could be adjusted accurately over a wide range to accommodate targets of different thickness while maintaining a fixed spot size.

Power measurements using the thermopile sensor, as described above, were made between the mirrors and the beam condenser, since the power density after the latter (and especially inside the chamber; see below) was, by design, sufficient to ablate any absorptive material even at the minimum usable laser pulse energy. It was therefore necessary for the purposes of calculating the absolute irradiance (in GW/cm^2) impinging on the target to assume $\approx 4\%$ reflection losses at each uncoated optical surface, yielding a transmittance through the two lenses and the entrance window to the chamber of ≈ 0.8. Though relatively poorly characterized, this value remained constant for all experiments, the results from which were typically well modelled by power law relationships between irradiance and optical emission intensity (see later). Any inaccuracy in the assumed transmittance (which it is reasonable to suppose will not exceed a few percent) therefore represents a systematic scaling error on all of the irradiance figures quoted in this work, but will not be manifested in the values obtained for the power law exponents since it mathematically cancels from the definition of this quantity.

[g] These mirrors were suitable for the Nd:YAG fundamental and the second and third harmonics, but had a relatively low damage threshold at 355 nm. Consequently, for high pulse energies at this wavelength, laser line mirrors were used instead (Y3, CVI Melles Griot, Albuquerque, New Mexico).

2.2 ABLATION CHAMBER

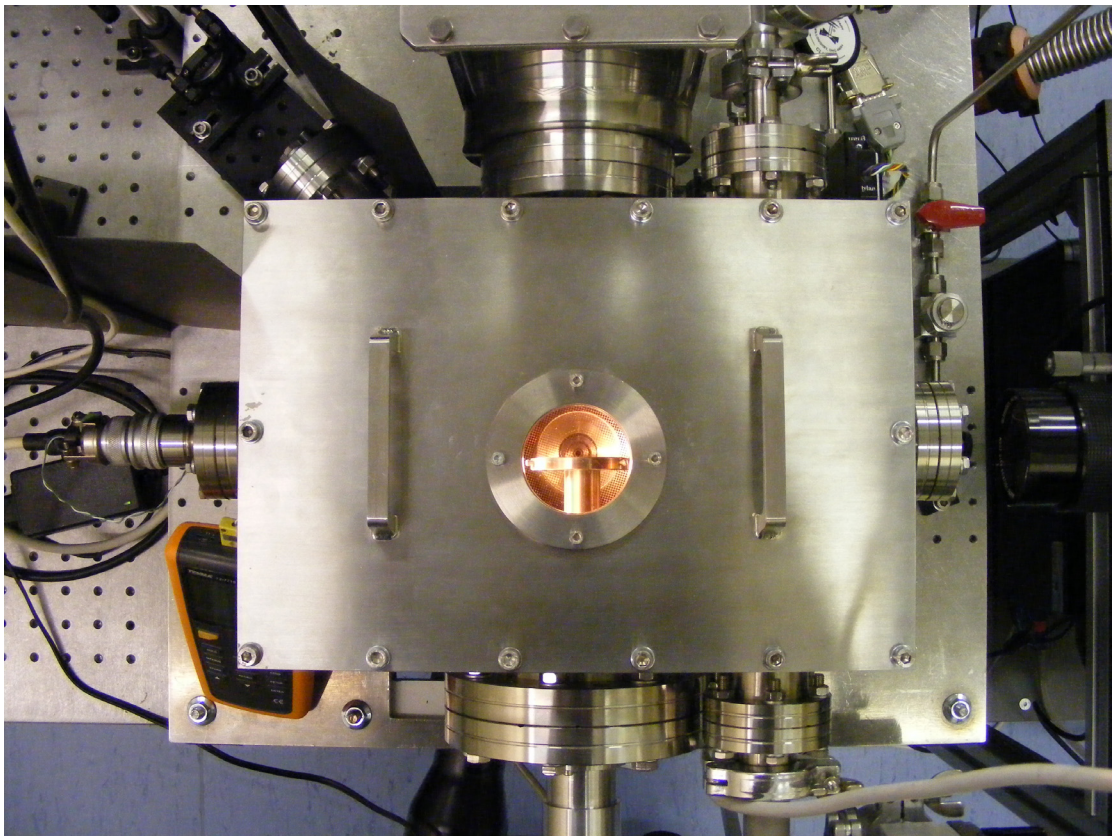

Figure 2.4: Photograph of the ablation chamber from above showing laser entrance window (top left), target in holder (centre), and observation window (right).

2.2.1 VACUUM SYSTEM AND PROCESS GAS SUPPLY

Vacuum was produced and maintained during experiments using a 6-inch turbomolecular pump (TMP-151, Oerlikon Leybold, Cologne, Germany) mounted on the base of the ablation chamber. This was backed by a two-stage rotary vane pump (E2M8, Edwards, Crawley, West Sussex), which was also used to establish rough vacuum (with the turbomolecular pump isolated) after the chamber had been vented. Ultimate vacuum was $\approx 10^{-7}$ mbar, with pressure measurement in this range accomplished using a Penning ionization gauge (AIM-S, Edwards).

Oxygen was admitted to the chamber by means of a mass flow controller (MFC) (Tylan FC-260, Qualiflow, Montpellier, France) and a constant pressure of between approximately 10^{-3} and 10^{-1} Torr, measured with a capacitance manometer (CTR 100, Oerlikon Leybold), established by adjusting the inlet flow rate (≈ 10–15 standard cubic centimetres/minute) with the gate valve partially closed.

2.2.2 TARGET

Various metal and metal oxide sputtering targets of 99.9% or higher purity were purchased from Testbourne Ltd. (Basingstoke, Hampshire). The two-inch diameter circular targets were fixed in a rotating mount, which turned at ≈ 1 rev/min so that each successive laser pulse would fall on a different area than the last to minimize any cumulative effects. Despite this, a tightly focused laser spot was not usable without incurring severe surface damage to all but the most mechanically resilient materials (e.g. Al_2O_3; W), which caused the ablation plume (which propagates nominally along the target surface normal) to slew progressively toward the entrance window during experiments. As a result, in order to improve experimental reproducibility by preserving the condition of the target and window as far as possible, a defocused (i.e., ring-shaped; cf. §2.1.1) spot was instead employed that had 275±10 μm outer and ≈ 120 μm inner diameters, giving a total area of $\approx 4.8 \times 10^{-4}$ cm^2.

Shims were used so that the surface of each target lay in approximately the same plane (±250 μm) irrespective of thickness, but adjustments to the position of the focus were typically also necessary in order to achieve the desired spot size, which was verified by microscopic examination of the target after each experiment. The photomicrographs given in Figure 2.5 show the effect of the loosely focused laser radiation on several targets, each having a different thickness, ablated both *in vacuo* and under oxygen. While the detail of the observed track morphology is clearly dependent on the thermal and mechanical properties of the material and the presence or otherwise of an oxidizing environment during ablation, the consistent spacing of the two parallel furrows and width of the central ridge are indicative of a highly reproducible spot size and shape. Nevertheless, the uncertainty in absolute irradiance due to imprecise determination of the spot size certainly represents by far the largest source of error in the present work. While a similar argument applies here as was put forward previously in §2.1.3, in this case it cannot be assumed that the effect is identical for every experiment, and this must be borne in mind especially when comparing results obtained using different targets.

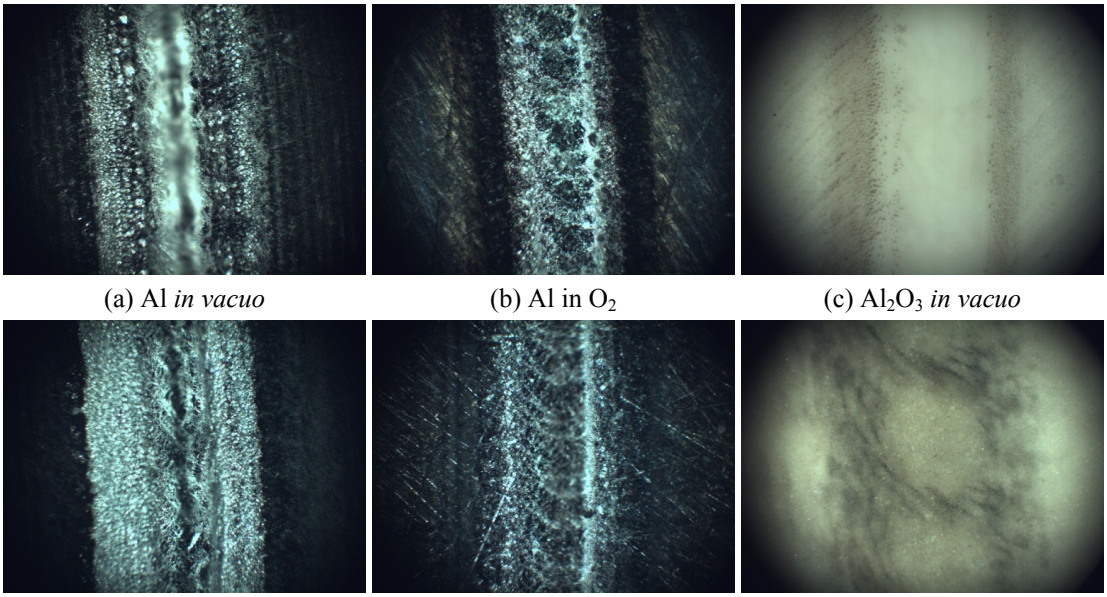

(a) Al *in vacuo* (b) Al in O_2 (c) Al_2O_3 *in vacuo*

(d) Zn *in vacuo* (e) Mg in O_2 (f) $ZnO:Al_2O_3$ in O_2

Figure 2.5: Polarized light photomicrographs (all at equal magnification) of tracks formed on targets of various materials during ablation experiments. The size of the features observed was determined by comparison with a sample (a TEM grid) of known dimensions (not shown).

2.3 DETECTION

2.3.1 IMAGING OPTICS AND SPECTROGRAPH

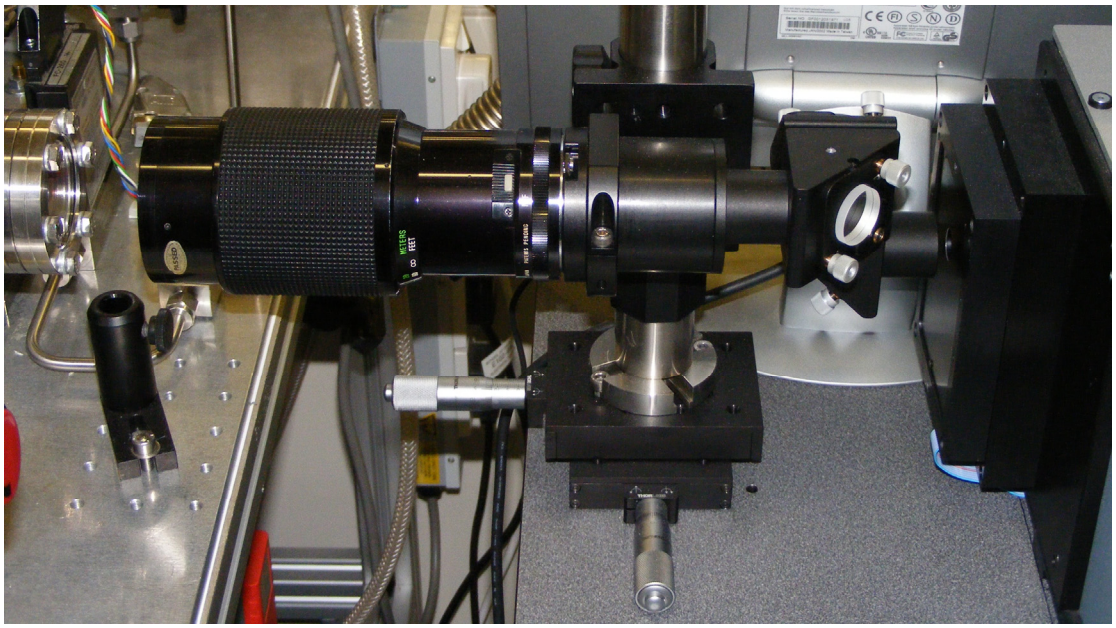

Figure 2.6: Photograph of the lens and mirror arrangement used to image the laser plasma/ablation plume onto the slit of the spectrometer (right).

Radiation (i.e. bremsstrahlung, atomic lines, and molecular emissions) emitted by the laser plasma over the spectral range ≈ 390–850 nm was characterized by imaging spectroscopy. The horizontally propagating ablation plume was observed, as shown in Figure 2.6, using a photographic lens (Series 1 70–210 mm *f*/3.5 macro-focusing zoom lens, Vivitar), the output from which was collimated by means of a diverging optic located at the focal plane. This beam proceeded *via* a series of three mirrors, effecting a rotation through 90°, with a subsequent convex lens re-imaging the plume onto the (vertically oriented) slit of a 303 mm *f*/4 Czerny-Turner spectrograph (Shamrock SR-303i, Andor, Belfast, Northern Ireland). The latter was equipped with two diffraction gratings, having 150 and 2400 lines/mm and providing maximum spectral resolutions of 1.96 and 0.07 nm respectively, as well as a mirror for spectrally unresolved observations with the slit open to its maximum width of 2500 µm. The magnification of the optical system was set to unity, such that the total field of view was 2.5 × 6.5 mm; two images of a 500 µm grid (used for spatial calibration), obtained using the high resolution (2400 lines/mm) grating and the mirror, are presented together in Figure 2.7. It is clear from the figure that the spectrograph was able to provide reasonably good imaging performance, with only minor astigmatism evident as a slight field curvature in the sagittal plane.

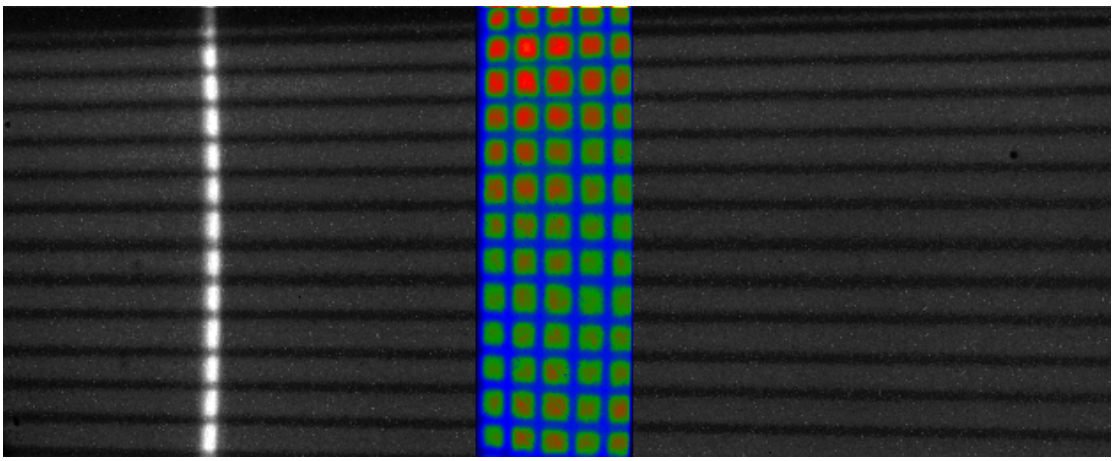

Figure 2.7: Composite image showing a 500 µm grid placed at the position of the laser focus and viewed spectrally unresolved with the slit fully open (central portion, in colour) and wavelength-dispersed with the slit width set to ≈ 30 µm (outer areas, in greyscale). A mercury line from the fluorescent room lighting can be observed on the left against a background of broad-band illumination.

The high spatial resolution of the imaging apparatus was useful for optical determination of the size of the laser spot, which was only possible *in vacuo* due to the otherwise confounding effects of air breakdown. Here, the nascent laser plasma (i.e., still during the laser pulse and before any significant expansion into the surrounding vacuum) was observed and the position of the focus altered so that the proper spot size was obtained in relation to the previously imaged calibration grid. The *post hoc* method discussed in the previous section was thus used mainly as a standard to confirm the accuracy and reproducibility of the more practical but indirect optical approach.

2.3.2 INTENSIFIED CCD

Images formed by the spectrograph were recorded using an intensified CCD (iCCD) camera (iStar DH-720, Andor) with an active area of 626 × 255 26 × 26 μm pixels and a minimum gate width of ≈ 2 ns. The maximum readout rate was ≈ 2.7 16-bit images/s at full resolution, necessitating the operation of the laser at a non-standard pulse repetition frequency of 2.5 Hz as stated in §2.1.1. In practice, the gate width was set to 10 ns, reflecting the approximate laser pulse duration; minimal laser plasma expansion occurred on this timescale and the recorded images therefore represented quasi-static states of the ablation plume at the chosen gate delay. The delays used in experiments ranged from 40 to 120 ns, measured in all cases from the peak of the optical pulse to the centre of the photocathode gate. Even given the image intensifier gain of $\approx 10^3$, relatively little optical emission was available to capture within a 10 ns period, so the CCD was cooled to −15°C and multiple images were accumulated in order to achieve a reasonable signal-to-noise ratio when recording weaker ionic and molecular emissions. The number of collections was chosen to be an integral multiple of 150, corresponding to the number of laser pulses produced during a single rotation of the target; this ensured that any shot-to-shot image shift due to imperfect target flatness would average out rather than be manifested as an unpredictable displacement of the accumulated images. Spatial resolution was limited to 26 μm by the CCD pixel size, although this was in any case comparable to the resolution of the imaging optics. Response nonlinearity was specified as less than 1% of the measured intensity.

Damage to the image intensifier tube by scattered laser radiation was avoided by the incorporation of a triple-wavelength (1064, 532, and 355 nm) notch filter (StopLine,

Semrock) into the imaging optics. However, a side effect of this was that any optical emission in the spectral region 520–536 nm was similarly blocked, as can be observed in Figure 2.8.

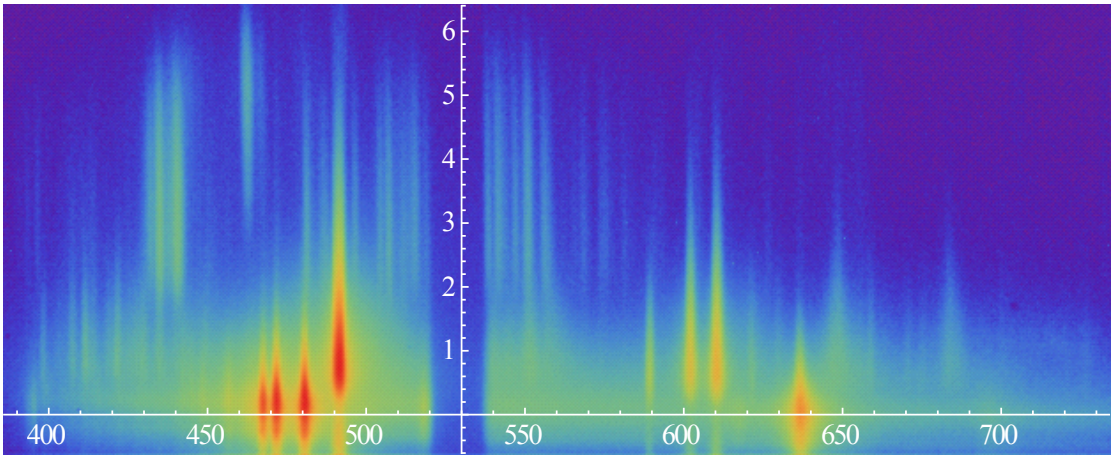

Figure 2.8: Example of a spatiospectrally-resolved optical emission image. The vertical axis represents spatial extent (distance in mm from the target surface) while the horizontal axis is the spectral dimension (values in nm). This image is of Zn ablated *in vacuo* at 355 nm, captured after a gate delay of 80 ns.

2.4 REFERENCES

[1] "Unstable Resonators", R. Paschotta, in *Encyclopedia of Laser Physics and Technology*, *Vol. 2*, 1st ed. (Wiley-VCH, Berlin, 2008). ISBN: 978-3-527-40828-3.

[2] W. Koechner, *Solid-State Laser Engineering*, 6th ed. (Springer, Berlin, 2006), p. 271. ISBN: 978-0-387-29094-2.

[3] *Ibid*., p. 275.

[4] "Polarized reflectance of aluminum and nickel to 532, 355 and 266 nm Nd:YAG laser beams for varying surface finish", H. Kwon and J. J. Yoh, *Optics & Laser Tech.* **44**, 1823 (2012). DOI: 10.1016/j.optlastec.2012.02.014.

[5] "YAG Lasers", R. Paschotta, in *Encyclopedia of Laser Physics and Technology*, *Vol. 2*, 1st ed. (*op. cit.*, *vide* [1]).

[6] "Effect of laser parameters on laser ablation and laser-induced plasma formation: A numerical modelling investigation", A. Bogaerts and Z. Chen, *Spectrochim. Acta B* **60** (9–10), 1280 (2005). DOI: 10.1016/j.sab.2005.06.009.

[7] J. F. Kenney and E. F. Keeping, *Mathematics of Statistics, Part 2*, 2nd ed. (Van Nostrand, Princeton, New Jersey, 1951), §7.8 (pp. 170–173).

[8] W. Koechner and M. Bass, *Solid-State Lasers: A Graduate Text*, 1st ed. (Springer, New York, 2003), §8.1 (pp. 280–284). ISBN: 978-0-387-95590-2.

CHAPTER 3: ABLATION OF ZINC AND ZINC OXIDE

The structure of this chapter will be as follows. Firstly, the crucial experimental parameters, i.e. the emission lines monitored and the irradiance range over which ablation was carried out, will be stated and justified, and details given of the analysis. The measured data will then be presented and discussed, beginning with Zn ablated at 355 nm *in vacuo*, proceeding *via* Zn under $p(O_2) = 50$ mTorr, to the case of ZnO *in vacuo*. Briefly, the situation of Zn ablation at 532 nm, including under increased oxygen pressure (up to 500 mTorr) will be discussed.

3.1 OVERVIEW OF EXPERIMENTS PERFORMED

3.1.1 ATOMIC AND IONIC LINES OBSERVED

Table 3.1: Summary of the (Zn^0)* lines observed in the present experiments. Data from measurements by Gullberg and Litzén.[1] Energies are given relative to the $[Ar]3d^{10}4s^2$ ($^1S_0$) ground state of Zn^0 and all terms implicitly include the $[Ar]3d^{10}$ core.

Air λ /nm	$\tilde{\nu}$ /cm^{-1}	Rel. intensity (arbitrary)	Lower state (Energy /cm^{-1})		Upper state (Energy /cm^{-1})
468.014	21360.9	2.35	4s4p $^3P_{0u}$ (32 311.3)	←	4s5s $^3S_{1g}$ (53 672.2)
472.216	21170.8	7.58	4s4p $^3P_{1u}$ (32 501.4)	←	4s5s $^3S_{1g}$ (53 672.2)
481.053	20781.9	7.73	4s4p $^3P_{2u}$ (32 890.3)	←	4s5s $^3S_{1g}$ (53 672.2)
636.235	15713.1	1.00	4s4p $^1P_{1u}$ (46 745.4)	←	4s4d $^1D_{2g}$ (62 458.5)

Notably, the lower states for the lines given in Table 3.1 are all substantially elevated in energy relative to the Zn^0 ground state. Transitions involving the $4s^2\ ^1S_0$ term all occur in the UV, and so could not be observed with the photographic optics used here.[a] This may be advantageous in the present context, however, since pronounced attenuation due to self-absorption may be expected for the lines of transitions that involve the ground state; whereas, assuming that Maxwell–Boltzmann statistics apply, this effect will be greatly reduced given lower states elevated by 4–6 eV.[b]

[a] Short wavelength cut-off ≈ 390 nm, possibly due to a construction employing optical epoxy that is transmissive only of visible wavelengths.

[b] Equivalent temperature 45 000–70 000 K (using a conversion factor of $hc/k_B \approx 1.44$ K/cm^{-1} or eV/$k_B \approx 11\,600$ K/eV). While the assumption of thermal equilibrium probably does not hold in general, particularly for very highly excited states of the ions (see later), it may be a reasonable approximation for Zn^0 relatively near to its ground state.

Table 3.2: Summary of the $(Zn^{1+})^*$ lines observed in the present experiments. From Gullberg and Litzén (*) and Crooker and Dick[2] (†). Energies are given relative to the $[Ar]3d^{10}4s$ ($^2S_{1/2}$) ground state of Zn^{1+} and all terms implicitly include the $[Ar]3d^{10}$ core, except for one, which has (as indicated) an $[Ar]3d^9$ ($^2D_{3/2}$) core.

Air λ /nm	$\tilde{\nu}$ /cm^{-1}	Lower state (Energy /cm^{-1})		Upper state (Energy /cm^{-1})
491.163*	20 354.2	$4d\ ^2D_{3/2,g}$ (96 909.9)	←	$4f\ ^2F_{5/2,u}$ (117 264.1)
492.401*	20 303.0	$4d\ ^2D_{5/2,g}$ (96 960.6)	←	$4f\ ^2F_{7/2,u}$ (117 263.6)
589.433†	16 960.8	$4p\ ^2P_{1/2,u}$ (48 481.0)	←	$[Ar]3d^94s^2\ ^2D_{3/2,g}$ (65 441.6)
602.118†	16 603.4	$5p\ ^2P_{1/2,u}$ (101 365.9)	←	$5d\ ^2D_{3/2,g}$ (117 969.3)
610.249†	16 382.2	$5p\ ^2P_{3/2,u}$ (101 611.4)	←	$5d\ ^2D_{5/2,g}$ (117 993.6)

Table 3.3: Summary of some of the more prominent $(Zn^{2+})^*$ lines observed in the present experiments. Energies and classifications by Dick[3]; present assignments based on *gf* values calculated by Kurucz and Peytremann[4]; line list and wavelengths tabulated by Hirata and Horaguchi[5]. Energies are given relative to the $[Ar]3d^{10}$ ($^1S_0$) ground state of Zn^{2+} and all terms implicitly include the [Ar] core.

Air λ /nm	$\tilde{\nu}$ /cm^{-1}	Lower state (Energy /cm^{-1})		Upper state (Energy /cm^{-1})
435.111	22 976.2	$3d^9(^2D_{5/2})4f\ ^3H_{5u}$ (257 796.0)	←	$3d^9(^2D_{5/2})5g\ ^3I_{6g}$ (280 772.2)
435.940	22 932.5	$3d^9(^2D_{3/2})4f\ ^1H_{5u}$ (260 613.1)	←	$3d^9(^2D_{3/2})5g\ ^1I_{6g}$ (283 545.6)
436.130	22 922.5	$3d^9(^2D_{3/2})4f\ ^3H_{4u}$ (260 623.1)	←	$3d^9(^2D_{3/2})5g\ ^3I_{5g}$ (283 545.6)
438.552	22 795.9	$3d^9(^2D_{3/2})4f\ ^3F_{2u}$ (260 805.9)	←	$3d^9(^2D_{3/2})5g\ ^3G_{3g}$ (283 601.8)
439.215	22 761.5	$3d^9(^2D_{5/2})4f\ ^3D_{3u}$ (258 075.7)	←	$3d^9(^2D_{5/2})5g\ ^3F_{4g}$ (280 837.2)
440.556	22 692.2	$3d^9(^2D_{5/2})4f\ ^3F_{4u}$ (258 178.3)	←	$3d^9(^2D_{5/2})5g\ ^3G_{5g}$ (280 870.5)
440.601	22 689.9	$3d^9(^2D_{5/2})4f\ ^3G_{5u}$ (258 171.2)	←	$3d^9(^2D_{5/2})5g\ ^3H_{6g}$ (280 861.1)
441.498	22 643.8	$3d^9(^2D_{3/2})4f\ ^1G_{4u}$ (260 988.4)	←	$3d^9(^2D_{3/2})5g\ ^1H_{5g}$ (283 632.2)
442.495	22 592.8	$3d^9(^2D_{5/2})4f\ ^3F_{3u}$ (258 277.7)	←	$3d^9(^2D_{5/2})5g\ ^3G_{4g}$ (280 870.5)
505.014	19 795.9	$3d^9(^2D_{3/2})5s\ ^1D_{2g}$ (217 846.8)	←	$3d^9(^2D_{3/2})5p\ ^1F_{3u}$ (237 642.7)
507.524	19 698.0	$3d^9(^2D_{5/2})5s\ ^3D_{3g}$ (214 878.0)	←	$3d^9(^2D_{5/2})5p\ ^3F_{4u}$ (234 576.0)
511.985	19 526.4	$3d^9(^2D_{5/2})5s\ ^3D_{2g}$ (215 340.5)	←	$3d^9(^2D_{5/2})5p\ ^3P_{1u}$ (234 866.9)
515.743	19 384.1	$3d^9(^2D_{3/2})5s\ ^3D_{1g}$ (217 663.7)	←	$3d^9(^2D_{3/2})5p\ ^3F_{2u}$ (237 047.8)
546.813	18 282.7	$3d^9(^2D_{3/2})4d\ ^1G_{4g}$ (219 360.0)	←	$3d^9(^2D_{3/2})5p\ ^1F_{3u}$ (237 642.7)
556.372	17 968.6	$3d^9(^2D_{5/2})4d\ ^3G_{5g}$ (216 607.4)	←	$3d^9(^2D_{5/2})5p\ ^3F_{4u}$ (234 576.0)
557.896	17 919.5	$3d^9(^2D_{5/2})4d\ ^3G_{4g}$ (216 464.5)	←	$3d^9(^2D_{5/2})5p\ ^3F_{3u}$ (234 384.0)

Because of the close proximity of many of the $(Zn^{2+})^*$ lines and the similarity in the energies of the terms, each set of lines (435.1–442.5, 505.0–515.7, and 546.8–557.9 nm) was considered in practice as a single unit. Additionally, for experiments involving the ablation of ZnO, the strongest ($4f \leftarrow 5g$) lines were obscured by overlapping $(O^{1+})^*$ emissions, so that observations of $(Zn^{2+})^*$ relied solely upon the much weaker $5s \leftarrow 5p$ and $4d \leftarrow 5p$ line groups.

To the author's knowledge, all work to date on the spectroscopy of Zn^{3+} has been conducted in the far UV, and therefore no visible lines have been reported in the literature. Assignments for at least seven lines observed between 462 and 464 nm in the present work were sought instead by considering all possible allowed transitions between the known energy levels of this ion. The majority of the 167 calculated lines occurring in the visible region involved a change of the $[Ar]3d^8$ core term, and hence could be discounted due to the small resulting transition probabilities.[c] The remaining three predicted lines, given in Table 3.4, are in some sense related to the weaker Zn^{2+} series given in the lower half of Table 3.3. The former, like the longest-wavelength Zn^{2+} group, are 4d ← 5p transitions; however, the terms indicate decreasing orbital angular momentum, as with the Zn^{2+} lines observed at 505.014, 507.524, and 515.743 nm.

Table 3.4: Core term–preserving, visible region (Zn^{3+})* lines predicted by the author from the known energy levels of Zn^{3+},[6] but not observed in the present experiments. Energies are given relative to the $[Ar]3d^9$ ($^2D_{5/2}$) ground state of Zn^{3+} and all terms implicitly include the $[Ar]3d^8$ ($^1G_4$) core.

Air λ /nm	$\tilde{\nu}$ /cm^{-1}	Lower state (Energy /cm^{-1})		Upper state (Energy /cm^{-1})
496.35	20 141	4d $^2D_{5/2,g}$ (353 124)	←	5p $^2F_{5/2,u}$ (373 265)
513.04	19 486	4d $^2D_{5/2,g}$ (353 124)	←	5p $^2F_{7/2,u}$ (372 610)
536.30	18 641	4d $^2D_{3/2,g}$ (354 624)	←	5p $^2F_{5/2,u}$ (373 265)

No 5s or 5g levels are described by Sugar and Musgrove, and so no lines could be predicted that would correspond more closely to the Zn^{2+} 5s ← 5p series or to the considerably stronger 4f ← 5g transitions. Noting, however, that the Zn^{1+} lines having the greatest observed intensity are the 4d ← 4f series, we may conjecture that those transitions involving pseudo-hydrogenic upper states (i.e., those having a core comparable to that of the ground state but with a single electron of highest possible l for given n) are preferentially observed. In justifying this we rely on the intuitive expectation that, since configurations with $(n, l = n - 1)$ possess nodeless radial wavefunctions, the overlap integral, which to first order determines the transition

[c] The decision to exclude these lines from consideration was supported empirically by the non-observation of core-changing transitions for (Zn^{2+})*. Although such a line was noted in the (Zn^{1+})* spectrum, this was very weak in relation to the substantial upper state population expected given the relative energetic accessibility of the latter.

probability, is maximized between any two such states. The Rydberg formula, which applies strictly only to hydrogenic configurations, but should hold approximately for sufficiently large n, is:

$$\tilde{\nu} = RZ^2\left(\frac{1}{n_1^{\,2}} - \frac{1}{n_2^{\,2}}\right) \qquad \text{Equation 3.1}$$

where $R = m_e e^4/(8\varepsilon_0{}^2 h^3 c) = 109\,737.316\ \text{cm}^{-1}$ is the Rydberg constant and $Z = +4$ is the formal nuclear (or ionic core) charge. Inserting $n_1 = 5$ and $n_2 = 6$ we obtain $\tilde{\nu} = 21\,460\ \text{cm}^{-1}$ ($\lambda = 466$ nm), which is in good agreement with the observed lines lying in the region 21551–21645 cm^{-1} (462–464 nm). We therefore tentatively assign these lines as belonging to the 5g ← 6h series of Zn^{3+}.

Fortunately, all of the oxygen lines observed in the present work have been assigned in the literature, and are summarized in Table 3.5 and Table 3.6. The latter of these is divided into three sections, the second and third of which list lines that overlapped (both spatially and spectrally) with those of Zn^{2+} and Zn^{3+}, respectively. This overlap rendered the corresponding measurements either unreliable or altogether impossible when these lines were observed together, which (along with the limited resolution of the grating employed) accounts for the conspicuous absence of certain datasets from the following analysis.

Table 3.5: Summary of the (O^0)* lines observed in the present experiments. Data as given by Moore.[7] Energies are given relative to the $[He]2s^22p^4$ ($^3P_2$) ground state of O^0 and all terms implicitly include the $[He]2s^22p^3$ ($^4S_{3/2}$) core.

Air λ /nm	$\tilde{\nu}$ /cm^{-1}	Rel. intensity (arbitrary)	Lower state (Energy /cm^{-1})		Upper state (Energy /cm^{-1})
777.194	12 863.3	1.16	3s $^5S_{2u}$ (73 768.2)	←	3p $^5P_{3g}$ (86 631.5)
777.417	12 859.6	1.08	3s $^5S_{2u}$ (73 768.2)	←	3p $^5P_{2g}$ (86 627.8)
777.539	12 857.6	1.00	3s $^5S_{2u}$ (73 768.2)	←	3p $^5P_{1g}$ (86 625.8)

Table 3.6: Partial summary of the $(O^{1+})^*$ lines observed in the present experiments. Data as given by Wenåker[8], Martin *et al.*[9], and Eriksson[10]. Energies are given relative to the $[He]2s^22p^3$ ($^4S_{3/2}$) ground state of O^{1+} and all terms implicitly include the $[He]2s^22p^2$ ($^3P_0$) core.

Air λ /nm	$\tilde{\nu}$ /cm^{-1}	Rel. intensity (arbitrary)	Lower state (Energy /cm^{-1})		Upper state (Energy /cm^{-1})
406.962	24 565.3	1.18	3p $^4D_{1/2,u}$ (206 730.8)	←	3d $^4F_{3/2}$ (231 296.1)
406.989	24 563.8	1.24	3p $^4D_{3/2,u}$ (206 786.3)	←	3d $^4F_{5/2}$ (231 350.1)
407.216	24 550.1	1.35	3p $^4D_{5/2,u}$ (206 877.9)	←	3d $^4F_{7/2}$ (231 428.0)
407.586	24 527.7	1.41	3p $^4D_{7/2,u}$ (207 002.5)	←	3d $^4F_{9/2}$ (231 530.2)
407.884	24 509.8	1.00	3p $^4D_{3/2,u}$ (206 786.3)	←	3d $^4F_{3/2}$ (231 296.1)
408.511	24 472.2	1.12	3p $^4D_{5/2,u}$ (206 877.9)	←	3d $^4F_{5/2}$ (231 350.1)
409.293	24 425.5	1.00	3p $^4D_{7/2,u}$ (207 002.5)	←	3d $^4F_{7/2}$ (231 428.0)
409.725	24 399.9	1.00	3p $^4P_{1/2,u}$ (208 346.1)	←	3d $^4D_{3/2}$ (232 746.0)
410.499	24 353.7	1.06	3p $^4P_{3/2,u}$ (208 392.3)	←	3d $^4D_{3/2}$ (232 746.0)
411.922	24 269.6	1.29	3p $^4P_{5/2,u}$ (208 484.2)	←	3d $^4D_{7/2}$ (232 753.8)
412.028	24 263.4	1.00	3p $^4P_{5/2,u}$ (208 484.2)	←	3d $^4D_{5/2}$ (232 747.6)
434.943	22 985.1	1.35	3s $^4P_{5/2}$ (185 499.1)	←	3p $^4P_{5/2,u}$ (208 484.2)
436.689	22 893.2	1.18	3s $^4P_{5/2}$ (185 499.1)	←	3p $^4P_{3/2,u}$ (208 392.3)
441.491	22 644.2	1.59	3s $^2P_{3/2}$ (189 068.5)	←	3p $^2D_{5/2,u}$ (211 712.7)
441.697	22 633.6	1.47	3s $^2P_{1/2}$ (188 888.5)	←	3p $^2D_{3/2,u}$ (211 522.1)
463.886	21 551.0	1.18	3s $^4P_{1/2}$ (185 235.3)	←	3p $^4D_{3/2,u}$ (206 786.3)
464.181	21 537.3	1.29	3s $^4P_{3/2}$ (185 340.6)	←	3p $^4D_{5/2,u}$ (206 877.9)
464.913	21 503.4	1.41	3s $^4P_{5/2}$ (185 499.1)	←	3p $^4D_{7/2,u}$ (207 002.5)
465.084	21 495.5	1.18	3s $^4P_{1/2}$ (185 235.3)	←	3p $^4D_{1/2,u}$ (206 730.8)

3.1.2 IRRADIANCE RANGE INVESTIGATED

The laser irradiance range employed in the present work was guided by the intention that the experimental conditions employed be comparable to those used for pulsed laser deposition (PLD). As a result, the maximum irradiance employed was substantially less than in many other laser ablation studies, principally due to the intentionally loosely focused incident beam, combined with a relatively long laser pulse duration. Initial experiments at 532 nm were therefore conducted with at most $I \approx 6$ GW/cm^2, corresponding to a fluence $F \approx 50$ J/cm^2, which is already substantially greater than generally required for PLD. Later measurements and all those performed at 355 nm extended the irradiance range upwards toward $I \approx 15$ GW/cm^2 after deviations from a simple power law trend (cf. §3.2.1) became evident. Furthermore, the regime close to the ablation threshold was inaccessible due to the limited sensitivity of the diagnostic technique, necessitating irradiance $I \gtrsim 1$ GW/cm^2 ($F \gtrsim 10$ J/cm^2) in order to capture sufficient optical emission. Within these bounds,

care was taken to make measurements for sufficiently many different irradiances, with typically $N = 11$ or 18 collections (for each time-gate) per experiment.

3.1.3 CHOICE OF GATE DELAYS

The delay between the laser pulse and the image intensifier gate was dictated by the requirement for the emission lines of each species to be adequately spectrally resolved while also remaining spatially inside the imaged region. In the following, the gate time is denoted as t_g, with optical excitation occurring at $t_0 \leq t_g$; both of these values are given relative to their respective temporal centres and the gate width was held constant at 10 ns, as described in the previous chapter. Continuum (bremsstrahlung and black-body) emission and pressure and/or Stark broadening effects dominate in the early plasma, such that resolution of individual species is difficult for $t_g \lesssim t_0 + 30$ ns. The rate of expansion of the ablation products depends on their mass and charge, with the lightest and most highly charged species gaining the highest velocities. In the present experiments, the displacement of emitting Zn^{2+} and Zn^{3+} ions relative to the target was sufficient by $t_g = t_0 + 40$ ns for adequate resolution of these species. However, little spatial separation between Zn^0 and Zn^{1+} was evident within this time, and moreover, the emissions of the lower charge states remained significantly broadened until around 60 ns after the optical pulse. Gate times $t_g \geq t_0 + 60$ ns were therefore employed, with the maximum delay chosen as the latest time for which Zn^{3+} lines remained completely within the field of view. In the initial experiments $t_{g,max}$ was chosen as $t_0 + 120$ ns, with this value being revised to $t_0 + 90$ ns in subsequent experiments after it became clear that in some cases $Zn^{2/3+}$ is more spatially extended and has velocity more strongly increasing with irradiance than was originally thought. Although measurements could usefully have been collected with greater time resolution or (for a subset of the monitored species) over a wider interval, the selection of a more limited set of gate delays was necessary in practice so that experiments could be completed within a reasonable time.

3.2 ANALYTICAL METHODS AND METHODOLOGY

3.2.1 YIELD MEASUREMENTS

"Optical emission yield", Y, was determined for each species of interest by summing over those spectral lines that were both sufficiently intense as to be identifiable and

not subject to interference from those of another emitter (i.e., free from spectral or spatial overlap in every image recorded during a given experiment). If multiphoton ionization (MPI) contributes significantly to the total ion yield, as has been demonstrated for carbon (ablated with 9 ns pulses at 1 064 nm) by Harilal *et al*.[11], we expect the ionization probability far below saturation to go as the n^{th} power of the photon flux,[12] where n is the order of the multiphoton process. As described in the previous chapter, the present work has been limited to the case of relatively low irradiance using defocused nanosecond laser pulses, so operation in the perturbative regime was assumed. Using a weighted nonlinear least squares procedure,[d] values of Y were thus fitted to a power law in the irradiance I, i.e.

$$\hat{Y}_{t_g} = \exp(A_{t_g}) \cdot I^{n_{t_g}} \qquad \text{Equation 3.2}$$

where A and n are fitting parameters and the subscript t_g denotes that these values were obtained separately for the data collected at each temporal offset (i.e., photocathode gate delay) relative to the laser pulse. Despite the initial expectation that saturation of the MPI yield would not be achieved in practice, it was observed in many cases that a single trend of the form given by Equation 3.2 did not suffice, with a second, smaller power law exponent being required in order to obtain an adequate fit to the data at high I. Any two such power laws, to which we may arbitrarily assign the labels 1 and 2, intersect at a "threshold" irradiance that is given from the corresponding values of A and n by

$$I_{\text{threshold}} = \exp\left(\frac{A_2 - A_1}{n_1 - n_2}\right) \qquad \text{Equation 3.3}$$

and which might be understood as signifying the point of transition between the low- and high-irradiance regimes, and hence the different physical processes dominating in each case.

[d] Namely, the Levenberg-Marquardt algorithm, as implemented in *Mathematica* (Wolfram Research, Champaign, Illinois). No serious difficulties of convergence were encountered, and the fitted parameters reported may be considered the globally optimal values.

While Equation 3.2 provided for the most part a useful quantitative description of the scaling of optical emission yield with irradiance, it was not possible to interpret the exponent n as relating directly to the order of any multiphoton process because its value was typically around (or even somewhat below) unity. This may suggest an indirect (and possibly multi-step) formation mechanism for the electronically excited product species, and could then reflect a sub-linear irradiance dependence of the total quantity of material ablated: Arnold and Bityurin, for example, have proposed a volume photothermal decomposition (phase explosion) model,[13] wherein the exponent associated with mass removal is equal to ½. Given this underlying scaling, and the fact that such a mechanism would not be expected to result in an initially highly ionized plasma, a linear dependence (for example) of the product species yield on irradiance might then be taken to imply multiphoton ionization by 2-photon absorption, since 1 = ½ × 2. Indeed, as will be seen in the following, the value of n lay close to ½ for the neutral atoms in all cases and increased monotonically with increasing charge of the associated species.

The empirical success of Equation 3.2 suggested the possible applicability of a more physically realistic family of power law models, notwithstanding the somewhat ambiguous theoretical basis for this particular functional form. In the first instance, an explicit threshold irradiance, $I_{\text{threshold}}$ (the meaning of which should not be confused with the same symbol as it appears in Equation 2.3), was incorporated, below which no optical emission could be observed:

$$\hat{Y}_{t_g} = \exp(A_{t_g}) \cdot (I - I_{\text{threshold}})^{n_{t_g}} \qquad \text{Equation 3.4}$$

Furthermore, under the assumption that ablation occurs without any appreciable delay, conservation of mass clearly requires the same $I_{\text{threshold}}$ for all time-gates t_g; this value was hence obtained through a simultaneous fit to all of the available experimental results. Provided that the other fitting parameters were well determined, the consideration of a large number of measurements (≈ 72) enabled $I_{\text{threshold}}$ to be obtained to relatively high precision in this way.

If justified by the data, we may additionally choose to assume that no dynamical effects (e.g., collisional ionization, electron-ion recombination, etc.) exist that would cause the exponent n to vary with time. As a result, the $\{n_{t_g}\}$ are replaced in the fitted models simply by n, and furthermore the scale factors A_{t_g} become independent of time and irradiance, and thus directly comparable to each other:

$$\hat{Y}_{t_g} = \exp(A_{t_g}) \cdot (I - I_{threshold})^n \qquad \text{Equation 3.5}$$

Finally, we may incorporate (where appropriate) not only a fixed exponent but also, under approximation to exponential decay of the optical emission yield with time, a rate constant k; this may be compared with a corresponding Einstein A-coefficient, if the latter is known. The number of free parameters is thus reduced to four, i.e. A (the extrapolated scale factor at $t_g = t_0$), k, $I_{threshold}$, and n, all of which possess a reasonably straightforward physical interpretation:

$$\hat{Y}_{t_g} = \exp\left[A - k(t_g - t_0)\right] \cdot (I - I_{threshold})^n \qquad \text{Equation 3.6}$$

3.2.2 SPATIAL PROFILES

The spatial distribution of each species was evaluated by summing a section of each spatiospectral image over the spectral dimension only, with the chosen blocks being short compact sections of the spectrum within which a single emission line (or, for weak emissions, several lines due to a single species) occurred. The resulting profiles are presented below in terms of either displacement from the target surface or average velocity (i.e., displacement at a given time), as appropriate for the species under consideration. It should be pointed out that the data extracted from each image have been independently normalized in the figures presented here, and that Savitzky-Golay filtering[14] has been applied in order to attenuate visually distracting noise. The parameters used in deriving the filter coefficients were carefully chosen in order to preserve the profile shapes.

3.3 355 NM ABLATION OF ZINC AND ZINC OXIDE

3.3.1 ZINC *IN VACUO*

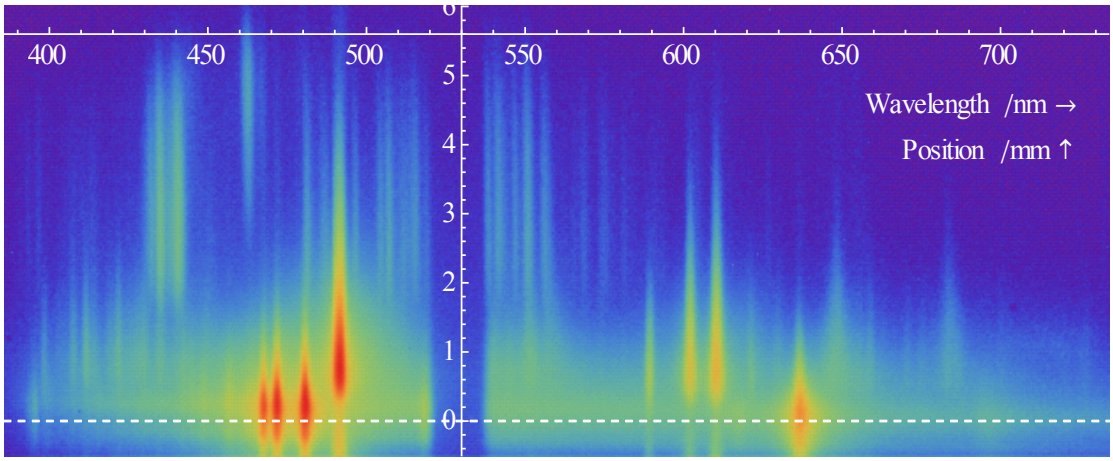

Figure 3.1: Spatiospectral image recorded at $t_g = t_0 + 80$ ns subsequent to the 355 nm ablation of Zn *in vacuo* with irradiance $I = 6.9$ GW/cm^2. The dashed line indicates the approximate position of the target surface.

Probably the most prominent qualitative feature of the spatiospectral images obtained in the present work is the spatial separation between charge states, which in practice facilitates the assignment of observed spectral features to particular species solely by consideration of their relative position (or, equivalently, velocity), as shown in Figure 3.2, below. However, while this effect was noted in some of the earliest studies in the field,[15] and appears to be a ubiquitous feature of laser plasma plumes, some disagreement persists over the correct explanation for the observed behaviour.

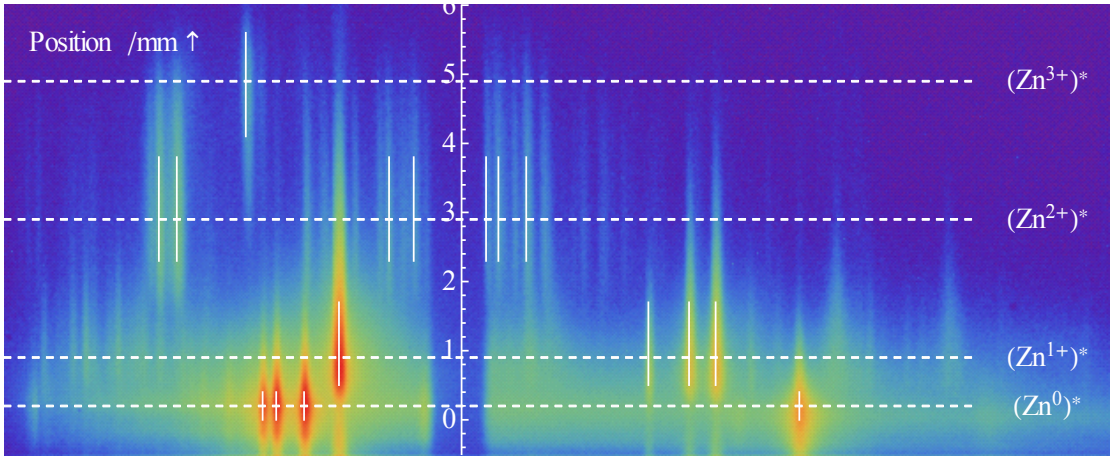

Figure 3.2: Annotated reproduction of the image given in Figure 3.1, with the approximate position of each species indicated and several of the more prominent emission lines marked (cf. Table 3.1–Table 3.4).

In the ultrashort-pulse regime, the observed charge separation and consequent ion acceleration is fully explained by a (surface) Coulomb explosion mechanism, which has been described in detail by Gamaly *et al.*[16] By their account, multiphoton and avalanche ionization processes (as described earlier) lead to near-complete ionization and a substantial free electron yield in the target bulk within the first few tens of femtoseconds of irradiation. Thereafter, inverse bremsstrahlung absorption dominates, and since the characteristic timescales for electron-ion heat transfer (≈ 5 ps) and electron diffusion ($\gg 10$ ps) both greatly exceed the pulse duration, laser energy coupled into the nascent plasma contributes almost solely to the heating of the electron gas. At the ablation (or plume formation) threshold, the thermal energy of the latter becomes comparable to the Fermi energy, so that a fraction of the electrons possess energies significantly in excess of the work function and are able to escape from the target with kinetic energy greater than the lattice binding energy.[e] The resulting charge separation produces an electric field sufficiently strong to accelerate ions out of the target, where the magnitude of the acceleration and hence the kinetic energy gained clearly depend on the ionic charge.

Such a model can apply, however, only if the probability of multiphoton ionization is high and laser energy is absorbed by the resulting free electrons more rapidly than it can be dissipated. For laser pulses of duration $\tau = 10$–100 ps (threshold irradiance $I_{\text{thresh}} = 10^{10}$–$10^{11}$ W/cm^2), these extreme non-equilibrium dynamics no longer exist due to the increased importance of electron-ion Coulomb coupling, while with $\tau \approx 1$–10 ns ($I_{\text{thresh}} \approx 10^{8}$–$10^{9}$ W/cm^2) the ionization fraction within the solid is negligible and so inverse bremsstrahlung absorption is insignificant. In the latter case, thermal equilibrium can be assumed between the electrons and ions in the irradiated volume, such that ordinary vaporization is the primary desorption mechanism. Peurrung *et al.*[18] have suggested that, for metals, nanosecond irradiation very near to the ablation threshold may nevertheless yield sufficient photoelectrons to form a space charge layer, the expansion of which, on collapse of the laser field, is capable of imparting a modest acceleration to thermally desorbed ions. However, the maximum kinetic energy gained through this process (which is limited because of the effect of

[e] Wendelen *et al.*[17] have recently argued that, at more moderate irradiance, photoelectron emission probably dominates over the thermionic mechanism proposed by Gamaly *et al*.

space charge on the photoelectron yield itself) is predicted theoretically by these authors as 3.3 eV, which, as will be seen in the following, is far smaller than observed in the present work. A wide variety of processes have been suggested by various authors that might account for the experimentally established relationship between charge state and translational kinetic energy, although most of these are either inapplicable to the present scenario or manifestly incompatible with our observations. Therefore, we discuss further below, in the context of the present findings, only those propositions that both possess clear explanatory power and are relevant to the current situation.

(Zn^0)*

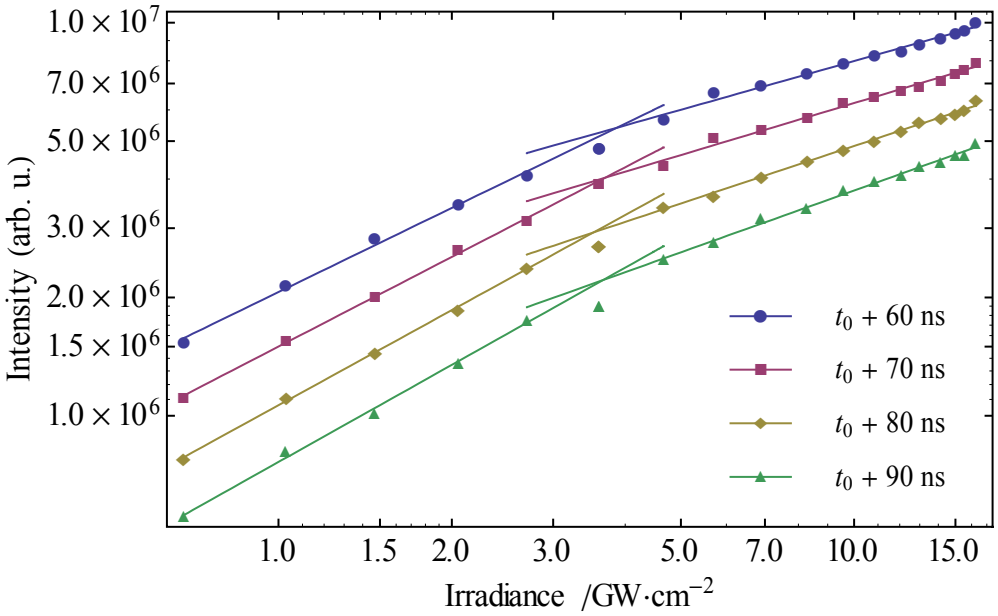

Figure 3.3: Variation with laser irradiance of the optical emission yield of (Zn^0)*, as produced in the 355 nm ablation of Zn *in vacuo*. The overlaid line segments correspond to power laws per Equation 3.2.

The first, and simplest, situation considered in the present work is the ablation of Zn *in vacuo*. The optical emission yield of (Zn^0)*, as assessed by the total integrated intensity of all of the lines given in Table 3.1, is presented in Figure 3.3 for various time-gates t_g subsequent to ablation at 355 nm. In justifying the aggregation of emission on dissimilar lines, we note that the model parameters obtained by considering each line individually are (within experimental error) identical up to the absolute magnitude of the scale parameter.

Table 3.7: Fitted scale and exponent (according to Equation 3.2) for each of the trends indicated in Figure 3.3, corresponding to the dependence of the optical emission yield of $(Zn^0)^*$ on the irradiance at 355 nm for the ablation of Zn *in vacuo*.

t_g	$0.68 \leq I \leq 2.70$ GW/cm^2		$4.67 \leq I \leq 16.28$ GW/cm^2	
	Scale A	Exponent n	Scale A	Exponent n
t_0 + 60 ns	14.540(18)	0.711(30)	14.946(39)	0.411(18)
t_0 + 70 ns	14.221(9)	0.757(15)	14.636(40)	0.439(18)
t_0 + 80 ns	13.877(8)	0.803(13)	14.277(22)	0.486(10)
t_0 + 90 ns	13.545(17)	0.821(26)	13.932(29)	0.522(13)

While the empirical power law dependence on irradiance (Equation 3.2) accurately matches the observed trend, there are two distinct regimes, corresponding to an abrupt decrease of the fitted exponent at $I_{threshold} = 3.68(18)$ GW/cm^2 (by Equation 2.3) from 0.77(6) to 0.49(6).[f] Notably, the exponents remain below unity in both cases, indicating that utilization of the available laser energy in the production of $(Zn^0)^*$ becomes progressively less efficient as irradiance is increased. Given the relatively low melting point and high vapour pressure of metallic zinc (692.7 K, and 152.8 mTorr at the melting point,[19] respectively), it may be argued that a dense (if only slightly ionized) zinc plasma might readily form, even for very small pulse energy, which would reduce the irradiance at the target through absorption, scattering, or Debye shielding. According to this model, one might consider the threshold irradiance to signify the transition between partial and total attenuation of the incident radiation, and therefore the progression from direct ablation to plasma etching as the principal mechanism of Zn atom production.

[f] These values are averages for all time-gates $t_g = t_0 + \{60, 70, 80, 90\}$ ns.

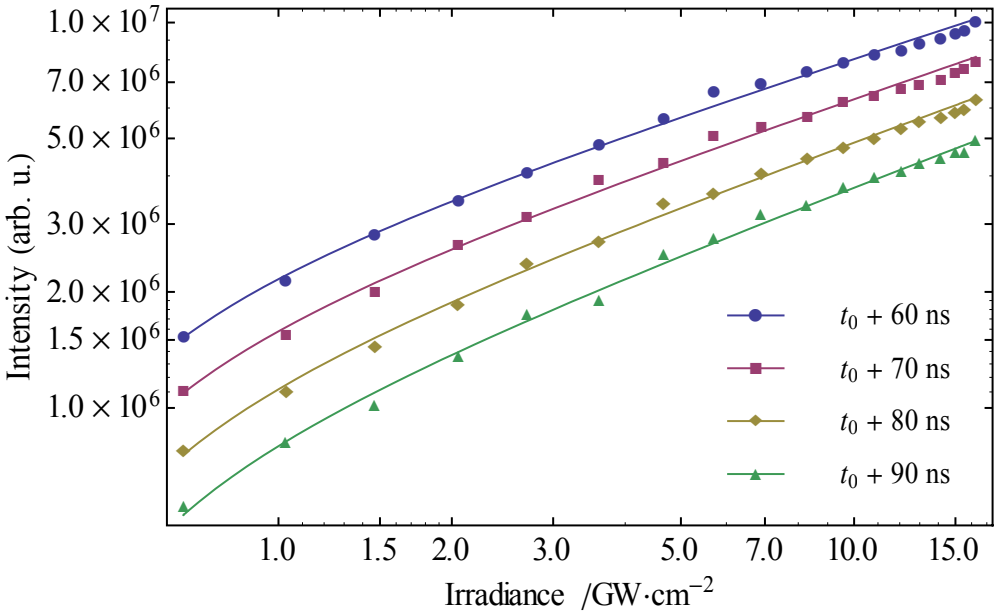

Figure 3.4: Variation with laser irradiance of the optical emission yield of $(Zn^0)^*$, as produced in the 355 nm ablation of Zn *in vacuo*. The overlaid curves are given by Equation 3.4 as fitted to the data.

A different interpretation is suggested, however, by the more physically realistic model of Equation 3.4, according to which a single exponent is assumed for the entire irradiance range, and the threshold irradiance signifies the onset of $(Zn^0)^*$ emission rather than the boundary between the applicability of separate scaling laws (Figure 3.4 and Table 3.8). The fitted "appearance threshold" of 0.393(18) GW/cm^2 corresponds to a fluence of 3.22(13) J/cm^2, and as such agrees quite well with the value of 3.12 J/cm^2 reported by Cabalín and Laserna[20] for the ablation of Zn at 266 nm.[g] The exponent in this case is very close to 0.5 (with $n = 0.50(1)$ obtained by fitting Equation 3.5 for all time-gates simultaneously), and this value is strongly suggestive of the photothermal model proposed by Arnold and Bityurin,[13] which predicts that the quantity of ablated material scales as the square root of fluence. While the latter was constructed in order to describe the ablation of strongly absorbing organic polymers, it is nonetheless applicable to metals in the restricted case of ablation *via*

[g] Mosteller and Wooten[21] have described the reflectance of Zn as being essentially constant between 190 and 560 nm. Their report, however, relates to a vacuum-cleaved Zn single crystal at 96 K, and the present author was not able to find any published work on the reflectivity of liquid Zn at high temperatures.

phase explosion, the occurrence of which has been established both theoretically[22] and experimentally[23] for aluminium.

Table 3.8: Fitted threshold, scale, and exponent (according to Equation 3.4) for each of the trends indicated in Figure 3.4, corresponding to the dependence of the optical emission yield of (Zn^0)* on the irradiance at 355 nm for the ablation of Zn *in vacuo*.

$I_{threshold}$	t_g	$0.68 \leq I \leq 16.28$ GW/cm^2	
		Scale A	Exponent n
0.393(18) GW/cm^2	t_0 + 60 ns	14.823(15)	0.476(8)
	t_0 + 70 ns	14.524(17)	0.502(9)
	t_0 + 80 ns	14.193(20)	0.533(11)
	t_0 + 90 ns	13.866(25)	0.559(14)

In order to determine whether phase explosion is plausible in the case of Zn, it is necessary to consider whether the material can become superheated under laser irradiation. In the absence of a suitable thermodynamic model, we attempt an argument based on the comparison of the thermophysical properties of zinc with those of aluminium. Zn possesses poorer thermal conductivity than Al and has a comparable volumetric heat capacity (2.77 vs. 2.42 J K^{-1} cm^{-3}),[19] while its critical temperature has been identified by Otter *et al.*[24] as about 3600 K, i.e. rather less than the value of ≈ 6700 K given by Morel *et al.*[25] for Al. Furthermore, the UV reflectivity of zinc is less than that of aluminium. Since the properties enumerated above are all favourable toward phase explosion as an explanation for the scaling of the (Zn^0)* optical emission yield with irradiance, we conclude that there is no obvious justification for excluding this possibility based on the current data alone. Moreover, Amer *et al.*[26] have recently proposed, based on an interferometric imaging study, that the ablation of Zn does indeed proceed *via* this mechanism for a fluence of only 5 J/cm^2 at 1064 nm, whereas the minimum fluence employed here was 8.10 J/cm^2 (corresponding to an irradiance of 0.68 GW/cm^2).

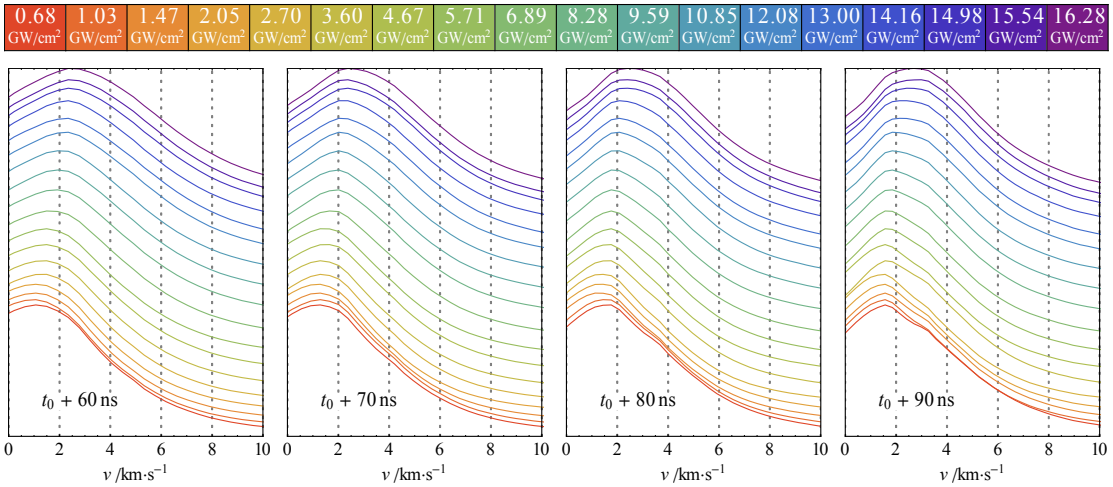

Figure 3.5: Spatial distribution of $(Zn^0)^*$ optical emission resulting from the 355 nm ablation of Zn *in vacuo*. Results are presented in terms of the average velocity required for an emitting Zn atom to have arrived at a given position in the specified time.

The spatial distribution of optical emission from $(Zn^0)^*$ is presented in Figure 3.5, wherein each curve has been independently normalized, and average velocities (the abscissae) have been calculated from the corresponding positions relative to the target surface and the appropriate delay subsequent to ablation. The vertical offset (applied at the common baseline; not shown in the figure) is proportional to the irradiance, so that trends in the measured profiles can more easily be related to the change in this parameter. $(Zn^0)^*$ does not appear to be subject to significant acceleration in the interval $t_g = t_0 + 60$–90 ns, with the modal velocity remaining approximately constant at ≈ 2 km/s (KE ≈ 1.4 eV). A modest shift to increasing average velocity that is nearly linear in irradiance is, however, observable, which accounts for a translational kinetic energy gain of around 2 eV over the irradiance range investigated. The data are reasonably consistent with the Maxwell–Boltzmann distribution of velocities in a one-dimensional gas of non-interacting Zn atoms at a temperature of 8–12 eV (largely independent of irradiance). While such a model is clearly not particularly physically realistic, this value is nonetheless useful as an order-of-magnitude estimate of the initial plasma temperature.

$(Zn^{1+})^*$

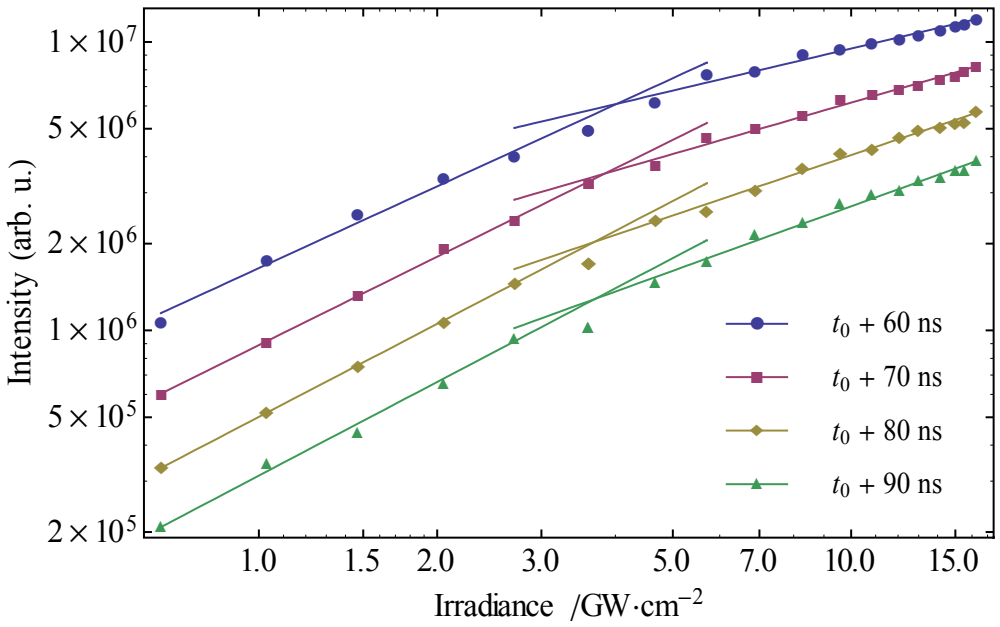

Figure 3.6: Variation of the optical emission yield of $(Zn^{1+})^*$ with laser irradiance, as recorded subsequent to the ablation of Zn *in vacuo* at 355 nm. The overlaid line segments correspond to power laws per Equation 3.2.

The scaling of optical emission yield with irradiance for $(Zn^{1+})^*$, as shown in Figure 3.6, appears qualitatively similar to that of $(Zn^0)^*$, including the threshold irradiance of 3.8(2) GW/cm^2, which is essentially equal to that obtained previously for the neutral species. In contrast to the prior case, however, the power law exponents are somewhat greater; in particular, those applicable to irradiance below the threshold take values close to unity, corresponding to proportionality between irradiance and the measured optical emission intensity.

Table 3.9: Fitted scale and exponent (according to Equation 3.2) for each of the trends indicated in Figure 3.3, corresponding to the dependence of the optical emission yield of $(Zn^{1+})^*$ on the irradiance at 355 nm for the ablation of Zn *in vacuo*.

t_g	$0.68 \leq I \leq 2.70$ GW/cm^2		$4.67 \leq I \leq 16.28$ GW/cm^2	
	Scale A	Exponent n	Scale A	Exponent n
t_0 + 60 ns	14.313(43)	0.942(64)	14.951(65)	0.484(29)
t_0 + 70 ns	13.698(17)	1.018(25)	14.270(55)	0.592(24)
t_0 + 80 ns	13.125(7)	1.071(11)	13.615(47)	0.694(21)
t_0 + 90 ns	12.656(38)	1.079(54)	13.096(63)	0.742(27)

Since a linear relationship is to be expected when laser energy is efficiently utilized in the formation of ablation products (and if multiphoton ionization does not play a significant role), further consideration of absorption within the plasma appears warranted as a possible explanation for the threshold. As discussed previously, the scaling of the (electron-ion) IBA coefficient α can be approximated as

$$\alpha \sim \frac{N_e}{A} I\lambda^2 \hat{T}^{-5/2} \qquad \text{Equation 3.7}$$

where N_e/A is the areal electron density and $\hat{T}$ is the temperature in eV. However, this expression is less useful for present purposes due to the severe approximation (that the plasma behaves as an ideal gas confined by radiation pressure) introduced earlier in order to remove the (unknown) volume of the electron gas from consideration. Proceeding without this assumption, we find instead, again to first order, that

$$\frac{P_{abs}}{V} \approx 2.9 \times 10^{-36} n_e{}^2 I\lambda^2 \hat{T}^{-3/2}. \qquad \text{Equation 3.8}$$

Since $\frac{P_{abs}}{V} = \frac{P_{abs}}{Ad}$ (where d is the depth of the plasma) and $I = \frac{P}{A}$, we have

$$\frac{P_{abs}}{P} = \alpha \approx 2.9 \times 10^{-36} n_e{}^2 d\lambda^2 \hat{T}^{-3/2} \qquad \text{Equation 3.9}$$

with $\alpha = 1$ corresponding to total absorption of incident optical power. Considering a quasi-neutral plasma, and so taking the spatial distribution of Zn^{1+} as indicative of that of the free electrons, we find that, with a constant mean expansion velocity of ≈ 10 km/s (per Figure 3.8, below), $d \approx 50$ μm at $t = t_0 + 5$ ns (i.e., mid-way through a 10 ns laser pulse). Assuming thermal equilibrium at $\hat{T} \approx 10$ eV at this early stage from the Maxwell–Boltzmann fit to the Zn^0 velocity distributions, we thus obtain a critical electron density of $n_e \approx 1.3 \times 10^{21}$ cm^{-3} for which laser radiation is completely absorbed by the plasma before reaching the target. It should be acknowledged, however, that given the treatment of the plasma as being fully ionized, this value is probably only accurate to within about an order of magnitude.

In calculating the corresponding density of Zn atoms/ions, the Saha-Langmuir equation may be employed to account for a combination of thermionic emission from the target surface (Equation 3.10) and thermal autoionization[h] of the vapour (Equation 3.11):[28]

$$\frac{n_i}{n_0} = \frac{g_i}{g_0} \exp\left(\frac{\phi - \mathrm{IP}_i}{\hat{T}} \right) \qquad \text{Equation 3.10}$$

$$\frac{n_{i+1}}{n_i} = \frac{2}{\lambda_\mathrm{T}^{\,3}} \frac{g_{i+1}}{g_i} \exp\left(- \frac{\mathrm{IP}_{i+1} - \mathrm{IP}_i}{\hat{T}} \right) \qquad \text{Equation 3.11}$$

where n_i is the number of ions of charge i, g_i is the statistical weight (degeneracy) of the i^{th} charge state, ϕ is the surface work function, equal to 3.63 eV,[19] and IP_i is the i^{th} ionization potential. The factor $2/\lambda_\mathrm{T}^{\,3}$, where

$$\lambda_\mathrm{T} = \sqrt{\frac{h^2}{2\pi m_\mathrm{e} e \hat{T}}} \qquad \text{Equation 3.12}$$

is the thermal de Broglie wavelength, is necessary when considering Bose or Fermi gases, but becomes unity in the classical limit ($n_e \lambda_\mathrm{T}^{\,3} \ll 1$), whereupon Maxwell–Boltzmann statistics apply.[29] Presently, $\lambda_\mathrm{T} = 2.2 \times 10^{-8}$ cm, so we may confidently neglect quantum effects; Equation 3.11 thus becomes:

$$\frac{n_{i+1}}{n_i} = \frac{g_{i+1}}{g_i} \exp\left(- \frac{\mathrm{IP}_{i+1} - \mathrm{IP}_i}{\hat{T}} \right) \qquad \text{Equation 3.13}$$

Here we assume that the pre-factor is near unity due to the high temperature and consequent population of many energy levels for each charge state. The first I. P. of Zn is 75 769.33 cm^{-1} (9.394 203 eV) according to Tukhlibaev and Alimov,[30] while Sugar and Musgrove[6] give the second as 144 893 cm^{-1} (17.9644 eV). The effective atomic volume for liquid zinc (density 6.570 $\mathrm{g/cm}^3$, mass 65.38 g/mol) is

[h] While the existence of such a phenomenon is intuitively reasonable and the physical descriptions of the process by Saha and Langmuir have long been known, the author was surprised to discover that Frölich and Merkli[27] have succeeded in formulating a rigorous (and highly involved) mathematical proof of this fact.

1.652×10^{-23} cm^3, suggesting an average interatomic distance of 2.547×10^{-8} cm and a surface density of 1.541×10^{15} cm^{-2}. Assuming the 7.4×10^{11} Zn atoms present at the target surface within the irradiated area of 4.8×10^{-4} cm^2 to be in thermal equilibrium with the plasma above, each of these is responsible (by Equation 3.10) for the emission of an average of 0.56 electrons into a 2.4×10^{-6} cm^3 volume. The electron density due to thermionic emission is therefore 1.7×10^{17} cm^{-3}, which is an insignificant contribution to the total of 1.3×10^{21} cm^{-3} required if IBA is to dominate. However, due to thermal autoionization (Equation 3.13), we also have 1.56 electrons on average for each Zn atom or ion in the vapour, the number density of which must therefore be 2.0×10^{21} cm^{-3} at the critical electron density, or approximately 1/30 that of liquid Zn. Since the atomization and ionization of only 0.52 μg of Zn is necessary in order to achieve this (requiring 1.0 mJ and 7.2 mJ of energy, respectively, which should be compared with 7.6 mJ available from the laser field at the threshold irradiance), we conclude that plasma absorption is a plausible explanation for the observed reduction in ablation efficiency with increasing irradiance.

It is worth noting that we implicitly assume in the above that the maximum degree of ionization is limited to that which can be expected thermally, since the ionization and recombination rates will shift to restore equilibrium in response to any perturbation. In practice, ionization proceeds also *via* nonthermal mechanisms such as electron impact or multiphoton absorption, which will result in a greater ionization fraction (and thus electron number density) than is otherwise possible. Electron–neutral inverse bremsstrahlung absorption has also not been considered here, although Bogaerts and Chen[31] have shown that this mechanism is normally the most significant, particularly close to the target surface. It is therefore highly probable that significant attenuation occurs also below the threshold irradiance as determined here.

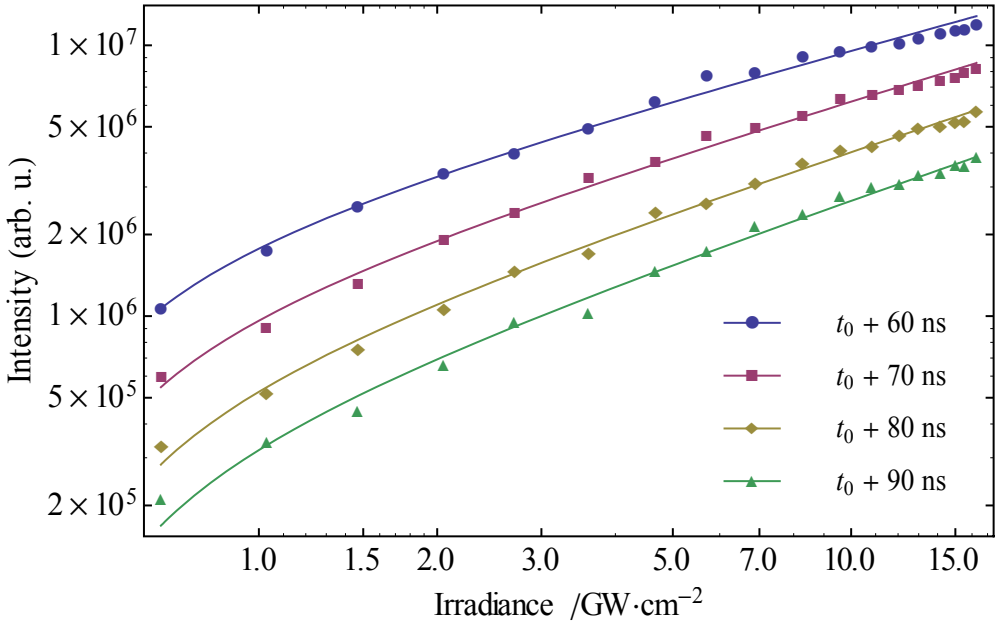

Figure 3.7: Variation with laser irradiance of the optical emission yield of $(Zn^{1+})^*$, as produced in the 355 nm ablation of Zn *in vacuo*. The overlaid curves are given by Equation 3.4 as fitted to the data.

Of course, the preceding argument cannot specifically account for the existence of a sharp threshold in optical emission yield, since it does not distinguish this situation from that of progressively increasing attenuation, as suggested by the alternative analysis presented in Figure 3.7. If the electron number density is not sufficient to effect the total attenuation of laser radiation through IBA, we may expect a continuing gradual increase of this quantity with irradiance, leading to approximately logarithmic scaling behaviour overall, which is equally consistent with the observations. Moreover, if phase explosion (for which substantial initial ionization of the ablation plume cannot be expected) is to account for the Zn^0 yield, plasma absorption is probably minimal and Zn^{1+} is then a minor constituent of the plasma whose yield will go as the square root of irradiance scaled by the (irradiance-dependent) ionization efficiency of the Zn vapour. Thus, while IBA probably influences plasma behaviour significantly, its status as a dominant effect is by no means conclusive based on the data examined so far.

Table 3.10: Fitted threshold, scale, and exponent (according to Equation 3.4) for each of the trends indicated in Figure 3.4, corresponding to the dependence of the optical emission yield of $(Zn^{1+})^*$ on the irradiance at 355 nm for the ablation of Zn *in vacuo*.

$I_{threshold}$	t_g	$0.68 \leq I \leq 16.28$ GW/cm^2	
		Scale A	Exponent n
0.454(21) GW/cm^2	t_0 + 60 ns	14.745(22)	0.587(11)
	t_0 + 70 ns	14.171(30)	0.650(15)
	t_0 + 80 ns	13.603(45)	0.711(23)
	t_0 + 90 ns	13.126(68)	0.740(35)

It is also interesting to note that the fitted power law exponents vary with time, increasing from ≈ 0.60 at t_0 + 60 ns to ≈ 0.75 at 90 ns after ablation. To account for this observation, we also consider the results obtained by fitting Equation 3.6. According to this model, the average exponent is 0.619(14), but moreover, the decay rate constant k is found as $4.81(12) \times 10^7$ s^{-1}. Although one might expect the experimental k-value to be similar to the Einstein A-coefficient for a given transition, this is apparently not the case, as k is here substantially smaller than the corresponding $A = 1.6 \times 10^8$ s^{-1},[19] and also appears to have essentially no dependence on the emission line for which it is calculated. Given that the observed fluorescence lifetime is far longer than would otherwise be predicted, we take the increase in the power law exponents as evidence that the upper states of some transitions continue to be populated even after laser excitation ends.[i] Furthermore, this evidently occurs in a way that is dependent on the amount of energy that was initially supplied: for example, by decay from more highly excited levels, or through predominantly thermally driven collisional processes such as electron impact excitation/ionization. Electron-ion recombination, on the other hand, is less likely to explain the observed behaviour since the velocity distributions (Figure 3.8) are clearly unimodal, whereas if some proportion of Zn^{1+} had previously existed as (e.g.) Zn^{2+}, some degree of bifurcation would be expected. It is not clear, in any case, that the effect of such recombination ought to scale with (rather than against) irradiance.

[i] In fact, the fitted values of k vary only by a factor of ≈ 2 regardless of the transition and species for which the analysis is performed. As the A-coefficients cannot reasonably be expected all to fall (by some improbable coincidence) within such a narrow range, this is suggestive of the applicability of the same behaviour to all species. However, it is obviously impossible to make a more conclusive statement to this effect given that rate constants are unknown for most of the observed transitions.

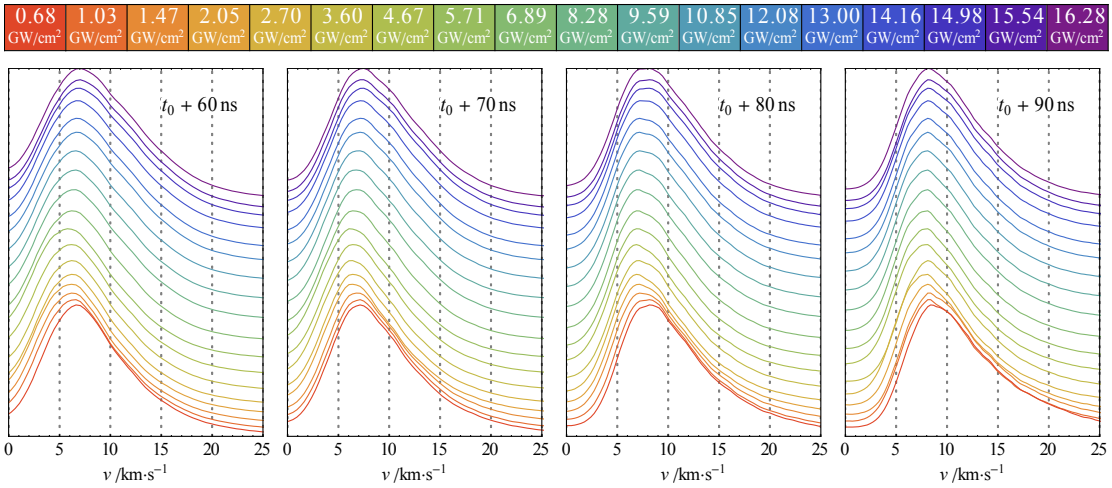

Figure 3.8: Spatial distribution of $(Zn^{1+})^*$ optical emission resulting from the ablation of Zn at 355 nm *in vacuo*.

The $(Zn^{1+})^*$ spatial profiles (or velocity distributions) are of similar form to those of $(Zn^0)^*$, except for the substantially greater modal velocity of ≈ 7–8 km/s (KE ≈ 20 eV)—which, however, remains essentially independent of irradiance. The latter observation is puzzling if, as proposed by Torrisi *et al.*,[32] ion acceleration is driven by charge separation resulting from the greater thermal velocity of electrons relative to ions (if both attain comparable temperatures). At higher irradiance, not only is more energy supplied to the plasma but also in a somewhat shorter time, so that a higher temperature may be expected to result and thus (according to this model) a stronger induced field. It seems likely, therefore, that space charge effects predominate, such that quasi-neutrality is maintained in the bulk of the plasma; polarization-induced acceleration is then possible, as suggested by Dreyfus,[33] only at the outer margins of the plume. Nonetheless, Zn^{1+} is manifestly not the highest charge state produced, and nor does this species possess the largest observed kinetic energy, so the applicability of such a mechanism is questionable, except perhaps early in the ablation process while the ionization fraction is low (and, in particular, before significant multiple ionization can occur).

The measured data strongly resemble the distributions obtained by Nedelea and Urbassek[34] using a one-dimensional particle-in-cell simulation, which it is interesting to note did not include any consideration of direct laser–plasma interaction, merely assuming a plasma consisting solely of electrons and singly charged ions in thermal equilibrium expanding adiabatically under the influence of its

own electric field. Due to the very close correspondence to our results, we assume that such a model is essentially correct in the case of Zn^{1+} and duplicate part of their Figure 1 as our Figure 3.9 (below) for reference. The symbol τ represents the timescale over which ions are ablated (at an assumed constant rate) from the target, $F(v)$ is the probability of finding an ion with velocity v, v/v_0 is the normalized ion velocity, $\varepsilon/\varepsilon_0$ is the normalized electric field, and $x/v_0\tau$ is normalized displacement from the "target" (origin).

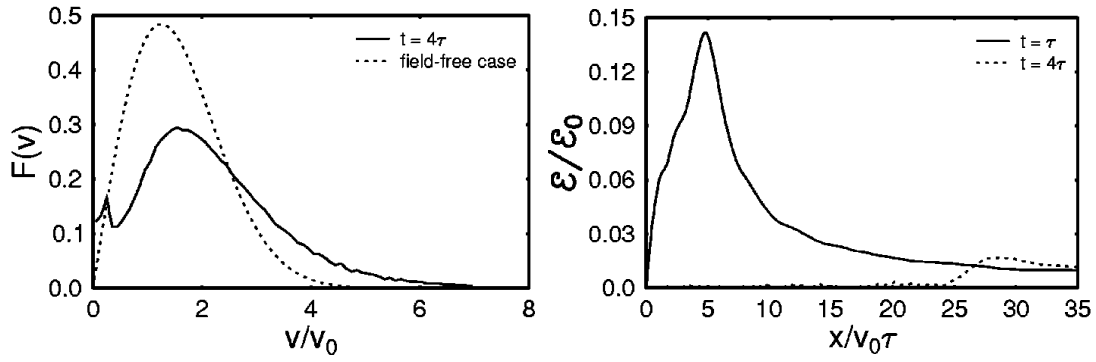

Figure 3.9: Part of Nedelea and Urbassek's Figure 1,[34] showing the normalized ion velocity and electric field a short time after "ablation" calculated using a particle-in-cell simulation. The correspondence between their simulated and our measured velocity distributions is striking, lending strong support to the idea that the behaviour of Zn^{1+} is well approximated under the assumptions of their model (see text).

$(Zn^{2+})^*$

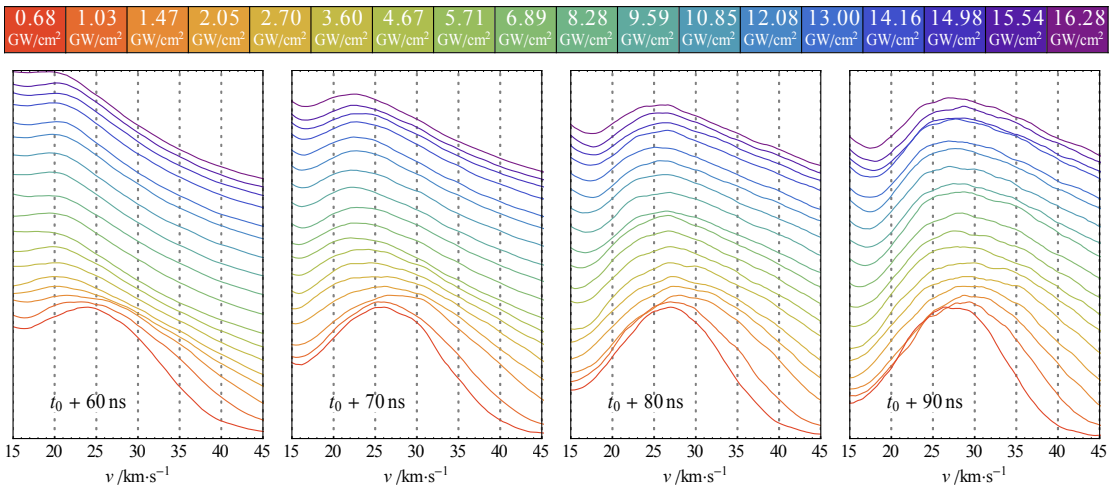

Figure 3.10: Spatial distribution of $(Zn^{2+})^*$ optical emission resulting from the 355 nm ablation of Zn *in vacuo*.

The spatial (or velocity) distribution of $(Zn^{2+})^*$ optical emission differs significantly from that of either $(Zn^{0})^*$ or $(Zn^{1+})^*$. Notably, there is a substantial change in the shape of the curves as irradiance is increased, with an initially roughly Gaussian distribution of velocities gaining a heavy fast tail above about 2–3 GW/cm^2. While the mean velocity clearly scales with irradiance as a result, the modal value does not, remaining roughly constant at ≈ 25 km/s (≈ 200 eV). It is notable, however, that at $t_g = t_0 + 60$ and 70 ns, velocity decreases slightly with increasing irradiance, which is probably indicative of competing formation mechanisms that impart different amounts of kinetic energy. Some acceleration is also apparent with time: at low irradiance, the increase in velocity is from ≈ 25 to ≈ 27 km/s between $t_0 + 60$ and $t_0 + 90$ ns, whereas a more pronounced increase from ≈ 20 to ≈ 27 km/s is evident for higher irradiance.

In comparison with the species already examined, $(Zn^{2+})^*$ possesses dramatically greater kinetic energy, with an essentially exponential increase of the most probable value from one charge state to the next; that is, ≈ 2 eV (Zn^{0}), to 20 (Zn^{1+}), to 200 eV (Zn^{2+}). Obviously, such strongly charge-dependent acceleration cannot be the result of interaction with a static electric field, but may instead be indicative of the behaviour described by Peurrung *et al.*[18], except with the moving space charge region formed in this case not by photoelectron emission but rather due to escaping hot electrons per Torrisi *et al.* or Dreyfus. Indeed, the simulated electric field distribution given by Nedelea and Urbassek and shown in Figure 3.9 demonstrates that such a region exists for quite some time during expansion, and persists at the front edge of the plume even after the majority of the plasma becomes quasi-neutral. Moreover, Peurrung *et al.* have stressed the importance of the relative positions of the space charge region and the launched ion in determining the degree of acceleration, since both must move together for an extended period in order for maximum energy transfer to occur. By this interpretation, the acceleration imparted to Zn^{1+} ions is inherently limited due to their situation for the most part far behind the charge separation front, which exists of necessity only in the fast tail of the distribution. Zn^{2+}, however, may freely be produced by multi-photon or electron impact ionization of Zn^{1+} that is *already* in the hot fraction at the front edge of the plasma. The accelerating force acting on these ions thereby immediately doubles, allowing them to move further into the space charge region, where they are subject to additional acceleration until they are either

retarded by their own induced field or cooled sufficiently by adiabatic expansion that they recapture an electron.

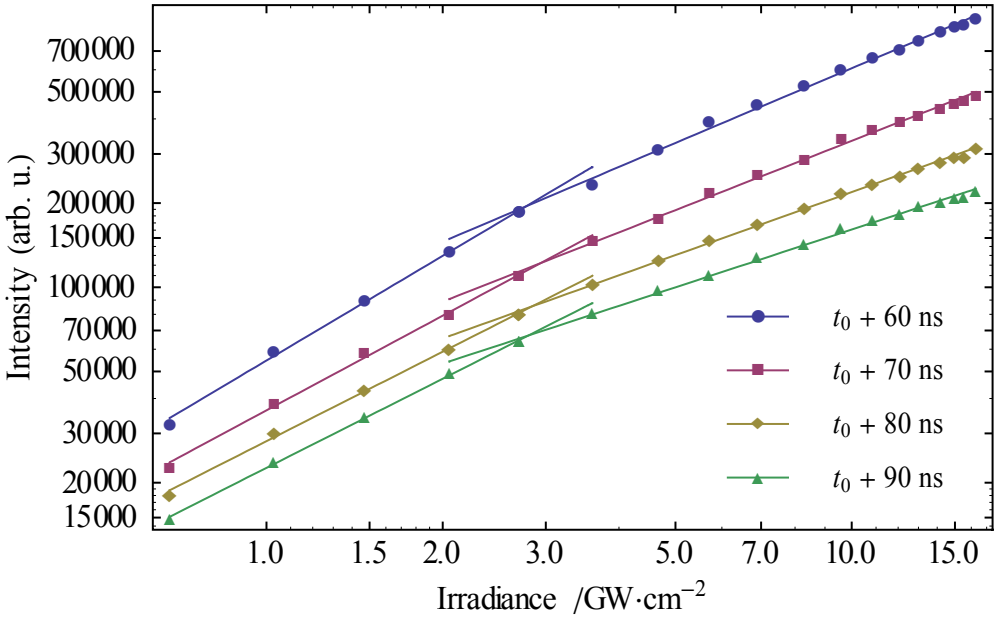

Figure 3.11: Variation with laser irradiance of the optical emission yield of (Zn^{2+})*, as produced in the 355 nm ablation of Zn *in vacuo*. The overlaid line segments correspond to power laws per Equation 3.2.

Due to the apparently rather different formation and acceleration mechanisms to which Zn^{2+} is subject, we must exercise some additional care in interpreting the optical emission yields. In particular, it is no longer clear that the trends observed in the high and low irradiance regimes are directly comparable with each other, since different processes are likely to dominate in each case. As suggested by the spatial profiles, the threshold lies at around 3 GW/cm^2, and here probably represents the point at which a mechanism that operates at low irradiance and imparts high kinetic energy is dominated by one for which the degree of acceleration is less significant.

Table 3.11: Fitted scale and exponent (according to Equation 3.2) for each of the trends indicated in Figure 3.11, corresponding to the dependence of the optical emission yield of $(Zn^{2+})^*$ on the irradiance at 355 nm for the ablation of Zn *in vacuo*.

t_g	$0.68 \leq I \leq 2.70$ GW/cm^2		$2.70 \leq I \leq 16.28$ GW/cm^2	
	Scale A	Exponent n	Scale A	Exponent n
t_0 + 60 ns	10.910(21)	1.243(28)	11.273(31)	0.888(14)
t_0 + 70 ns	10.499(23)	1.124(32)	10.824(26)	0.823(12)
t_0 + 80 ns	10.246(17)	1.062(25)	10.572(15)	0.749(7)
t_0 + 90 ns	10.026(11)	1.058(16)	10.409(19)	0.686(9)

Interestingly, the power law exponents at low irradiance are now slightly in excess of unity, which is suggestive of saturated multiphoton ionization, where in this case saturation may be due to the limiting availability of the source species (most probably an excited state of Zn^{1+}). Above the threshold, the exponents are sub-unity, yet still greater than the value of ½ expected if some constant fraction of Zn^0 becomes doubly ionized. We thus require a process for which the ionization efficiency increases with irradiance, for which electron impact is a suitable candidate due to the expected effect of avalanche ionization and the strong dependence of the absorption depth on the initial electron density. Furthermore, the (shifted) quasi-Maxwellian form of the velocity distributions at high irradiance is suggestive of the formation of Zn^{2+} preferentially in the hot leading edge of the existing plasma, which is consistent with such a hypothesis.

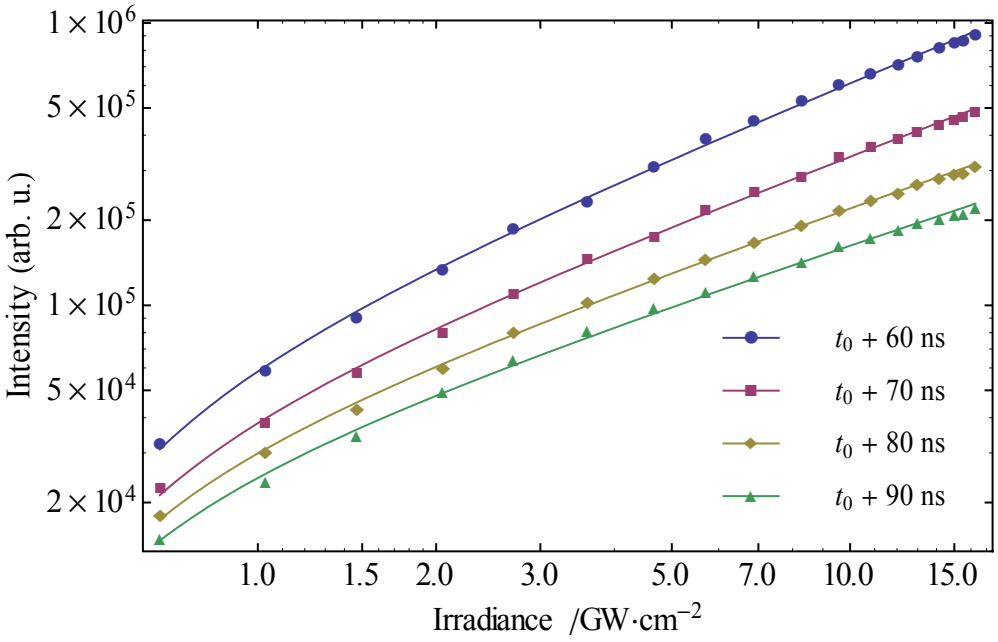

Figure 3.12: Variation with laser irradiance of the optical emission yield of $(Zn^{2+})^*$, as produced in the 355 nm ablation of Zn *in vacuo*. The overlaid curves are given by Equation 3.4 as fitted to the data.

The appropriateness of the fit to Equation 3.4 (Figure 3.12/Table 3.12) is somewhat questionable, since evidently a single power law relationship cannot meaningfully represent two competing processes; nonetheless, the fit is empirically very good and permits the approximate determination of the formation threshold for $(Zn^{2+})^*$ as 0.399(14) GW/cm^2. This value is smaller than that obtained in the previous subsection, although it is not immediately clear whether the formerly determined values are especially accurate since the fit to Equation 3.4 for the $(Zn^{1+})^*$ optical emission yields is rather poorer than for the current dataset. In any case, it is probably reasonable to conclude that the thresholds for both species are roughly comparable and similar to that of $(Zn^0)^*$, since the quantity of material ablated at low irradiance is determined largely according to whether or not the Zn target reaches the critical temperature and the volume throughout which this degree of heating is achieved.

Table 3.12: Fitted threshold, scale, and exponent (according to Equation 3.4) for each of the trends indicated in Figure 3.12, corresponding to the dependence of the optical emission yield of $(Zn^{2+})^*$ on the irradiance at 355 nm for the ablation of Zn *in vacuo*.

$I_{threshold}$	t_g	$0.68 \leq I \leq 16.28$ GW/cm^2	
		Scale A	Exponent n
0.399(14) GW/cm^2	t_0 + 60 ns	11.405(16)	0.848(7)
	t_0 + 70 ns	10.950(20)	0.784(10)
	t_0 + 80 ns	10.672(24)	0.721(12)
	t_0 + 90 ns	10.453(28)	0.683(15)

$(Zn^{3+})^*$

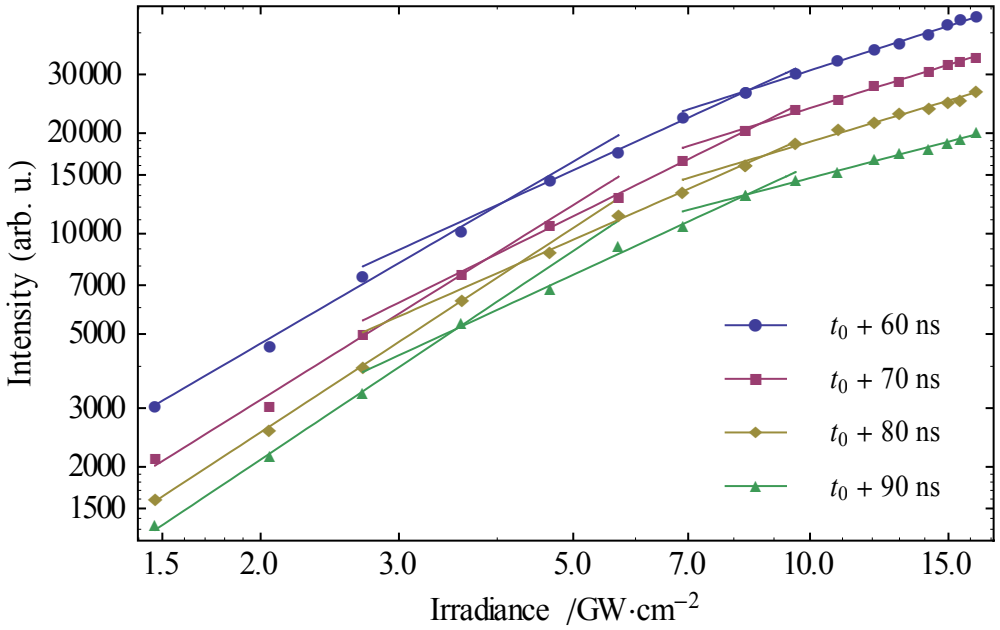

Figure 3.13: Variation of the optical emission yield of $(Zn^{3+})^*$ with laser irradiance, as recorded subsequent to the ablation of Zn *in vacuo* at 355 nm. The overlaid line segments correspond to power laws per Equation 3.2.

Zn^{3+} is the first species considered for which it is not possible to obtain a good representation of the scaling of optical emission yield with irradiance by using only two power laws; rather, three such functions are the minimum required to model the data. As it is unlikely that three different processes are responsible for the formation of $(Zn^{3+})^*$ and each dominates over the others only in a narrow irradiance range, we consider the results presented in Figure 3.13 and Table 3.13 as essentially empirical in nature. Since the spatial profiles (Figure 3.14) reveal (in contrast to the situation for the other species) an obviously significant formation threshold, the power law exponents in the low irradiance regime must be considered especially doubtful. There

is, however, reasonable evidence of saturation at moderate irradiance, with a threshold at 8.5(3) GW/cm^2 signifying the point above which essentially linear scaling no longer holds.

Table 3.13: Fitted scale and exponent (according to Equation 3.2) for each of the trends indicated in Figure 3.13, corresponding to the dependence of the optical emission yield of (Zn^{3+})* on the irradiance at 355 nm for the ablation of Zn *in vacuo*.

t_g	$1.47 \leq I \leq 3.60$ GW/cm^2		$4.67 \leq I \leq 8.28$ GW/cm^2		$8.28 \leq I \leq 16.28$ GW/cm^2	
	A	n	A	n	A	n
t_0 + 60 ns	7.501(103)	1.371(102)	7.915(82)	1.077(44)	8.594(40)	0.756(16)
t_0 + 70 ns	7.045(82)	1.468(80)	7.452(99)	1.167(53)	8.380(58)	0.737(23)
t_0 + 80 ns	6.771(28)	1.540(27)	7.500(103)	1.037(55)	8.228(80)	0.702(32)
t_0 + 90 ns	6.561(44)	1.572(42)	7.175(177)	1.088(95)	8.170(47)	0.618(19)

The (Zn^{3+})* velocity distributions are quite distinct from those already examined, showing a substantial increase in modal velocity with irradiance: ≈ 42 km/s (600 eV) at the formation threshold, rising to 55 km/s (≈ 1 keV) at 16.28 GW/cm^2. While not representing a further exponential increase of kinetic energy relative to Zn^{2+}, this value is still surprisingly large in view of the fact that the present experiments represent very mild conditions (long pulses, low pulse energy, and loose focusing) in comparison to others conceived with the explicit intention of producing high-energy ions.

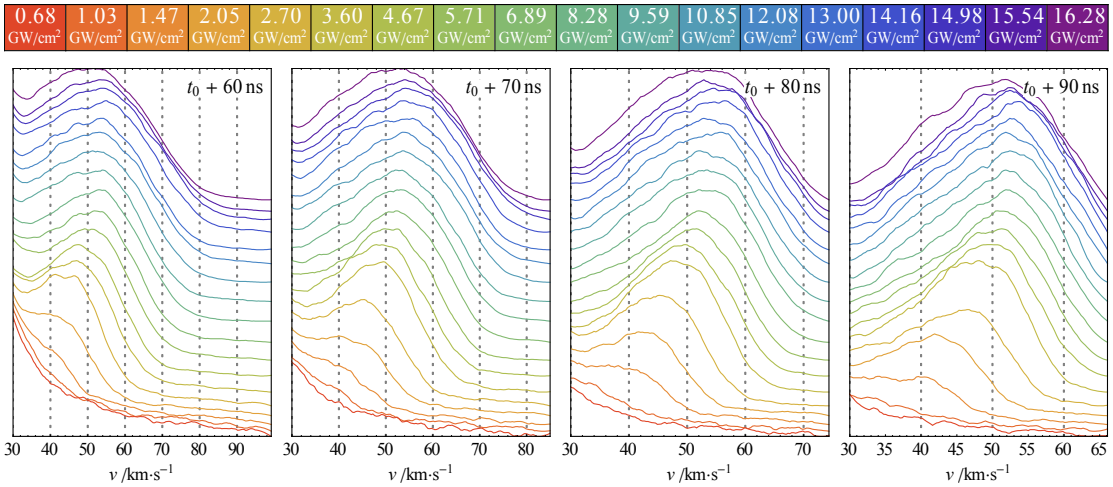

Figure 3.14: Spatial (velocity) distribution of (Zn^{3+})* optical emission resulting from the ablation of Zn at 355 nm *in vacuo*.

Furthermore, Zn^{3+} exhibits a subthermal KE distribution, and in this respect is unlike even Zn^{2+}. There is, however, considerable similarity between the Zn^{2+} spatial profiles *at low irradiance* and those of the higher charge state, suggesting that the two species may be formed in predominantly the same way until a second source term becomes dominant for Zn^{2+} at high irradiance. Considering the 39.7 eV third ionization potential of zinc, and the fact that the emitting state of Zn^{3+} almost certainly also possesses a comparable (or greater) amount of excess energy in the form of electronic excitation, it seems reasonable to assume that thermal excitation is not sufficient to generate significant observable Zn^{3+} even at the highest irradiance employed here. The observed upper state of Zn^{2+} (with ≈ 35 eV of electronic excitation), on the other hand, could conceivably be thermally populated due to the heating of the front edge of the plasma that would result from inverse bremsstrahlung absorption of on average 10 photons at 355 nm. If this interpretation is correct, both species are produced by multiphoton ionization (or another non-thermal process with similar irradiance scaling) and subject to the space charge–driven acceleration described in the previous section, except that this becomes an increasingly minor channel for Zn^{2+} as irradiance is increased.

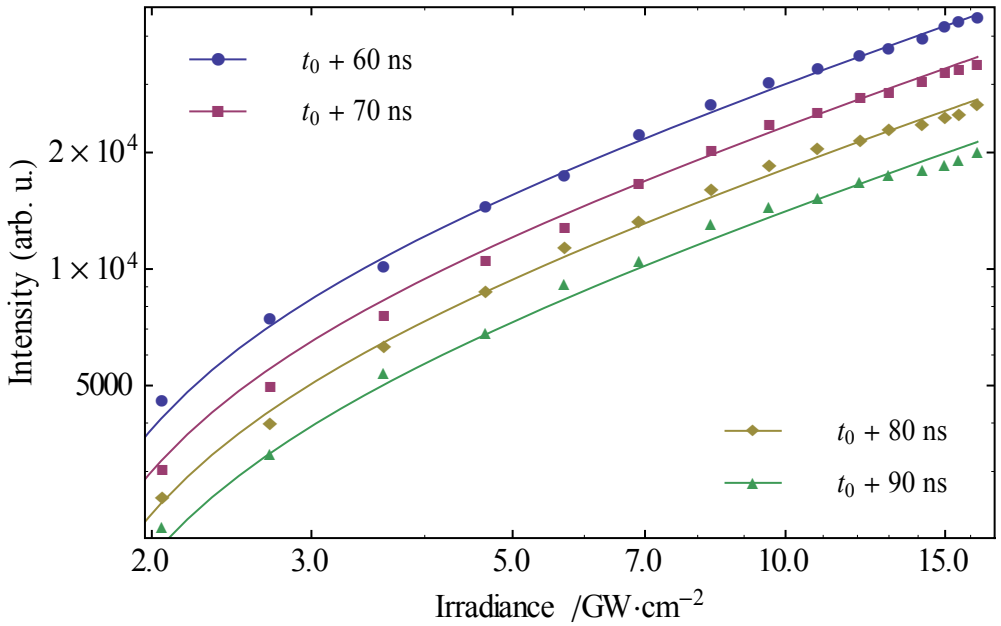

Figure 3.15: Variation with laser irradiance of the optical emission yield of $(Zn^{3+})^*$, as produced in the 355 nm ablation of Zn *in vacuo*. The overlaid curves are given by Equation 3.6 as fitted to the data.

With reference to the fits obtained using Equation 3.6 (Figure 3.15), we find that the $(Zn^{3+})^*$ formation threshold is equal to 1.45(6) GW/cm^2, which is clearly much greater than the value of ≈ 0.4 GW/cm^2 obtained for each of the species examined previously. Given the above-unity power law exponents at low irradiance for both Zn^{2+} and Zn^{3+}, this is supportive of multi-photon ionization, since higher-order absorption must occur with far lower probability for any given irradiance. The question naturally arises as to how probable the required 10- or 20-photon absorption can really be, given the moderate laser intensity employed in the present work. This point has been addressed by Varró and Ehlotzky,[35] who found that 34-photon absorption by laser-ablated Au atoms is possible, even for irradiance as low as 0.12 GW/cm^2, due to the formation of a strong dipole layer at the metal surface. However, it is worth pointing out some significant differences between the present situation and that examined in the prior work, which assumed 1 064 nm, 8 ps laser pulses, and the absence of plasma during the laser–target interaction. On the one hand, the frequency of the radiation employed here is greater, plasma is certainly more readily polarizable than metal, and radiation may penetrate it more deeply; on the other, the formation of a space charge layer most likely substantially reduces the effective dipole potential. Since the analysis given by Varró and Ehlotzky relies on the numerical solution of large systems of equations, it is difficult to predict the outcome of their model as applied to the nanosecond irradiation of Zn; we thus conclude only that mechanisms are known which, in principle, could permit high-order multiphoton ionization for even lower irradiance than used here.

The values of the other parameters in Equation 3.6 are found as $k = 2.525(55) \times 10^7$ s^{-1} and $n = 0.750(16)$, which may offer additional insight into the mechanism according to which Zn^{3+} is produced. If we assume that the Einstein A-coefficient for the observed transitions of $(Zn^{3+})^*$ is larger than k, as it is for those of $(Zn^{1+})^*$, then the status of multiphoton ionization as the principal formation mechanism is called into question, since clearly this may only occur during the laser pulse and not 60–90 ns afterwards. The most likely possibility apart from multiphoton ionization appears to be continuing electron impact ionization/excitation: the high temperature resulting from inverse bremsstrahlung absorption by already hot electrons in the space charge region of the nascent plasma may persist during the initial quasi-free expansion, with thermal energy being dissipated into the trailing ions over an

extended period. If this account is accurate, it is also easier to interpret the power law exponent, as a value of at least unity would be expected for photoionization, but this is clearly not achieved in the present case. However, multiphoton ionization may still be an important contributor to the initial free electron density, as suggested by Dreyfus,[33] even if it is not directly responsible for the bulk of the Zn^{3+} yield. As this will not necessarily be apparent in the results presented so far, we refrain from commenting further on the status of this process until additional experimental scenarios have been examined.

3.3.2 ZINC UNDER 50 MTORR O_2

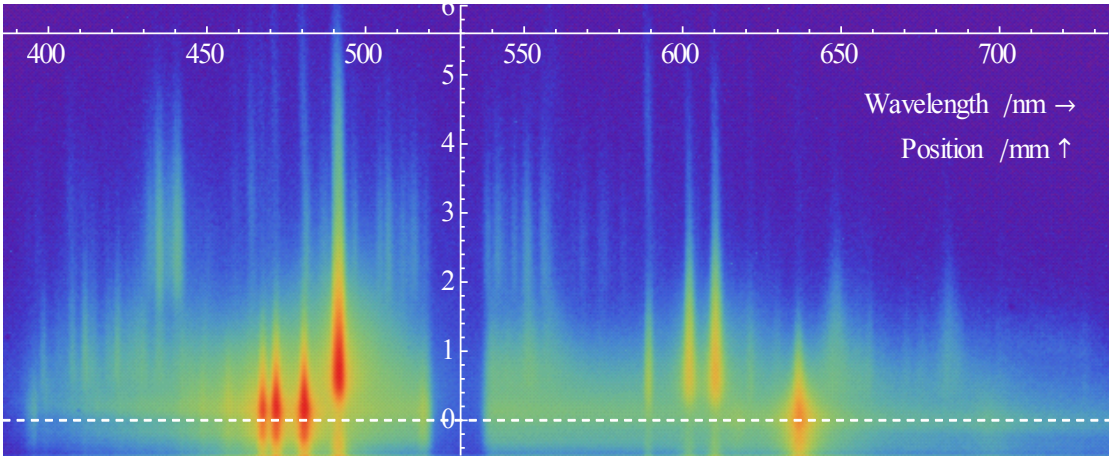

Figure 3.16: Spatiospectral image taken at $t_g = t_0 + 80$ ns subsequent to the 355 nm ablation of Zn under oxygen with $p(O_2) = 50$ mTorr and $I = 7.22$ GW/cm^2.

In comparison with Figure 3.1, Figure 3.16 appears broadly similar, but with two important differences being apparent. The first of these is that emission due to $(Zn^{3+})^*$, which had appeared at ≈ 462 nm and in the distance range 3–6 mm *in vacuo*, is now essentially absent in the presence of oxygen. Furthermore, certain lines associated with the lower charge states extend to greater distance than was previously the case, as well as exhibiting secondary intensity maxima approximately coincident with the expected spatial location of Zn^{3+}. It is interesting to note that this effect is especially pronounced for the $(Zn^{1+})^*$ line at 589.433 nm, which is unusual in originating from a state having an $[Ar]3d^9$ ($^2D_{3/2}$) core; indeed, this is the only (known) two-electron transition observed with significant intensity in the present work.[j] Given that the ground state of Zn^{3+} is $[Ar]3d^9$ ($^2D_{5/2}$)[k], and since all of the

[j] The related $[Ar]3d^{10}4p\ ^2P_{3/2,u} \leftarrow [Ar]3d^94s^2\ ^2D_{3/2,g}$ transition at 621.461 nm appears to share the same spatial profile as the 589.433 nm line, but is barely discernible from the image.

$(Zn^{2+})^*$ lines (cf. Table 3.3) also involve this core configuration, it appears plausible that the enhanced 589.433 nm emission may be attributable to electron-ion recombination of either $(Zn^{2+})^*/(Zn^{3+})^*$ or ground-state Zn^{3+}. Charge transfer reactions between these species and Zn^0 might also occur; according to Riseberg and Schearer,[36] a similar mechanism (Penning ionization of Zn^0 by metastable He atoms), is responsible for populating the upper state of the 589.433 nm transition in the HeZn laser. This process must be reasonably efficient since worthwhile laser action can be obtained on this line, the $[Ar]3d^{10}4p\ ^2P_{1/2} \leftarrow [Ar]3d^9 4s^2\ ^2D_{3/2}$ transition of $(Zn^{1+})^*$ being analogous to that of $(Cd^{1+})^*$, i.e. $[Kr]4d^{10}5p\ ^2P_{1/2} \leftarrow [Kr]4d^9 5s^2\ ^2D_{3/2}$, by means of which emission at 325.033 nm is produced in the common HeCd laser.[37] It is, however, open to question whether a meaningful quantity of Zn^0 is likely to be spatially coincident with the higher charge states in order for this to occur.

$(Zn^0)^*$

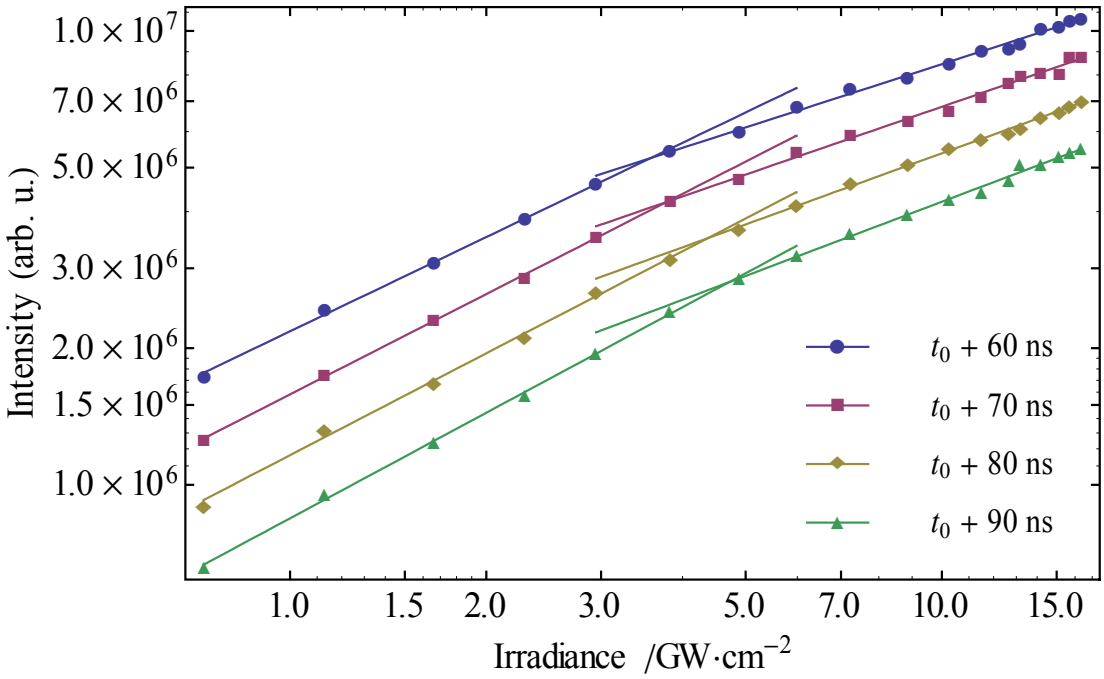

Figure 3.17: Variation with laser irradiance of the optical emission yield of $(Zn^0)^*$, as produced in the 355 nm ablation of Zn under oxygen with $p(O_2) = 50$ mTorr. The overlaid line segments correspond to power laws per Equation 3.2.

Perhaps unsurprisingly, the introduction of a low background pressure of oxygen appears to have little effect on the optical emission yield of $(Zn^0)^*$, with the findings

[k] The spin-orbit splitting between the ^2D terms amounts to 2 759.1 cm^{-1}, or 0.342 eV.[6]

in this case being negligibly different from those reported in §3.3.1. The irradiance threshold delineating the two applicable regimes of Equation 3.2 is presently found as 4.1(7) GW/cm^2, with the power law exponents being 0.74(4) below and 0.51(4) above this value.

Table 3.14: Fitted scale and exponent (according to Equation 3.2) for each of the trends indicated in Figure 3.17, corresponding to the dependence of the optical emission yield of $(Zn^0)^*$ on irradiance for the ablation of Zn at 355 nm under $p(O_2)$ = 50 mTorr.

t_g	$0.74 \leq I \leq 3.83$ GW/cm^2		$4.88 \leq I \leq 16.37$ GW/cm^2	
	Scale A	Exponent n	Scale A	Exponent n
t_0 + 60 ns	14.595(10)	0.690(14)	14.883(29)	0.463(13)
t_0 + 70 ns	14.275(5)	0.734(7)	14.590(35)	0.496(15)
t_0 + 80 ns	13.966(17)	0.746(23)	14.298(21)	0.521(9)
t_0 + 90 ns	13.646(12)	0.772(15)	14.002(26)	0.543(11)

While the statistical indistinguishability of the quantities presented in Table 3.14 from those obtained in the absence of oxygen (Table 3.7, page 55) demonstrates the repeatability of the experimental procedure, it is clearly uninformative as to the role of the backing gas in influencing ablation dynamics. We therefore do not comment further on these results.

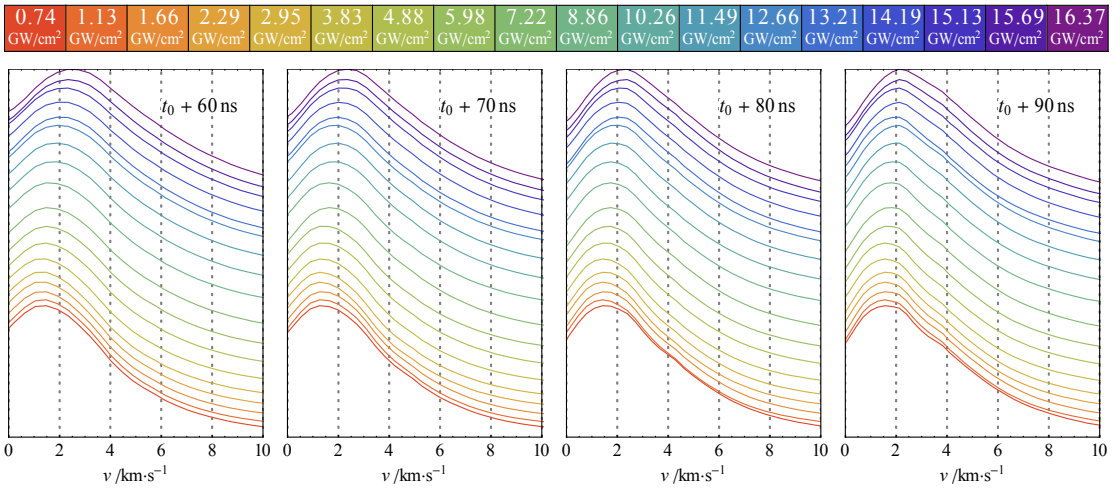

Figure 3.18: Spatial distribution of $(Zn^0)^*$ optical emission resulting from the ablation of Zn at 355 nm under $p(O_2)$ = 50 mTorr.

The spatial profiles (Figure 3.18) similarly do not reveal any quantifiable differences, which, if (as discussed previously) we assume a thermal distribution of velocities for the neutral species, is consistent with the predictions of Chen *et al*. of very limited

dependence of the plasma temperature on background gas pressure for the ablation of Cu under He.[38, 39]

Table 3.15: Fitted threshold, scale, and exponent (according to Equation 3.4) for each of the trends indicated in Figure 3.19, corresponding to the dependence of the optical emission yield of $(Zn^0)^*$ on irradiance for Zn under $p(O_2)$ = 50 mTorr ablated at 355 nm.

$I_{threshold}$	t_g	$0.74 \leq I \leq 16.37$ GW/cm^2	
		Scale A	Exponent n
0.360(19) GW/cm^2	t_0 + 60 ns	14.840(14)	0.494(7)
	t_0 + 70 ns	14.537(15)	0.531(9)
	t_0 + 80 ns	14.234(18)	0.557(10)
	t_0 + 90 ns	13.923(21)	0.584(12)

The formation threshold of $(Zn^0)^*$ also does not vary significantly under oxygen, with the value of 0.36(2) GW/cm^2 (Figure 3.19/Table 3.15) being very close to that of 0.39(2) GW/cm^2, as obtained *in vacuo*. Since these values differ mutually by only 1.5 standard deviations, and given the lack of evidence in the other fitted parameters for any discrepancy, we consider them equal for present purposes.

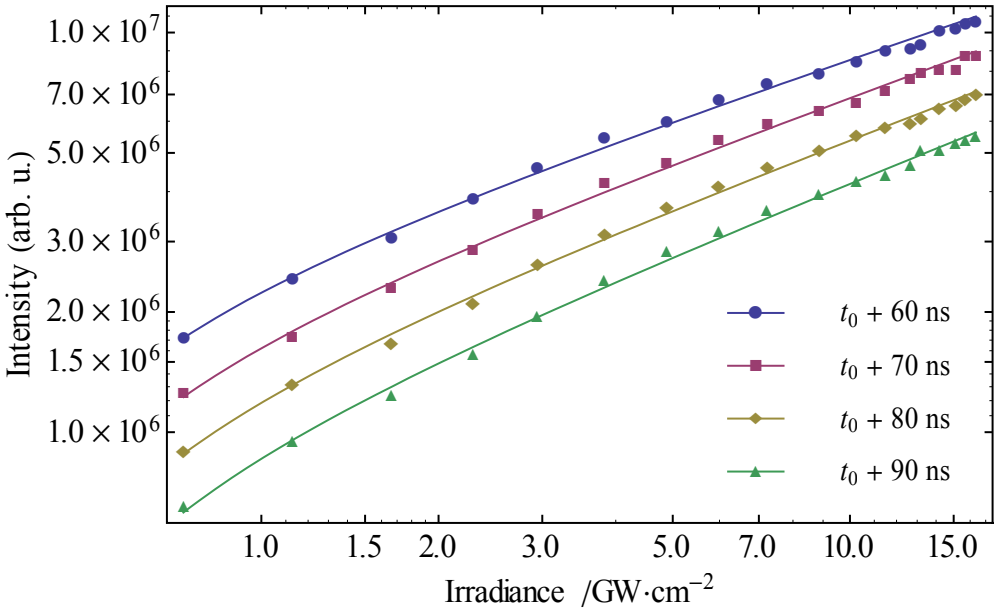

Figure 3.19: Variation with laser irradiance of the optical emission yield of $(Zn^0)^*$, as produced in the 355 nm ablation of Zn under oxygen with $p(O_2)$ = 50 mTorr. The overlaid curves are given by Equation 3.4 as fitted to the data.

$(Zn^{1+})^*$

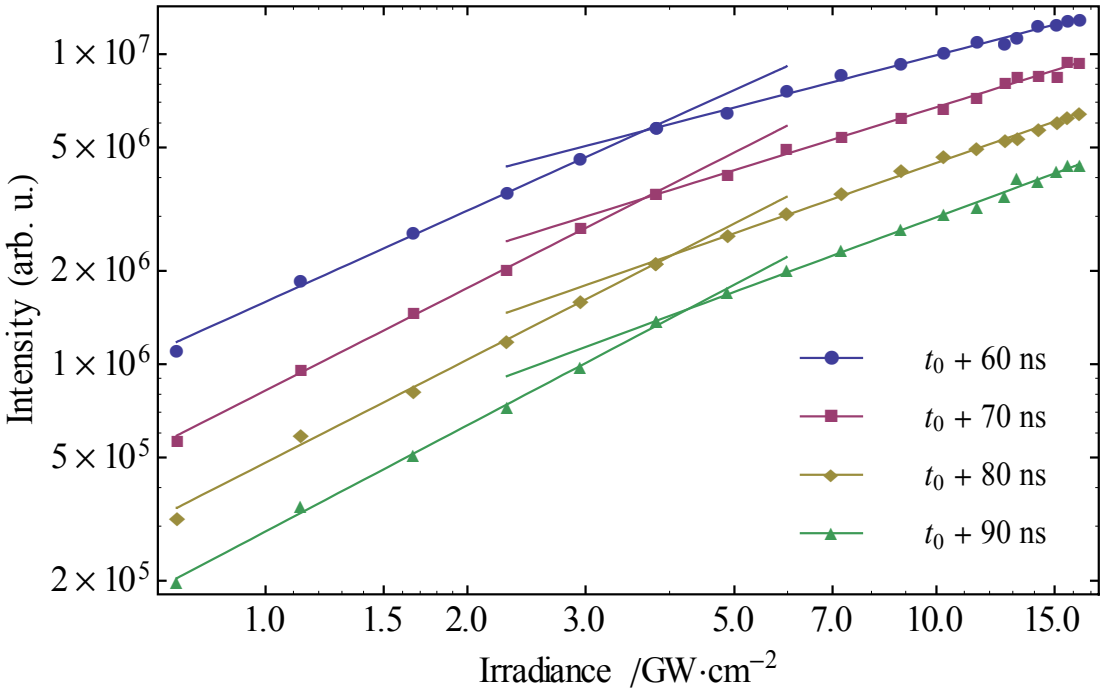

Figure 3.20: Variation with laser irradiance of the optical emission yield of $(Zn^{1+})^*$, as produced in the 355 nm ablation of Zn under oxygen with $p(O_2) = 50$ mTorr. The overlaid line segments correspond to power laws per Equation 3.2.

The results obtained for $(Zn^{1+})^*$ under oxygen similarly do not vary greatly with respect to the measurements made without ambient gas: the mean lower exponent, threshold irradiance, and upper exponent take values of 1.1(4), 3.9(4) GW/cm^2, and 0.7(1), respectively.

Table 3.16: Fitted scale and exponent (according to Equation 3.2) for each of the trends indicated in Figure 3.17, corresponding to the dependence of the optical emission yield of $(Zn^{1+})^*$ on irradiance for the ablation of Zn at 355 nm under $p(O_2) = 50$ mTorr.

t_g	$0.74 \leq I \leq 3.83$ GW/cm^2		$3.83 \leq I \leq 16.37$ GW/cm^2	
	Scale A	Exponent n	Scale A	Exponent n
t_0 + 60 ns	14.279(24)	0.977(29)	14.821(25)	0.560(11)
t_0 + 70 ns	13.621(15)	1.099(17)	14.171(32)	0.675(14)
t_0 + 80 ns	13.085(33)	1.104(37)	13.573(25)	0.755(11)
t_0 + 90 ns	12.573(25)	1.139(28)	13.063(33)	0.801(14)

The values of the exponents are consistently slightly larger than those found for ablation *in vacuo*, indicating that greater energy input is required in order to obtain a proportional increase in the optical emission yield. This is somewhat surprising given

that the collision frequency in oxygen at 50 mTorr is only 5.9×10^5 s^{-1}, so that there is very little scope for collisional deactivation, with the background gas remaining essentially static over the timescale of the experiment. This being the case, however, the oxygen initially occupying the volume into which the ablation plasma expands is surely subject to significant compression; and as the collision frequency is probably much greater at the interface between hot Zn plasma and the surrounding medium, the rate of either collisional or reactive quenching is likely to be correspondingly larger in this region. We may therefore anticipate a preferential diminution of optical emission intensity at the leading edge of the plume.

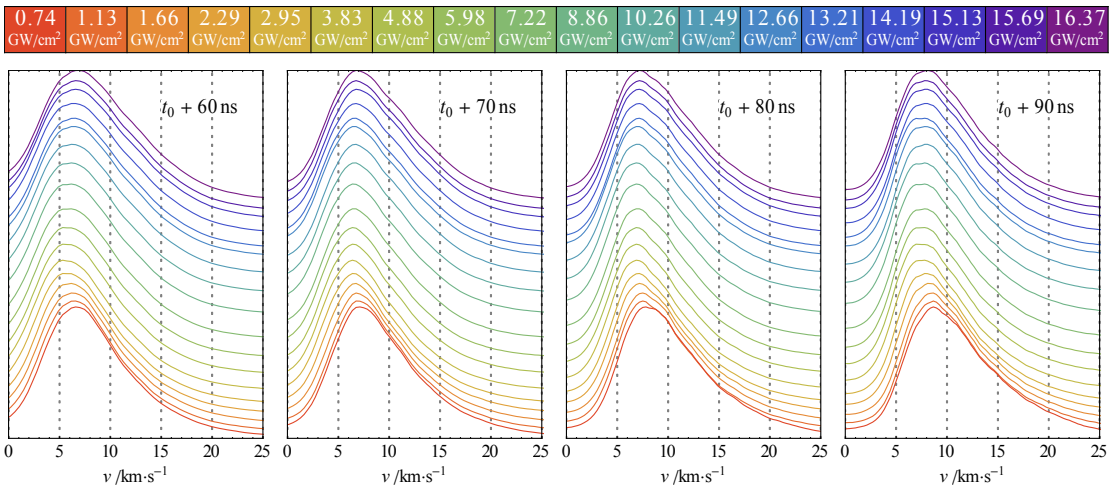

Figure 3.21: Spatial (velocity) distribution of $(Zn^{1+})^*$ optical emission resulting from the 355 nm ablation of Zn under $p(O_2)$ = 50 mTorr.

Nevertheless, the spatial distributions (Figure 3.21) are suggestive of indistinguishable dynamics for Zn^{1+} regardless of the presence of oxygen, contrary to what might be expected. This suggests that either the Zn plasma does not displace the ambient medium (instead intermixing with it), or that the processes that lead to quenching occur early in the expansion (i.e., at $t \ll t_0 + 60$ ns) while Zn^{1+} ions possessing different velocities have yet to achieve any significant degree of spatial separation. The latter possibility appears plausible in view of the observed forward-biased expansion, as shown in Figure 3.22, which, according to Chen *et al.*,[40] is attributable to a combination of two thermohydrodynamic effects that occur primarily while the laser pulse persists. These are, respectively, the continuous addition of material to the plasma by vaporization from the target surface, and an effective translational cooling (and therefore, by conservation of momentum, increased flow

velocity) resulting from the partitioning of available thermal energy into autoionization at the expansion front, the latter being of reduced significance in the presence of background gas.[1] Although only ionization was considered as a thermal sink by the previous authors, their argument does not rely on the formation or existence of charged particles and similar reasoning should apply to electronic excitation of Zn^0 below the ionization potential, and indeed to the formation of electronically excited Zn^{1+}. (We note explicitly that this process is not related to the space-charge-mediated acceleration that we suggest is responsible for imparting very high kinetic energies, and rather different spatial distributions, to the Zn^{2+} and Zn^{3+} ions.) We would therefore expect the Zn^{1+} velocity distributions to be narrower under $p(O_2) = 50$ mTorr than *in vacuo*, with a smaller maximum velocity having been achieved in the nascent plume. This is not observed, however; the spatial profiles appear almost identical, so although the mechanism is appealing (in that it explains the forward-biased expansion and is able to account for the greater velocity of Zn^{1+} than Zn^0 without requiring drastically different spatial distributions), there must be some doubt as to whether it really applies in this case.

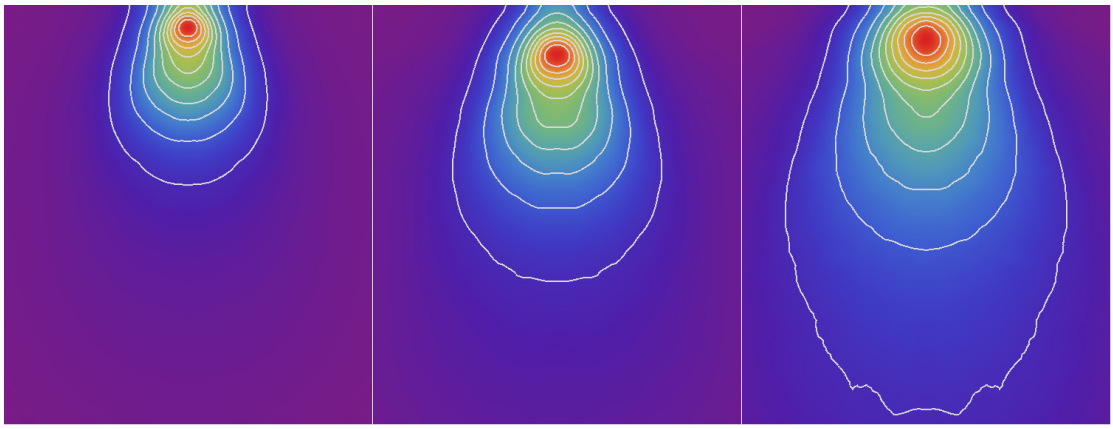

(a) t_0 + 100 ns (b) t_0 + 125 ns (c) t_0 + 150 ns

Figure 3.22: Spectrally unresolved images of the Zn plasma at $t = t_0 + \{100, 125, 150\}$ ns after ablation *in vacuo*, demonstrating forward-biased expansion. The target is located at the top of the images, and contour lines are drawn to aid in the recognition of the plasma plume geometry.

[1] Similar phenomena are noted by the (unrelated) Chen *et al*. cited previously,[39] which they ascribe instead to enhanced inverse bremsstrahlung absorption. Regardless of the assumed mechanism, the conclusion is the same: in the presence of ambient gas, ionization by the leading shock wave alters the distribution of thermal energy within the plume so that the central part of the plasma achieves a relatively higher temperature than the expansion front, while the opposite situation applies *in vacuo*.

Another possibility is that hot electrons (as the species with the lowest mass, and therefore the highest velocity at a given temperature, hence the greatest spatial extent) are subject to capture by the surrounding oxygen, which possesses a relatively high electron affinity: 0.448(6) eV for the O_2 molecule,[41] or 1.439157(4) eV for O atoms.[42] Having undergone such capture, the mobility of the negative species will be decreased sharply, which may alter the electric field distribution in the expanding plasma, especially if zinc and oxygen ions mutually react to form neutral ZnO molecules instead of contributing to a space charge layer. Subject to a reduced accelerating field, $(Zn^{1+})^*$ may remain for longer in the hot centre of the plume, and therefore be subject to collisional quenching not by O_2 but rather, as an indirect effect of the presence of the ambient gas, by Zn^0. However, this too should be apparent in the $(Zn^{1+})^*$ spatial distributions, which show no indication of an altered plasma self-field, remaining very similar to the predictions of Nedelea and Urbassek[34] based on a model that does not include electron capture.

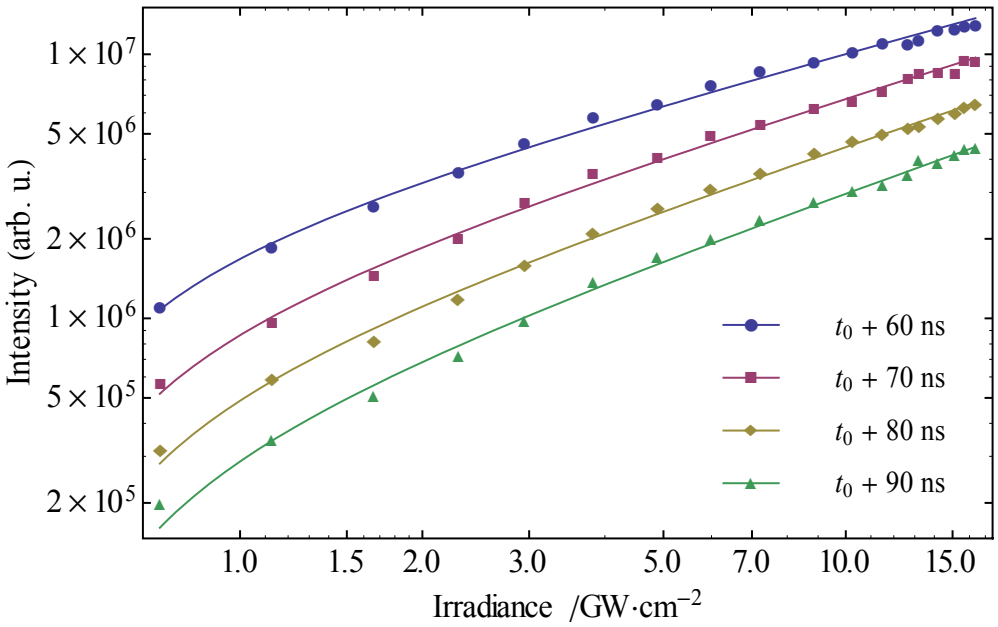

Figure 3.23: Variation with laser irradiance of the optical emission yield of $(Zn^{1+})^*$, as produced in the ablation of Zn at 355 nm under $p(O_2)$ = 50 mTorr. The overlaid curves are given by Equation 3.4 as fitted to the data.

The results presented in Figure 3.23 and Table 3.17 are again indicative of slightly larger power law exponents under oxygen, and the appearance threshold of 0.49(2) GW/cm^2 is somewhat greater than the figure of 0.45(2) GW/cm^2 obtained *in*

vacuo. The extra degree of freedom introduced *via* this threshold also renders the scale factor A somewhat more meaningful than in Equation 3.2, and we observe that the A-values according to Equation 3.4 are in fact equal to those determined previously. A more precise interpretation of the larger exponent values thus arises versus what has been discussed above: although the optical emission yield is reduced *at low irradiance* in oxygen, the average yield is the same, so that it must also be *increased* at high irradiance. This is clearly apparent when Figure 3.7 and Figure 3.23 are overlaid (not shown). Furthermore, Equation 3.6 provides $k = 4.74(13) \times 10^7\ \mathrm{s}^{-1}$ versus $k = 4.81(12) \times 10^7\ \mathrm{s}^{-1}$ previously, i.e. the addition of oxygen has no statistically significant effect on the rate at which optical emission decays. Unfortunately, these additional results provide no clarification of the role of the background gas; indeed, its influence appears more subtle than was initially recognized. The real reason for the altered scaling of $(Zn^{1+})^*$ optical emission yield for ablation under oxygen thus remains rather unclear at present.

Table 3.17: Fitted threshold, scale, and exponent (according to Equation 3.4) for each of the trends indicated in Figure 3.23, corresponding to the dependence of the optical emission yield of $(Zn^{1+})^*$ on the irradiance at 355 nm for the ablation of Zn under $p(O_2)$ = 50 mTorr.

$I_{\mathrm{threshold}}$	t_g	$0.74 \le I \le 16.37$ GW/cm^2	
		Scale A	Exponent n
0.490(20) GW/cm^2	t_0 + 60 ns	14.745(20)	0.610(10)
	t_0 + 70 ns	14.143(27)	0.703(14)
	t_0 + 80 ns	13.607(39)	0.755(20)
	t_0 + 90 ns	13.106(59)	0.797(30)

$(Zn^{2+})^*$

Unlike for Zn^0 and Zn^{1+}, the Zn^{2+} velocity distributions measured in the presence of oxygen (Figure 3.24) differ greatly in comparison with the results obtained *in vacuo* (cf. page 66). While the situation is not dramatically altered at high irradiance, we find that, below about 3 GW/cm^2, the previously observed "fast" source term (i.e., the formation mechanism for which space charge–induced acceleration is most apparent) is essentially absent, and quasi-thermal profiles are observed in both the high and the low irradiance regime. This may be indicative either of the nonexistence of this formation channel altogether under these conditions, or the collisional quenching of $(Zn^{2+})^*$ by (or reaction with) the ambient oxygen.

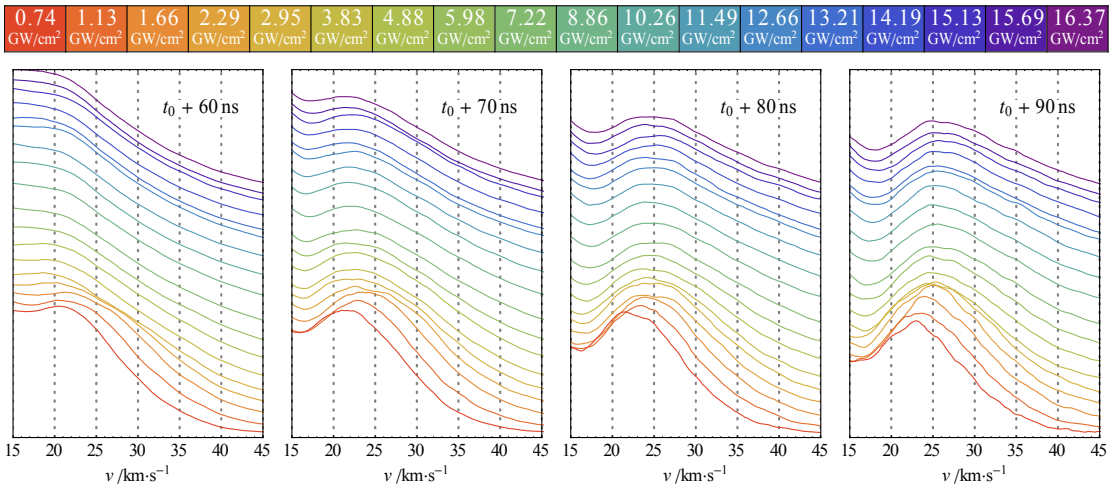

Figure 3.24: Velocity-space distributions of $(Zn^{2+})^*$ optical emission resulting from the 355 nm ablation of Zn under 50 mTorr of oxygen.

Although the possible role of the background gas in inhibiting the formation of a space-charge layer was not supported by the $(Zn^{1+})^*$ spatial profiles, it is nonetheless a plausible explanation for the effect observed presently. According to Dreyfus,[33] three-body (electron-ion) recombination plays a central role in the dynamics of the plasma,[m] and is more significant the lower the electron temperature (with the recombination rate scaling as $\hat{T}_e^{-9/2}$), i.e. predominantly at low irradiance and/or long after the laser pulse has ended. Clearly, it is also dependent on the density of species (evidently greater for expansion into ambient gas) able to absorb part of the kinetic energy of either (or both of) the electron and/or ion in order to facilitate recombination (i.e., play the part of the third body), which is more important for higher-energy ions. Here the attenuation of the "fast" channel is more significant for larger t_g, which is consistent with the expected cooling of the plume over time and increased pressure at the expansion front as progressively more of the background oxygen is displaced. The total $(Zn^{2+})^*$ optical emission yield is also somewhat less than *in vacuo*, which is as anticipated if some of the Zn^{2+} ions undergo recombination. However, the absence of any impact on the $(Zn^{0})^*$ and $(Zn^{1+})^*$ velocity distributions suggests that, if indeed three-body recombination accounts for the current observations, the product is not formed with (or does not retain) significant electronic

[m] Namely, because of its influence on the electron number density, recombination strongly reduces the inverse bremsstrahlung absorption cross-section and thus the extent of direct plasma heating by incident laser radiation.

excitation.[n] Therefore, it is also worth noting the possibility that $(Zn^{2+})^*$ at the leading edge of the plume may simply be collisionally de-excited without necessarily undergoing recombination. These effects are, of course, not mutually exclusive.

Given the negligible impact on $(Zn^{0})^*$ and limited effect on $(Zn^{1+})^*$, as discussed above, the processes underlying ablation appear to remain substantially unchanged in the presence of the background gas, and we should therefore further consider direct interaction between $(Zn^{2+})^*$ and O_2. Koyanagi *et al.*[43] have noted that Zn^{1+} has a rather small O-atom affinity of 1.67 eV; when compared with the O-atom affinity of another O atom, which is 5.16 eV, it is therefore clear that the lower charge state is relatively unreactive toward O_2 under ordinary conditions. If their conclusions also hold for the rather energetic Zn^{1+} ions produced in the present case, and if the reaction of $(Zn^{2+})^*$ with O_2 can be assumed rather more favourable, this may also explain why no modification of the $(Zn^{1+})^*$ spatial profiles is observed, whereas those of $(Zn^{2+})^*$ are quite noticeably altered.

Table 3.18: Fitted scale and exponent (according to Equation 3.2) for each of the trends indicated in Figure 3.25 corresponding to the dependence of the optical emission yield of $(Zn^{2+})^*$ on the irradiance at 355 nm for the ablation of Zn under oxygen.

t_g	$0.74 \leq I \leq 2.95$ GW/cm^2		$2.95 \leq I \leq 16.37$ GW/cm^2	
	Scale A	Exponent n	Scale A	Exponent n
t_0 + 60 ns	10.606(11)	1.281(14)	10.976(27)	0.964(12)
t_0 + 70 ns	10.081(17)	1.181(23)	10.349(32)	0.955(14)
t_0 + 80 ns	9.685(27)	1.090(38)	9.914(14)	0.911(6)
t_0 + 90 ns	8.411(38)	0.931(56)	9.517(22)	0.890(10)

In view of the apparent mechanistic differences, it is interesting to compare the yield curves for Zn^{2+} under oxygen with those obtained *in vacuo*. While the point of intersection between the low- and high-irradiance regimes remains approximately the same, the power law exponents are uniformly greater than was the case previously, and the scale factors are smaller (i.e., the intensity of the observed emission is reduced) in the presence of the ambient gas. These findings are suggestive of a smaller, or shorter lived (electronically excited) Zn^{2+} population; that is, the optical

[n] In principle, this observation might also indicate that the $(Zn^{2+})^*$ yield is insignificant relative to that of the less energetic species, since the relative populations are not known. However, if this were the case, it would be more difficult to rationalize the effect of oxygen on the $(Zn^{1+})^*$ yields (see below).

emission yield due to the "fast" (low irradiance) channel appears to be absent, rather than (for example) being subsumed into the total with the velocity distributions merely blurred together. Lending further support to this hypothesis, the optical emission intensity decays more quickly under oxygen, even at high irradiance (where the spatial profiles are similar to those *in vacuo*): Equation 3.6 yields $k = 5.7(1) \times 10^7\ \mathrm{s}^{-1}$, versus $4.6(1) \times 10^7\ \mathrm{s}^{-1}$ without background gas; the corresponding average power law exponents are 0.936(15) and 0.814(18), respectively. We may thus reasonably infer that electronically excited Zn^{2+} is strongly quenched (whether by a collisional or reactive mechanism) in the presence of ambient oxygen. It is therefore not necessarily the case that the latter also implies significant electron capture, particularly given the high electron temperature likely to occur at the expansion front.

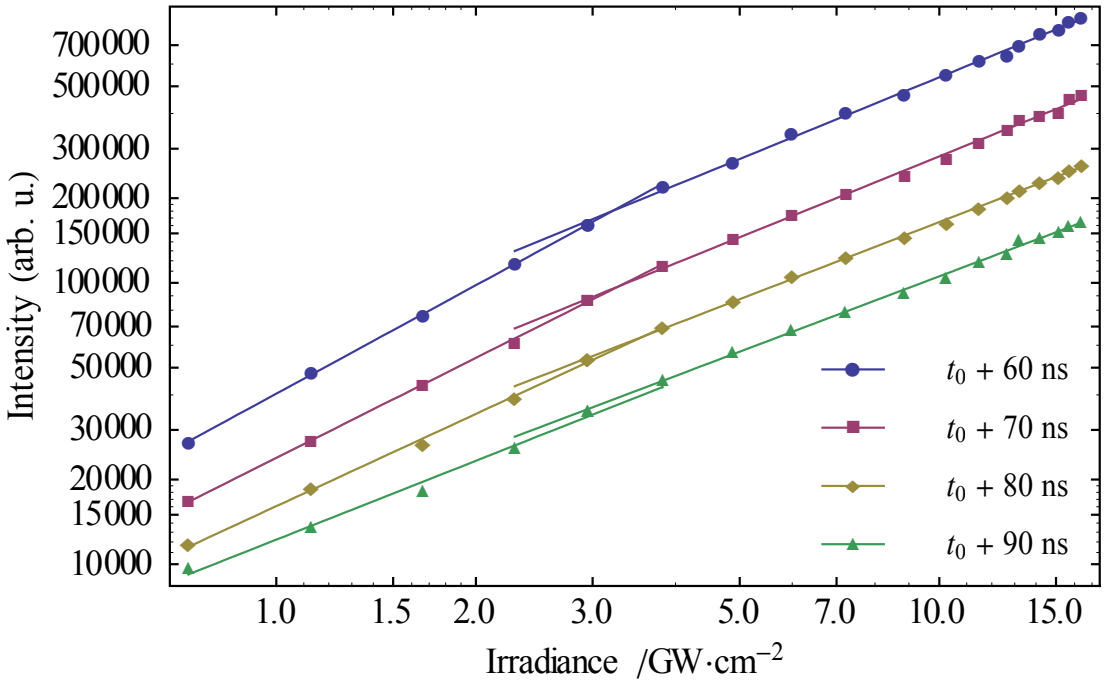

Figure 3.25: Variation with laser irradiance of the optical emission yield of $(Zn^{2+})^*$, as produced in the 355 nm ablation of Zn under $p(O_2) = 50$ mTorr. The overlaid line segments correspond to power laws per Equation 3.2.

Despite the findings enumerated above, the appearance threshold for $(Zn^{2+})^*$ optical emission, 0.335(24) GW/cm^2, is not dramatically altered from the previous value of 0.399(14) GW/cm^2. The magnitude of the change is comparable to that already seen for Zn^{1+}, for which the impact of introducing oxygen on the yield curves and spatial

distributions was obviously much less pronounced. The power law exponents obtained by fitting to Equation 3.4 (given in Table 3.19, below) support the conclusions already drawn from the results according to Equation 3.2.

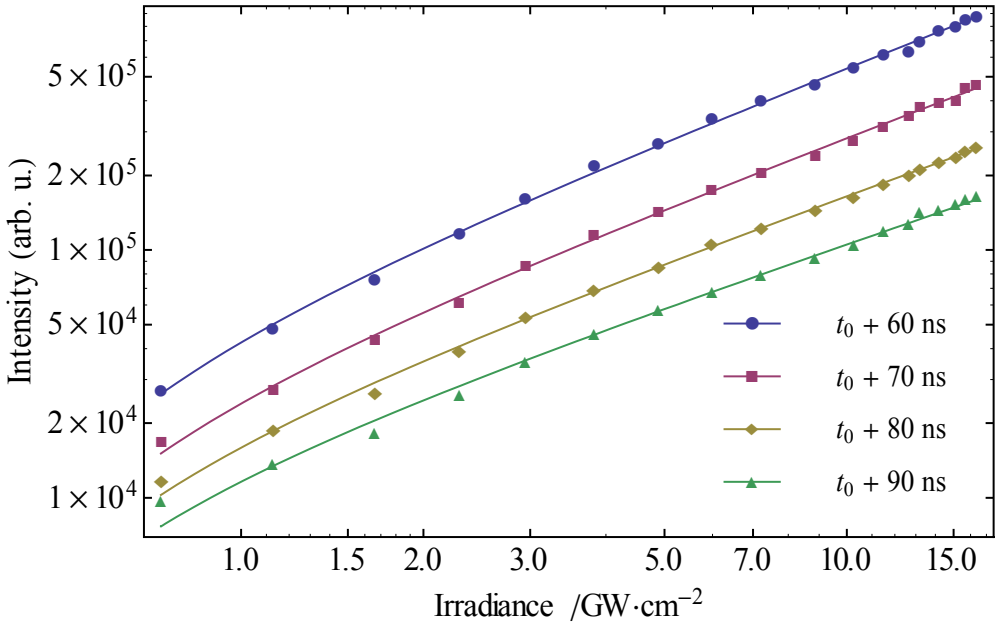

Figure 3.26: Variation with laser irradiance of the optical emission yield of $(Zn^{2+})^*$, as produced in the 355 nm ablation of Zn in the presence of oxygen at 50 mTorr. The overlaid curves are given by Equation 3.4 as fitted to the data.

Given the foregoing observations on $(Zn^{2+})^*$, we now arrive at an apparently reasonable interpretation of why the $(Zn^{1+})^*$ yields in the presence of oxygen are altered in the specific fashion described in the previous section. If indeed Zn^{2+} ions that would otherwise constitute the high-KE population undergo collisional or reactive quenching under these conditions, then clearly the energy lost by these species (and quite possibly also the electrons in the associated space charge layer, *via* three-body recombination) must be transferred to the remainder of the plasma and the surrounding gas at the expansion front. Since the $(Zn^{1+})^*$ formation mechanism appears to be predominantly (if not exclusively) thermal, we may anticipate that, under conditions for which a substantial quantity of $(Zn^{2+})^*$ is lost through these channels, the plume temperature may as a result rise sufficiently to bring about a slight increase in the ionization fraction. This model provides a rationalization for the increased $(Zn^{1+})^*$ yield at high irradiance, as the plume temperature should scale with the amount of $(Zn^{2+})^*$ available to be captured. Furthermore, if this latter quantity is

negligible, $(Zn^{1+})^*$ (as the highest charge state) then interacts directly with the surrounding oxygen, so that we may understand the corresponding decrease in its yield at low irradiance as resulting from comparable loss processes to those acting on $(Zn^{2+})^*$.

Table 3.19: Fitted threshold, scale, and exponent (according to Equation 3.4) for each of the trends indicated in Figure 3.26, corresponding to the dependence of the optical emission yield of $(Zn^{2+})^*$ on the irradiance at 355 nm for the ablation of Zn under 50 mTorr of oxygen.

$I_{threshold}$	t_g	$0.74 \leq I \leq 16.37$ GW/cm^2	
		Scale A	Exponent n
0.335(24) GW/cm^2	t_0 + 60 ns	11.042(25)	0.951(10)
	t_0 + 70 ns	10.461(31)	0.921(14)
	t_0 + 80 ns	10.032(40)	0.873(19)
	t_0 + 90 ns	9.695(52)	0.824(27)

$(Zn^{3+})^*$

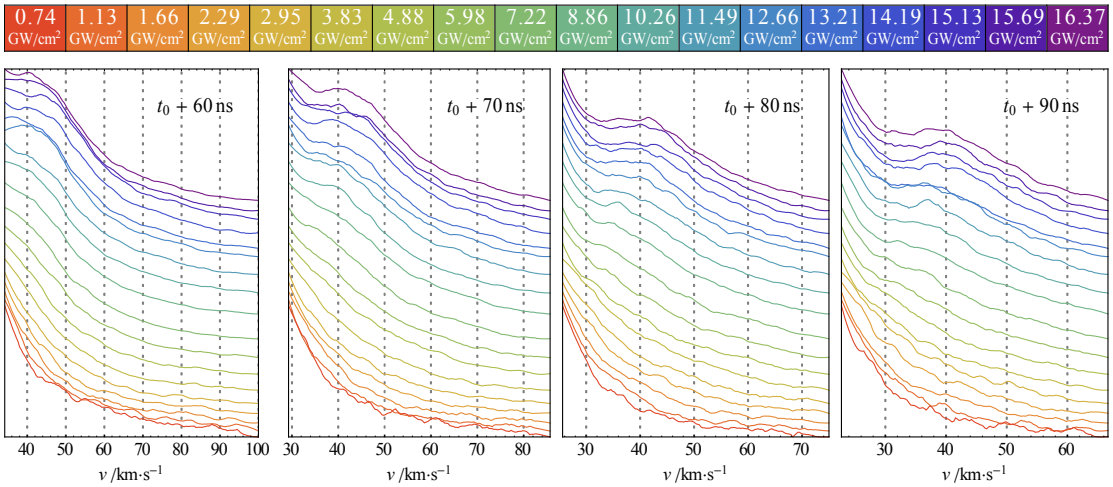

Figure 3.27: Spatial (velocity) distribution of $(Zn^{3+})^*$ optical emission resulting from the ablation of Zn at 355 nm under $p(O_2)$ = 50 mTorr.

$(Zn^{3+})^*$ emission is virtually absent in the presence of oxygen, which can readily be understood as the result of the same processes, i.e. either collisional or reactive quenching, that account for the corresponding reduction in $(Zn^{2+})^*$ yield. Unfortunately, the weak $(Zn^{3+})^*$ lines lie close to, and are subject to significant interference from, the wings of the somewhat broadened 468.014 nm $(Zn^0)^*$ line, as is apparent from Figure 3.27, and since the $(Zn^0)^*$ emission intensity itself varies with irradiance, this partial overlap presents some analytical difficulty. As a result, we do not attempt to quantify the scaling of the $(Zn^{3+})^*$ yield with irradiance, commenting

instead only on the nearly constant modal velocity of ≈ 40 km/s, which accords well with the minimum velocity observed for Zn^{3+} *in vacuo*. Although space-charge–mediated acceleration is still likely to account for the large observed Zn^{3+} velocity, the ≈ 600 eV of kinetic energy imparted by this process is clearly independent of irradiance,[o] indicating that the time integral of the accelerating force (i.e., the impulse) acting on Zn^{3+} is now strictly limited. While both the magnitude and duration of the acceleration are likely to be reduced in the presence of oxygen, given that the initial plasma density substantially exceeds that of the ambient medium it appears likely that the primary limitation is the latter, due to rapid expansion into (still) relative vacuum. In comparison with the appearance threshold of 1.45(6) GW/cm^2 *in vacuo*, a much greater value of roughly 4–5 GW/cm^2 (as estimated from the spatial profiles) applies under oxygen, which is suggestive of the greater relative importance of multiphoton ionization under the present conditions. Indeed, if $(Zn^{3+})^*$ cannot feasibly be produced thermally, and if ambient oxygen tends to promote electron-ion recombination, as has been argued above, then the reduced scope for collisional ionization (by energetic electrons having undergone inverse bremsstrahlung absorption) may render MPI the most favourable remaining formation mechanism even despite the requirement for ≈ 20-photon absorption. As this process is unlikely to depend significantly on the environment, given the observed yield and velocity scaling behaviour we propose that both mechanisms could apply simultaneously (and potentially synergistically) *in vacuo*. Nonetheless, although (as stated previously) 34-photon absorption at a metal surface has been described by Varró and Ehlotzky,[35] further work is needed in order to establish whether similar processes can be responsible for enhancement of the otherwise very small probability of 20th-order MPI under the present conditions.

[o] We do not discount the possibility that the acceleration may be only indirectly dependent on irradiance *via* the total amount of $(Zn^{3+})^*$ produced, but since it is difficult to determine which of these is actually the case, we apply *lex parsimoniae* and assume that a direct relationship exists.

3.3.3 ZINC OXIDE *IN VACUO*

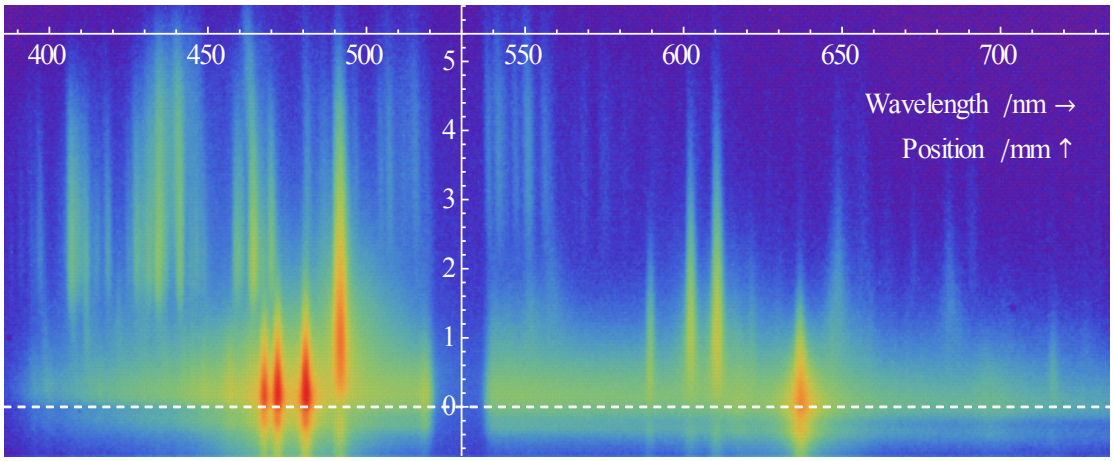

Figure 3.28: Spatiospectral image recorded at $t_g = t_0 + 80$ ns subsequent to the 355 nm ablation of ZnO *in vacuo* with irradiance $I = 6.95$ GW/cm^2.

(Zn^0)*

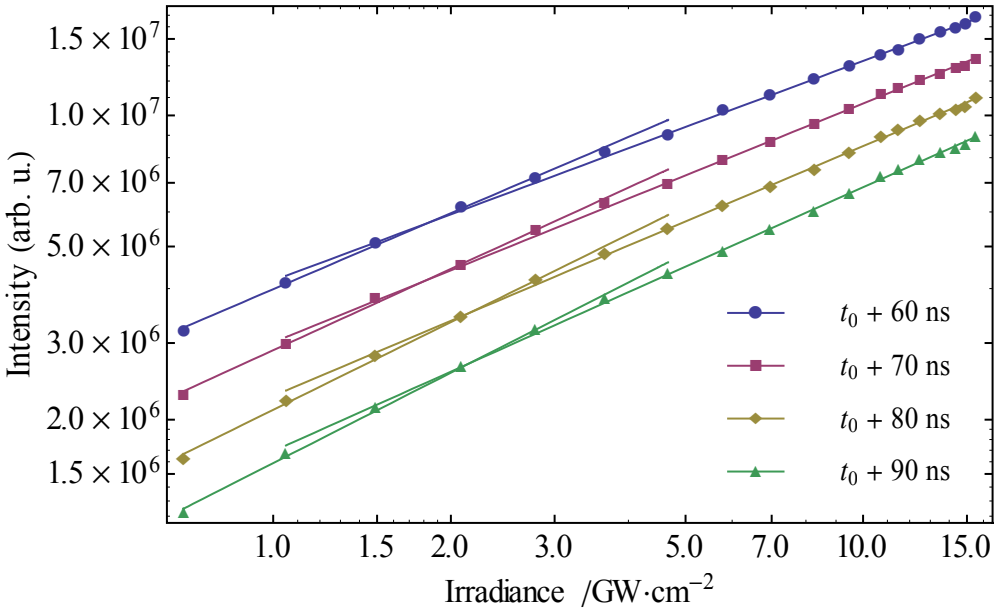

Figure 3.29: Variation with laser irradiance of the optical emission yield of (Zn^0)*, as produced in the 355 nm ablation of ZnO *in vacuo*. The overlaid line segments correspond to power laws per Equation 3.2.

In view of the radically different thermal properties of ZnO, the (Zn^0)* optical emission yield curves for ablation at 355 nm are strikingly similar to those of Zn (cf. page 54). Nonetheless, important differences exist, the most readily apparent of which are the reduced threshold, 2.0(2) versus 3.7(2) GW/cm^2, for which a reduction in the

power law exponents is observed, and the relative similarity of the trends above and below this value, with $\Delta n = 0.08(1)$ here against a previous value of 0.31(1).

Table 3.20: Fitted scale and exponent (according to Equation 3.2) for each of the trends indicated in Figure 3.29, corresponding to the dependence of the optical emission yield of $(Zn^0)^*$ on the irradiance at 355 nm for the ablation of ZnO *in vacuo*.

t_g	$0.70 \leq I \leq 3.65$ GW/cm^2		$4.67 \leq I \leq 15.54$ GW/cm^2	
	Scale A	Exponent n	Scale A	Exponent n
t_0 + 60 ns	15.199(8)	0.581(11)	15.244(13)	0.505(6)
t_0 + 70 ns	14.876(11)	0.621(15)	14.918(13)	0.549(6)
t_0 + 80 ns	14.561(13)	0.669(17)	14.633(14)	0.574(6)
t_0 + 90 ns	14.278(11)	0.689(14)	14.342(17)	0.607(8)

The origin of this discrepancy is perhaps better demonstrated with reference to the analysis according to Equation 3.4 (Figure 3.30 and Table 3.21), from which it is clear that the power law exponents for the $(Zn^0)^*$ optical emission yield differ negligibly between Zn and ZnO when the complete irradiance range is considered. In this case, Δn is found as −0.001(7) (i.e., it is statistically equal to zero) and the two materials are differentiated only by their ablation thresholds, these being 0.393(18) and 0.248(9) GW/cm^2 for Zn and ZnO respectively.

Table 3.21: Fitted threshold, scale, and exponent (according to Equation 3.4) for each of the trends indicated in Figure 3.30, corresponding to the dependence of the optical emission yield of $(Zn^0)^*$ on the irradiance at 355 nm for the ablation of Zn *in vacuo*.

$I_{threshold}$	t_g	$0.70 \leq I \leq 15.54$ GW/cm^2	
		Scale A	Exponent n
0.248(9) GW/cm^2	t_0 + 60 ns	15.347(6)	0.467(3)
	t_0 + 70 ns	15.034(6)	0.504(3)
	t_0 + 80 ns	14.732(7)	0.539(4)
	t_0 + 90 ns	14.454(8)	0.564(5)

Given the much higher melting point of ZnO (approximately 2 248 K), it is perhaps counterintuitive that its ablation threshold should be *lower* than that of the pure metal. However, Lamoreaux *et al.*[44] have calculated based on other thermodynamic data that the vapour pressure of Zn rises rapidly with temperature due to thermal decomposition of ZnO even far below this value; at ≈ 1 300 K it is already approximately equal to the opposing radiation pressure for an irradiance of 1 GW/cm^2 (33.4 kPa GW^{-1} cm^2). According to Gadzhiev,[45] the thermal conductivity and

volumetric heat capacity of solid ZnO are 35 W m^{-1} K^{-1} and 2.82 J K^{-1} cm^{-3} respectively, which are not drastically different from the corresponding values for liquid Zn. A similar, pseudo-phase explosion mechanism may therefore plausibly account for the Zn^0 yield from both Zn and ZnO, with the latter undergoing a rapid *thermochemical* (rather than purely thermodynamic) phase change shortly after the confining pressure is removed when irradiation ceases. In this light, the reduced ablation threshold relative to Zn can be understood as the result of stronger heating within a smaller volume due to a combination of resonant absorption[p] and the somewhat lower thermal conductivity of the oxide.

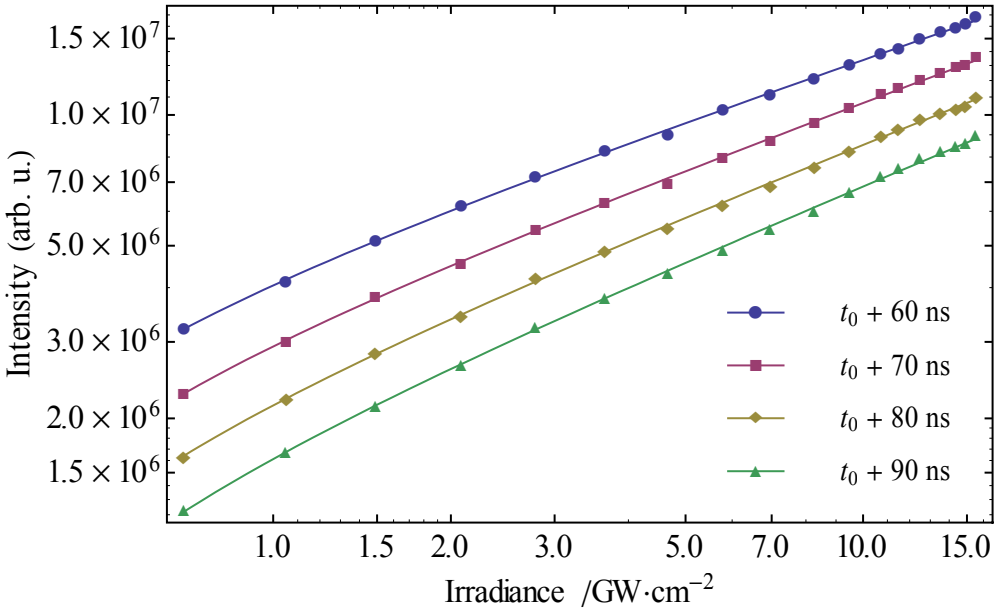

Figure 3.30: Variation with irradiance of the optical emission yield of (Zn^0)*, as produced in the 355 nm ablation of ZnO *in vacuo*. The overlaid curves are given by Equation 3.4 as fitted to the data.

The (Zn^0)* spatial profiles obtained from ZnO differ more substantially with respect to those from Zn than do the yield curves, however. The dependence of the modal velocity on irradiance is sharply reduced, while the value itself increases modestly from 2–3 to ≈ 3 km/s. Additionally, the hot tail of the distribution is more pronounced in the case of ZnO, with a significant fraction of the Zn atoms now possessing a mean velocity of 10–15 km/s, contrasting with the maximum (Zn^0)* velocity of ≈ 10 km/s observed in §3.3.1. As a result, the ablation behaviour of ZnO is not well modelled by

[p] The band-gap of ZnO is 3.37 eV, while the energy of a 355 nm photon is 3.49 eV.

a one-dimensional Maxwell–Boltzmann expansion, rather appearing strongly hyperthermal: a temperature of 19.2(2.4) eV adequately reproduces the measured distributions above 3 km/s, but does not correctly account for the observed behaviour at lower velocities. This is, of course, unsurprising; thermal equilibrium at such a high temperature is not possible under the present conditions since the maximum radiation pressure is far below that necessary to meaningfully confine a gas of $\approx 10^{20}$ Zn atoms and electrons at $\hat{T} \approx 20$ eV, so that a plasma somehow formed with this initial temperature would undergo essentially free (adiabatic) expansion.

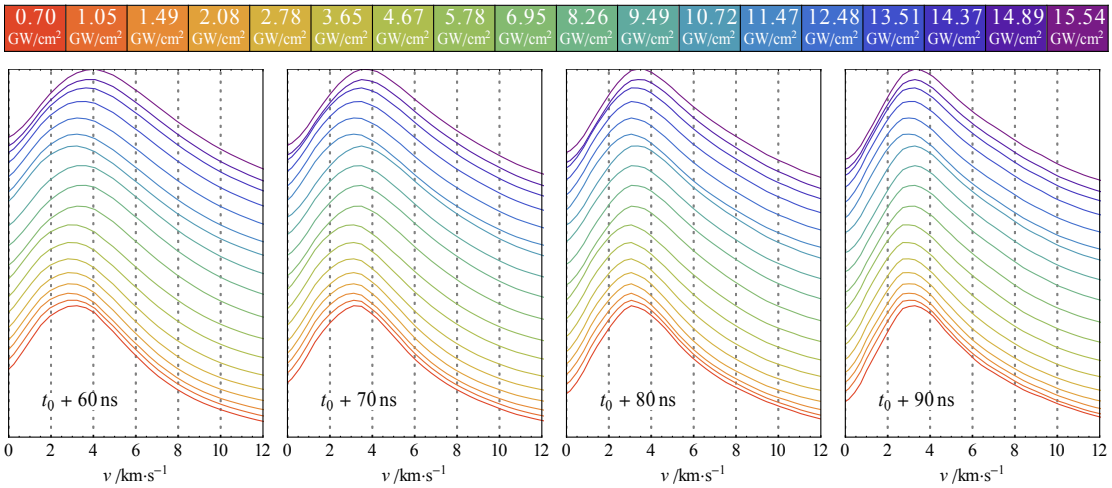

Figure 3.31: Velocity distributions of $(Zn^0)^*$ optical emission resulting from the 355 nm ablation of ZnO *in vacuo*.

The consistency of the $(Zn^0)^*$ spatial profiles with irradiance and their distinctness from those obtained in the ablation of Zn (cf. pp. 54, 76) both argue against an explanation of the close correspondence between the scaling laws for Zn and ZnO in terms of redeposition of Zn on the target surface. This effect has been suggested by Claeyssens *et al.*[46] to cause substantial non-stoichiometry of the ablated surface, with irradiation at 193 nm resulting in a roughly six-fold enhancement of the Zn atom surface density (as assessed by XPS), but with the corresponding measurements for O remaining essentially unchanged. Clearly, such a process might easily yield a spurious similarity with the results obtained for Zn and thus confound observations that may otherwise be assumed to relate to the ablation specifically of ZnO. Van Vechten[47] has also estimated that the enthalpies of formation for a Zn and an O vacancy are 5.41 eV and 3.00 eV, respectively, and since the energy of a 355 nm photon is only 3.49 eV (i.e., sufficient to form an O vacancy, but not a Zn vacancy) one might expect

the bias toward Zn enrichment of the surface to be even more pronounced than in the 193 nm ($\hbar\omega = 6.42$ eV) case. However, it is not clear to what extent this holds in practice, since the influence (if any) of Zn enrichment on plume dynamics is not readily apparent in the results discussed above.

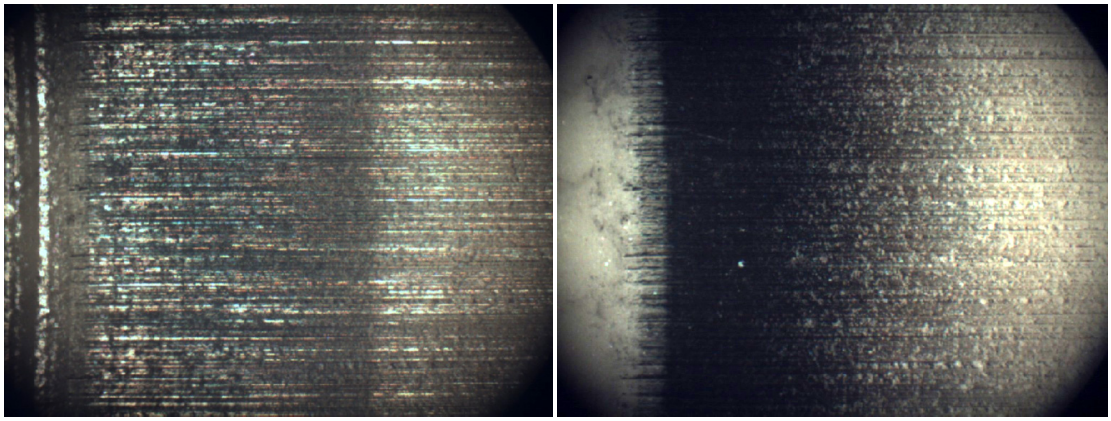

Figure 3.32: Photomicrographs (5 × magnification) of ZnO target surface after ablation *in vacuo* at 355 nm showing redeposited Zn (which appears black against the pale yellow oxide). The laser track is at the far left. Left/right panels are images of the same area under unpolarized/polarized light, respectively.

Photographs of the ZnO target after ablation at 355 nm *in vacuo* are presented in Figure 3.32, which shows a significant accumulation of Zn at the margins of the irradiated area after prolonged ablation.[q] However, the amount redeposited subsequent to a single ablation event appears to be quite limited. This is demonstrated more clearly in Figure 3.33, wherein the area irradiated by each laser pulse can be seen under polarized light to be free of metallic Zn; the metallic (or submetallic) lustre observed under ordinary illumination is rather that of ZnO itself. Thus, while redeposition certainly does occur under the present conditions, it would seem that Zn condenses preferentially outside of the ablated region and so is unlikely to represent a large proportion of the ablated material.

[q] Each experiment in the present work lasted for approximately 8 hours, during which time ≈ 72 000 laser pulses (4 000 for each irradiance value) were produced and the target underwent ≈ 480 complete revolutions. The accumulated number of pulses falling on a given area was therefore approximately 150.

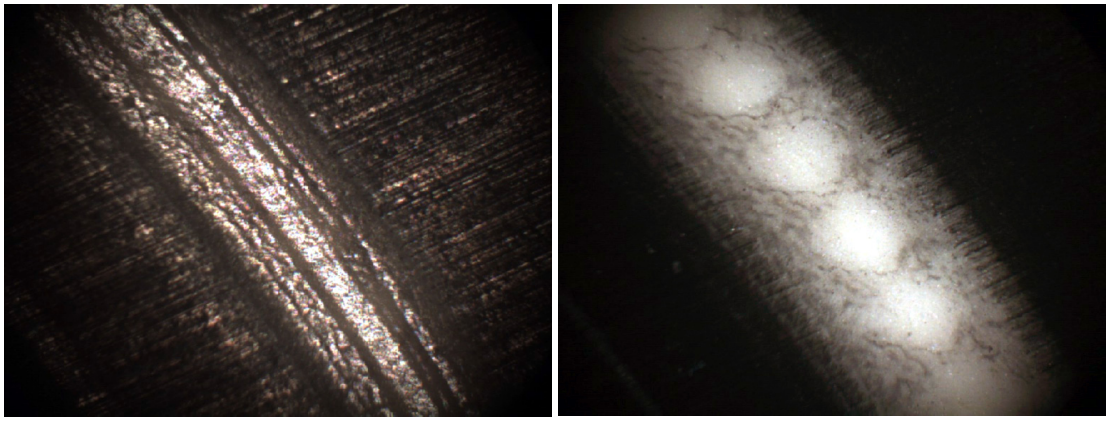

Figure 3.33: Photomicrographs (5 × magnification) of ZnO target surface after ablation *in vacuo* at 355 nm. Left/right panels are images of the same area under unpolarized/polarized light, respectively.

$(Zn^{1+})^*$

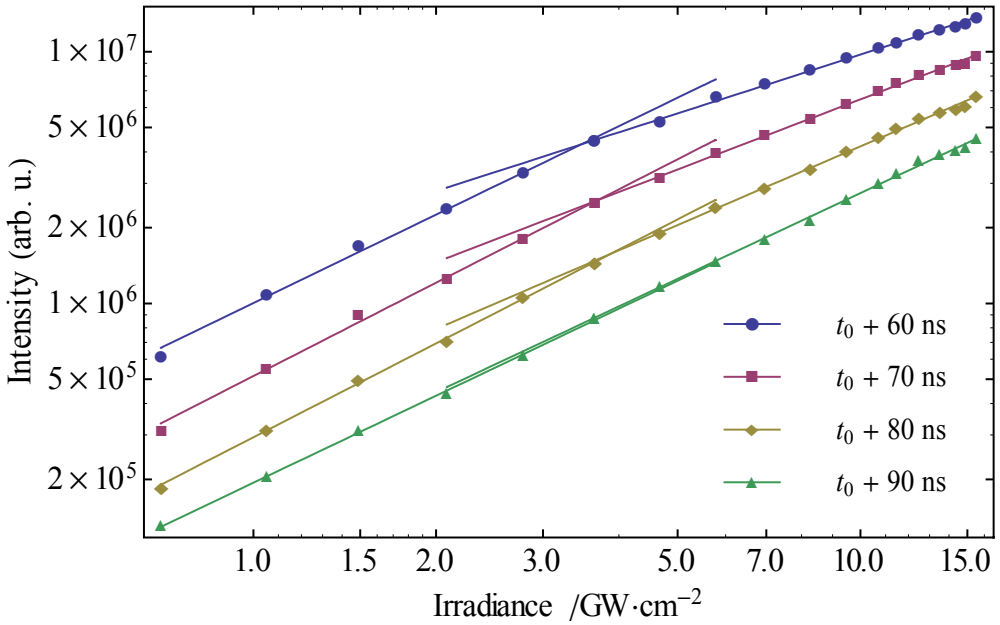

Figure 3.34: Variation of the optical emission yield of $(Zn^{1+})^*$ with laser irradiance, as recorded subsequent to the ablation of ZnO *in vacuo* at 355 nm. The overlaid line segments correspond to power laws per Equation 3.2.

The power law exponents characterizing the $(Zn^{1+})^*$ optical emission yield from ZnO are considerably larger than for the metal, and those above the point of intersection at $I = 3.7(2)$ GW/cm^2 are also time-dependent, rising from 0.776(11) at $t_g = t_0 + 60$ ns to 1.131(14) at $t_0 + 90$ ns. This is somewhat more pronounced than was observed for Zn ablated under oxygen, with an increase of 0.355 presently as compared to 0.241 in the

previous case; the behaviour at low irradiance and the location of the threshold, however, remain similar.

Table 3.22: Fitted scale and exponent (according to Equation 3.2) for each of the trends indicated in Figure 3.34, corresponding to the dependence of the optical emission yield of $(Zn^{1+})^*$ on the irradiance at 355 nm for the ablation of ZnO *in vacuo*.

t_g	$0.70 \leq I \leq 3.65$ GW/cm^2		$3.65 \leq I \leq 15.54$ GW/cm^2	
	Scale A	Exponent n	Scale A	Exponent n
t_0 + 60 ns	13.819(32)	1.167(35)	14.305(23)	0.776(11)
t_0 + 70 ns	13.151(30)	1.232(32)	13.552(27)	0.925(12)
t_0 + 80 ns	12.591(18)	1.239(19)	12.862(30)	1.038(13)
t_0 + 90 ns	12.174(19)	1.150(21)	12.219(31)	1.131(14)

The $(Zn^{1+})^*$ spatial profiles obtained for a ZnO target reveal significantly different velocity distributions than those observed from metallic Zn either *in vacuo* or under $p(O_2)$ = 50mTorr. Most notably, pronounced bimodality at low irradiance is now observed, for which no analog was seen in the $(Zn^0)^*$ distributions. Interestingly, neither of the modal velocities, ≈ 5 and ≈ 15 km/s, correspond closely to that of $(Zn^{1+})^*$ as obtained in the ablation of Zn (≈ 7–8 km/s), suggesting that rather different formation/acceleration mechanisms apply in each case. Nonetheless, the behaviours of the two materials do converge at high irradiance; the discrepancy no longer exists above ≈ 10 GW/cm^2, which lends additional weight to the assignment of the $(Zn^0)^*$ velocity distributions as essentially thermal in origin, since we expect most dynamical information to be lost and collective (ensemble) effects to dominate under strongly saturated conditions.

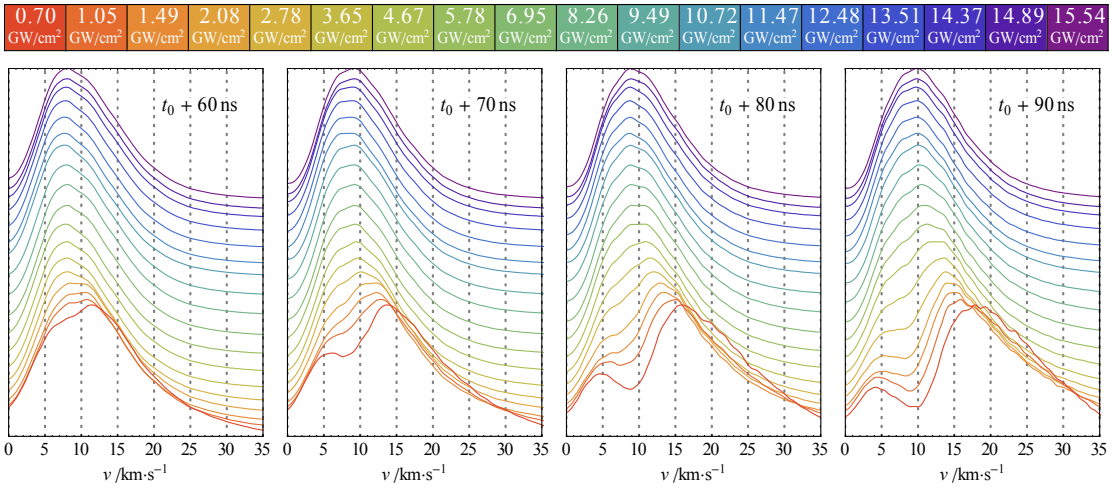

Figure 3.35: Spatial distribution of (Zn^{1+})* optical emission resulting from the ablation of ZnO at 355 nm *in vacuo*.

Leuchtner[48] has commented on the origin of a bimodal distribution of ion velocities, albeit based on experimental data of potentially questionable validity.[r] Working with $\lambda = 248$ nm and at low irradiance (fluence $F \leq 2.5$ J/cm^2, as compared to our minimum value of $F = 8.3$ J/cm^2 at $I = 0.70$ GW/cm^2), he observed a slow Zn^{1+} formation channel imparting ≈ 5 eV of kinetic energy. This value, too small to present instrumental difficulties, is not in serious doubt, and corresponds to a velocity of ≈ 4 km/s, in good agreement with our results at low irradiance. Leuchtner suggests, and more specifically Khan *et al.*[49] have recently argued, that this probably represents the energy of a Zn ion electrostatically ejected from a (net positive) region in which a high density of O vacancies exists, which as we have seen above probably applies to much of the ablated area. This mechanism is, due to melting of the ZnO surface, unlikely still to represent a major contribution toward the Zn^{1+} yield at high irradiance, thus accounting for the lack of structure in the KE distributions obtained under such conditions.

[r] As discussed earlier, Leuchtner performed a quadrupole mass filtered time-of-flight (QMF-TOF) experiment very similar to that previously attempted by the present author. The TOF data he obtained for Zn^{1+} (produced by the 248 nm ablation of ZnO *in vacuo*) exhibit strong oscillations characteristic of unstable transmission through the QMF, so that the component of the previously reported kinetic energy distributions at ≈ 100 eV was in fact almost certainly due to Zn^{2+}. This does not, of course, invalidate Leuchtner's argument as to why a bimodal Zn^{1+} KE distribution might arise in principle.

The identity of the fast component of the $(Zn^{1+})^*$ velocity distribution is less clear, however, and the modal energy of ≈ 75 eV (15 km/s) is substantially larger than the value of ≈ 17 eV (≈ 7 km/s) given in the prior work. Although discrimination between Zn^{1+} and Zn^{2+} would have been difficult for $E_k \gtrsim 20$ eV in the mass-spectrometric experiment, the smaller value may also be representative of Zn^{1+} in its electronic ground state, so that in fact three distinct formation mechanisms might exist. It is interesting to note that Leuchtner was able to produce Zn^{2+} by photoionization of the ablation products, thus measuring a kinetic energy for $(Zn^{1+})^*$ close to that reported here; the kinetic energy distribution of $(Zn^0)^*$ was also determined, with a maximum of ≈ 40 eV (≈ 11 km/s) corresponding quite well to that reported in the previous section. Although these species were suggested to be metastable states, it should be pointed out that the emission lines observed in the present work involve upper states quite near to the respective ionization limits (cf. Table 3.1 and Table 3.2). Indeed, the 636.235 nm $(Zn^0)^*$ line originates 7.74 eV above the ground state, reflecting an atom which will be ionized by absorption of a single 532 nm photon (the wavelength employed by Leuchtner for this purpose), while the observation of the 610.249 nm line of $(Zn^{1+})^*$ implies (at least) 14.63 eV of electronic excitation, so that two-photon absorption is sufficient.

Marine *et al.*[50] have revisited the photoelectron-induced acceleration mechanism (first proposed by Peurrung *et al.*[18] for metals) as it applies to the ablation of a semiconductor (namely, silicon), considering its role within a more general model incorporating target melting, electrostatic ablation, and plasma formation. Rather than being limited by space charge, these authors argued that, in the nanosecond regime, photoelectron emission is balanced (for sufficiently high, but still rather small fluence) by the field-induced ejection of positive ions, and that in contrast to the case of sudden Coulomb explosion, these processes occur continuously until the target finally melts and begins to vaporize. A careful numerical modelling study[s] showed that, prior to melting, an extremely powerful electric field is produced at the Si surface that is sufficient to eject Si^+ ions electrostatically (and, in fact, is self-limited

[s] Marine *et al.* constructed a rather complicated model explicitly accounting for most of the relevant physical processes. The primary limitations were due to their continuum approach (so that they would not have predicted, for example, the results of Khan *et al.*) and that it was not possible to consider the result of the electrostatic and thermal ablation mechanisms acting together.

exactly by this process, with a maximum amplitude of $\approx 2.5 \times 10^8$ V/cm attained for $F \geq 0.4$ J/cm^2). Although Marine *et al.* were not directly able to consider the effect of surface charge at the moment of melting, they speculated that this leads to an enhancement of the ablation rate in the brief period before the effect of the accumulated charge is nullified by band-gap collapse occurring along with the solid–liquid phase transition. It is important to note that, as pointed out by the authors of the previous work, the critical field strength required for electrostatic ablation to occur can only be reached if the photoelectron yield is large, which generally implies deep-UV irradiation. In the present case, $\hbar\omega \approx E_{gap}$, so that this cannot apply.[t] Instead, a more modest charge (yet still sufficient to desorb Zn^{1+} from defect sites) will accumulate, and this is likely to lead to a Coulomb explosion-like process when, with continuing irradiation, melting occurs and the cohesive energy of the material drops. We thus arrive at a plausible overall rationalization of the current observations, particularly given that melting will occur almost immediately at high irradiance and thus very little surface charge will develop in this case.

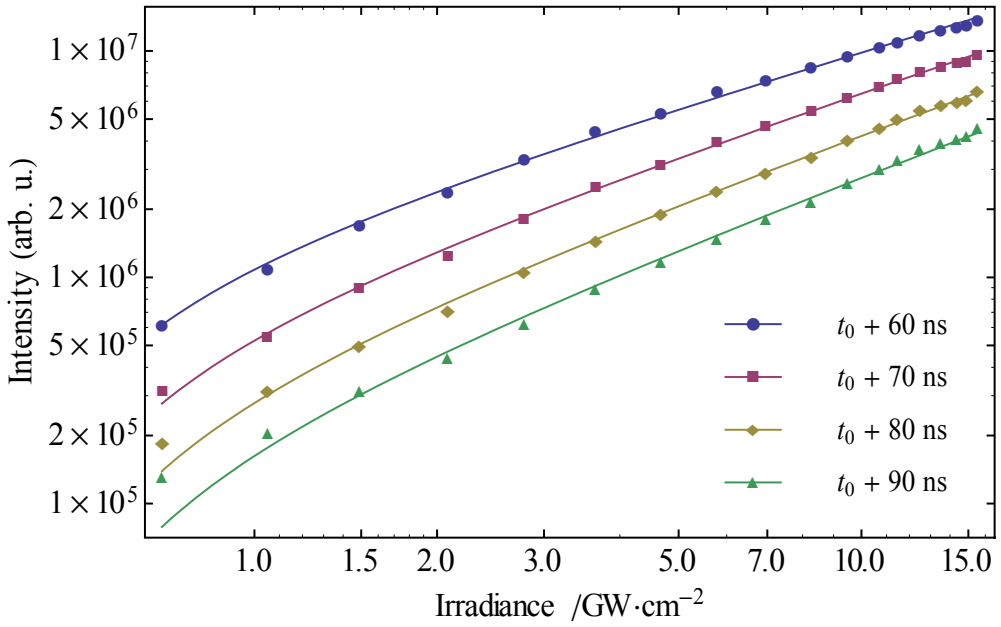

Figure 3.36: Variation with laser irradiance of the optical emission yield of $(Zn^{1+})^*$, as produced in the 355 nm ablation of ZnO *in vacuo*. The overlaid curves are given by Equation 3.4 as fitted to the data.

[t] Marien[51] has found the work function of zinc oxide to lie between 3.15(15) and 4.85(15) eV (for the Zn- and O-faces, respectively). Thus, photoelectrons will be emitted ($E_{gap} + \phi = 6.52$–8.22 eV) only after the absorption of either two or three photons at $\lambda = 355$ nm.

Considering briefly the analysis *via* Equation 3.4, it is apparent that the $(Zn^{1+})^*$ optical emission yield curves obtained from a ZnO target (Figure 3.36) strongly resemble those presented above for Zn ablated under oxygen (Figure 3.23, page 82) in overall form; furthermore, the $(Zn^{1+})^*$ appearance threshold is very similar in both cases. Although this appears physically justified above ≈ 7 GW/cm^2, whereupon analogous formation mechanisms apply, the similarity at low irradiance appears largely spurious. The power law exponents applicable to ZnO are, however, significantly larger, while the scale factors are smaller than in the previous case; this may be indicative of the initially weaker coupling of radiation into this material than into Zn, so that proportionally more energy is required to effect comparable electron emission. Additionally, the surface field gradient is likely to be greater in the case of the metal (since external electric fields are screened out of bulk conductive media), thereby further promoting field-assisted desorption.

Table 3.23: Fitted threshold, scale, and exponent (according to Equation 3.4) for each of the trends indicated in Figure 3.36, corresponding to the dependence of the optical emission yield of $(Zn^{1+})^*$ on the irradiance at 355 nm for the ablation of ZnO *in vacuo*.

$I_{threshold}$	t_g	$0.70 \leq I \leq 15.54$ GW/cm^2	
		Scale A	Exponent n
0.421(17) GW/cm^2	t_0 + 60 ns	14.323(19)	0.787(9)
	t_0 + 70 ns	13.660(26)	0.895(12)
	t_0 + 80 ns	13.065(39)	0.968(19)
	t_0 + 90 ns	12.548(61)	1.008(29)

$(O^{1+})^*$

Due to their logical consistency with the mechanism proposed to account for the $(Zn^{1+})^*$ data, the $(O^{1+})^*$ velocity distributions obtained from ZnO (Figure 3.37) are of significant value in confirming the validity of the former. In particular, the measurements obtained at low irradiance are strongly suggestive of the expected Coulombic desorption mechanism, while for higher powers this is apparently dominated by the thermal behaviour described previously. The bimodality formerly observed is absent in the present case, which however is easily rationalized given that the slow $(Zn^{1+})^*$ formation channel was assigned as being due to desorption of Zn ions that had been adjacent to O vacancies. Clearly, such a mechanism will not operate also in the reverse sense since a Zn vacancy possesses a net negative charge

that cannot cause the ejection of a cation. The modal velocity of ≈ 25 km/s corresponds reasonably well with the value of ≈ 10 km/s for $(Zn^{1+})^*$ given the relative masses of these species and the expectation that they are subject to the same accelerating field. Interestingly, similarities also exist with the $(Zn^{2+})^*$ data presented in §§3.3.1–3.3.2, which may imply that the discrepancy of ≈ 5 km/s (≈ 20 eV) can be accounted for by invoking a modest dynamic acceleration owing to the proximity of $(O^{1+})^*$ to the expansion front but limited by its relatively small charge.

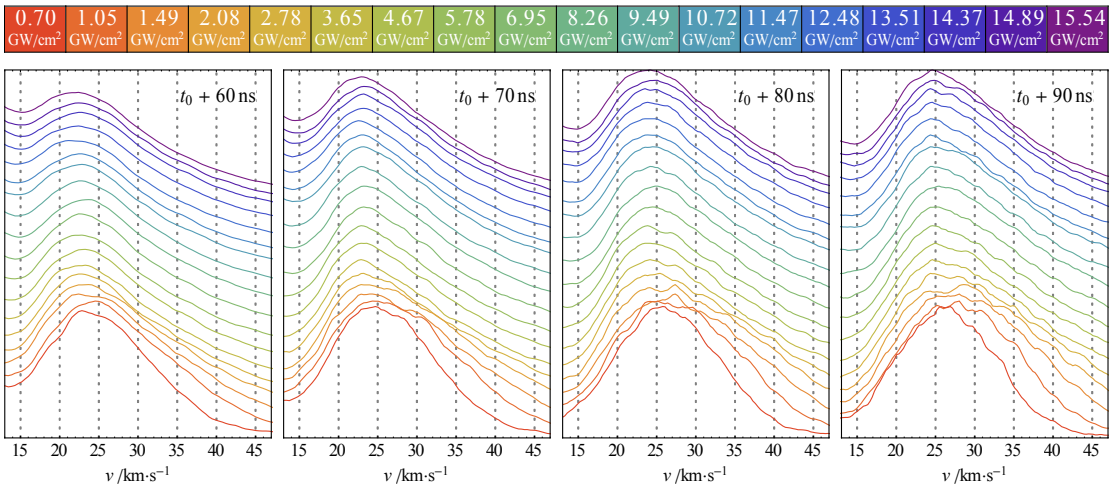

Figure 3.37: Spatial (velocity) distribution of $(O^{1+})^*$ optical emission resulting from the ablation of ZnO at 355 nm *in vacuo*.

The appearance threshold for $(O^{1+})^*$ is identical to that of $(Zn^{1+})^*$ produced under the same conditions, lending further weight to the conclusion that both ions are formed according to substantially the same mechanism. The scaling of emission intensity with irradiance differs, however, most notably in that the value of n increases with t_g rather than decreasing. Since $(O^{1+})^*$ lies at least partly within the space charge region, yet does not escape sufficiently from the plasma to undergo free expansion, this can be interpreted in terms of electron recapture, most probably facilitated by adiabatic expansion; in this sense $(O^{1+})^*$ again plays a similar role to that of $(Zn^{2+})^*$ observed previously.

Table 3.24: Fitted threshold, scale, and exponent (according to Equation 3.4) for each of the trends indicated in Figure 3.38, corresponding to the dependence of the optical emission yield of $(O^{1+})^*$ on the irradiance at 355 nm for the ablation of ZnO *in vacuo*.

$I_{threshold}$	t_g	$0.70 \leq I \leq 15.54$ GW/cm^2	
		Scale A	Exponent n
0.423(8) GW/cm^2	t_0 + 60 ns	10.558(9)	0.711(4)
	t_0 + 70 ns	10.280(10)	0.685(5)
	t_0 + 80 ns	10.073(11)	0.642(6)
	t_0 + 90 ns	9.891(12)	0.605(7)

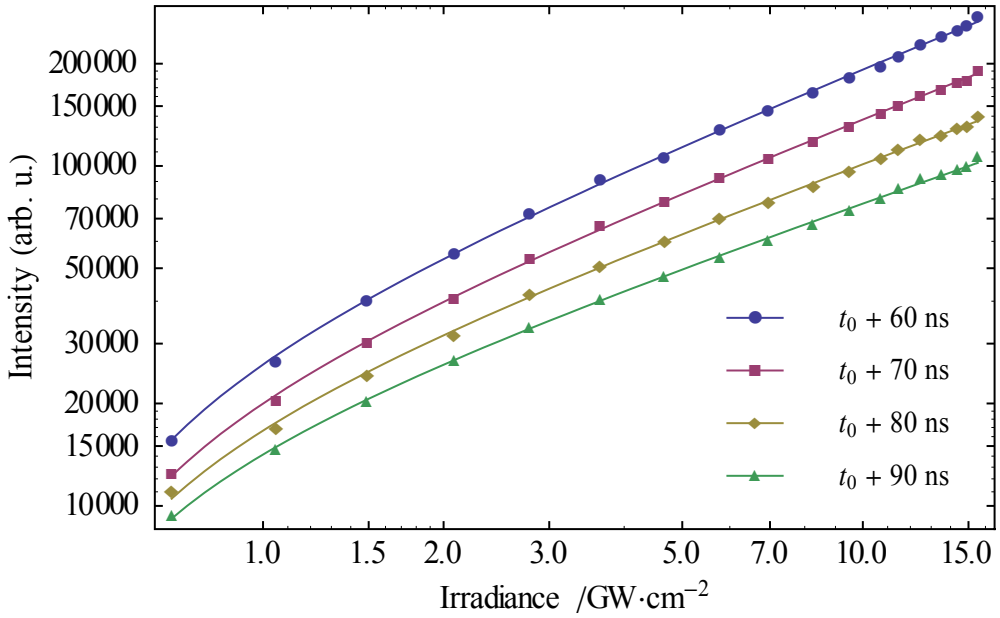

Figure 3.38: Variation with laser irradiance of the optical emission yield of $(O^{1+})^*$, as produced in the 355 nm ablation of ZnO *in vacuo*. The overlaid curves are given by Equation 3.4 as fitted to the data.

$(Zn^{2+})^*$

In view of the observations for $(O^{1+})^*$ enumerated above, it is interesting to consider whether the behaviour of $(Zn^{2+})^*$ within the ZnO plume is altered with respect to that of the Zn plasma. Given the apparent absence of $(Zn^{3+})^*$ from the oxide target, and in consideration of the fact that $(O^{1+})^*$ is likely to be significantly more abundant than $(Zn^{2+})^*$ due to its comparative energetic accessibility, two possible but mutually exclusive outcomes might result depending on the plume cooling rate. If cooling is rapid, it is likely that recombination between $(O^{1+})^*$ and the 'hot' fraction of electrons will strongly diminish the space charge-mediated acceleration of $(Zn^{2+})^*$. However, if the plasma temperature remains high over the timescale of the latter process then it

may be anticipated that the doubly charged species undergoes *stronger* acceleration due both to repulsion from the $(O^{1+})^*$ population (with which it is substantially collocated), and simultaneously an effective enhancement of the thermally-induced electric field due to the nonexistence of any higher charge state. It appears from Figure 3.39 that in fact the second possibility applies; the modal velocity of $(Zn^{2+})^*$ is now ≈ 40 km/s (≈ 550 eV), which is much greater than was observed from a Zn target and approaches that of $(Zn^{3+})^*$ seen previously. Nonetheless, since the intensity of $(Zn^{2+})^*$ emission is also strongly reduced, it is conceivable that this is also due (at least in part) to a reduced population of this species, which as a result interacts more strongly with the accelerating field.

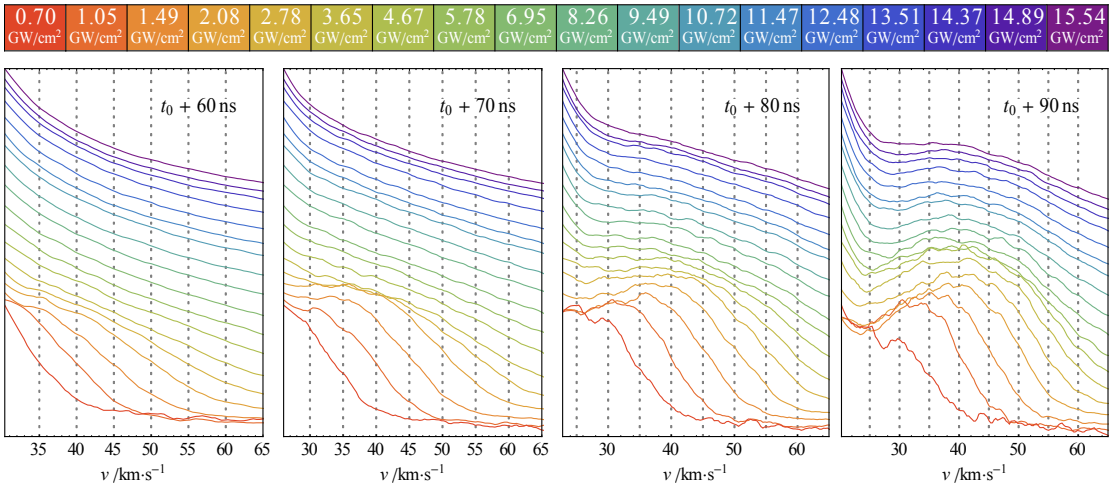

Figure 3.39: Spatial distribution of $(Zn^{2+})^*$ optical emission resulting from the 355 nm ablation of ZnO *in vacuo*.

Consideration of the fits to Equation 3.2 illustrates that both the point of intersection between the distinct scaling laws (i.e., 2.7–2.8 GW/cm^2) and the power law exponents below this threshold are unchanged with respect to the corresponding values for Zn as presented in Table 3.11. This finding is perhaps remarkable in view of the rather different velocity distributions applicable in the present case; clearly, the quantity of $(Zn^{2+})^*$ formed does not appear to depend on either the target material or the position of this species within the plasma. We are thus able to conclude that essentially the whole $(Zn^{2+})^*$ population is likely already to be present before significant plume expansion occurs, and that, *in vacuo*, the latter process is quasi-collisionless (at least after several tens of nanoseconds) so that no meaningful adiabatic cooling and electron-ion recombination can take place.

Table 3.25: Fitted scale and exponent (according to Equation 3.2) for each of the trends indicated in Figure 3.40, corresponding to the dependence of the optical emission yield of $(Zn^{2+})^*$ on the irradiance at 355 nm for the ablation of Zn *in vacuo*.

t_g	$0.70 \leq I \leq 2.78$ GW/cm^2		$2.78 \leq I \leq 15.54$ GW/cm^2	
	Scale A	Exponent n	Scale A	Exponent n
t_0 + 60 ns	10.288(26)	1.200(34)	10.549(21)	0.928(10)
t_0 + 70 ns	9.877(14)	1.155(19)	10.202(10)	0.837(5)
t_0 + 80 ns	9.650(22)	1.060(30)	9.987(9)	0.750(5)
t_0 + 90 ns	9.440(14)	1.032(20)	9.816(16)	0.677(8)

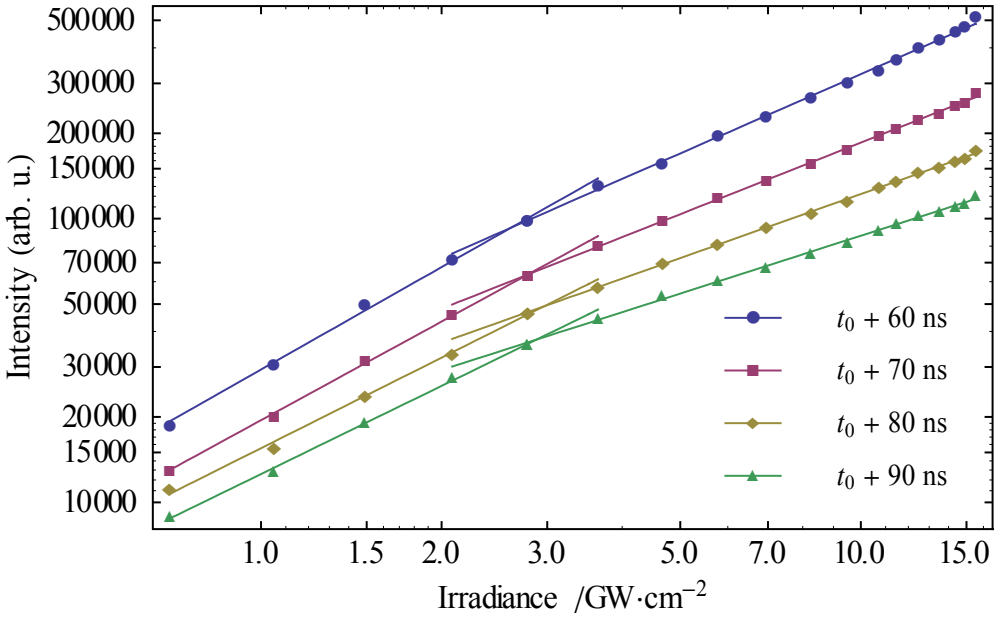

Figure 3.40: Variation with laser irradiance of the optical emission yield of $(Zn^{2+})^*$, as produced in the 355 nm ablation of ZnO *in vacuo*. The overlaid line segments correspond to power laws per Equation 3.2.

3.4 532 NM ABLATION OF ZINC

3.4.1 *IN VACUO*

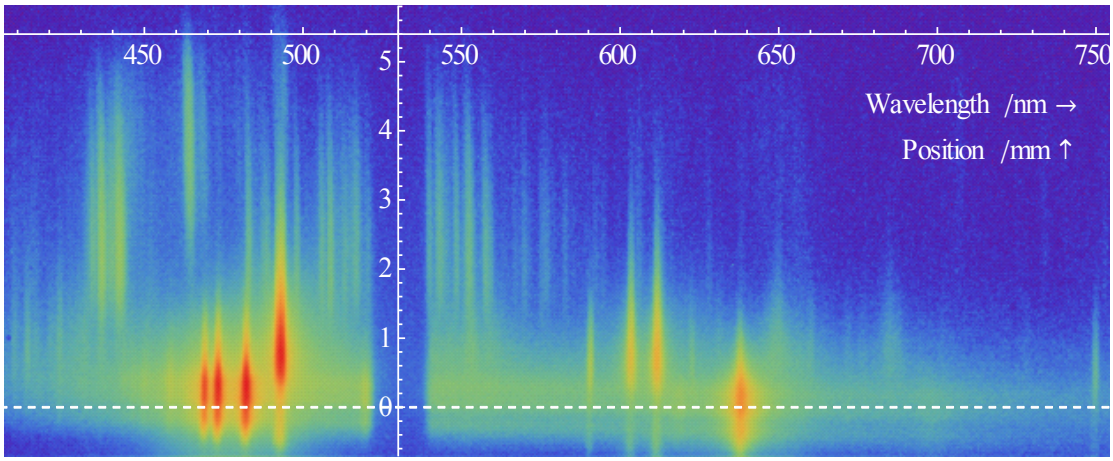

Figure 3.41: Spatiospectral image recorded at $t_g = t_0 + 80$ ns subsequent to the 532 nm ablation of Zn *in vacuo* with irradiance $I = 5.61$ GW/cm^2.

(Zn^0)*

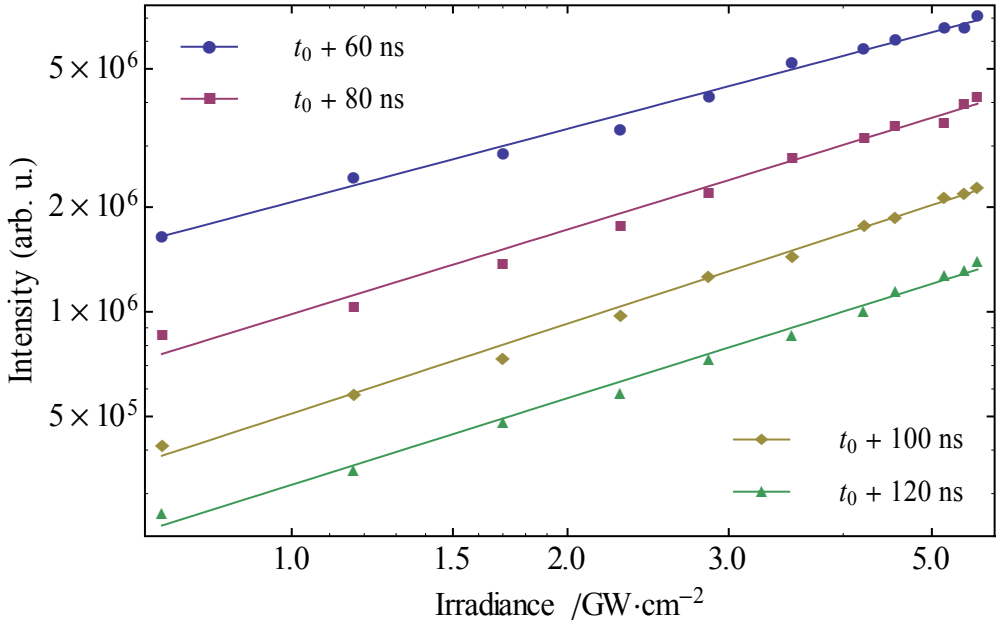

Figure 3.42: Variation with laser irradiance of the optical emission yield of (Zn^0)*, as produced in the 532 nm ablation of Zn *in vacuo*. The overlaid lines correspond to fitted power laws per Equation 3.2.

The power law exponents characterizing the (Zn^0)* optical emission yield subsequent to 532 nm ablation are comparable to those reported for irradiance below 3.7 GW/cm^2 in the 355 nm case, taking values of ≈ 0.7–0.8. In contrast to the previous situation,

though, no threshold is apparent above which different scaling behaviour applies, and a single power law accounts for the observed trend over the entire irradiance range investigated. It is not known, given the presently available data, whether a threshold would be observed at higher irradiance, but since phase explosion is not expected to exhibit significant wavelength dependence, we tentatively ascribe equivalent behaviour for ablation at 355 and 532 nm based on the similar power law exponents at low irradiance.

Table 3.26: Fitted scale and exponent (per Equation 3.2) for each of the trends indicated in Figure 3.3, corresponding to the dependence of the optical emission yield of $(Zn^0)^*$ on the irradiance at 532 nm for the ablation of Zn *in vacuo*.

t_g	$0.72 \leq I \leq 5.61$ GW/cm^2	
	Scale A	Exponent n
t_0 + 60 ns	14.543(23)	0.698(20)
t_0 + 80 ns	13.800(40)	0.808(32)
t_0 + 100 ns	13.142(24)	0.858(19)
t_0 + 120 ns	12.670(30)	0.827(24)

It is worth reiterating that Equation 3.2 relies upon the assumption that ablation and optical emission occur at arbitrarily small irradiance, which clearly cannot hold in view of the finite heat capacity and atomization enthalpy of Zn (especially if phase explosion is responsible for ablation at low incident power density, as this mechanism does not necessarily result in plasma formation). Nevertheless, it was not possible to obtain a meaningful formation threshold for $(Zn^0)^*$ at 532 nm from fits to Equation 3.4–Equation 3.6 due to the lack of discernible curvature in the trends presented in Figure 3.42.

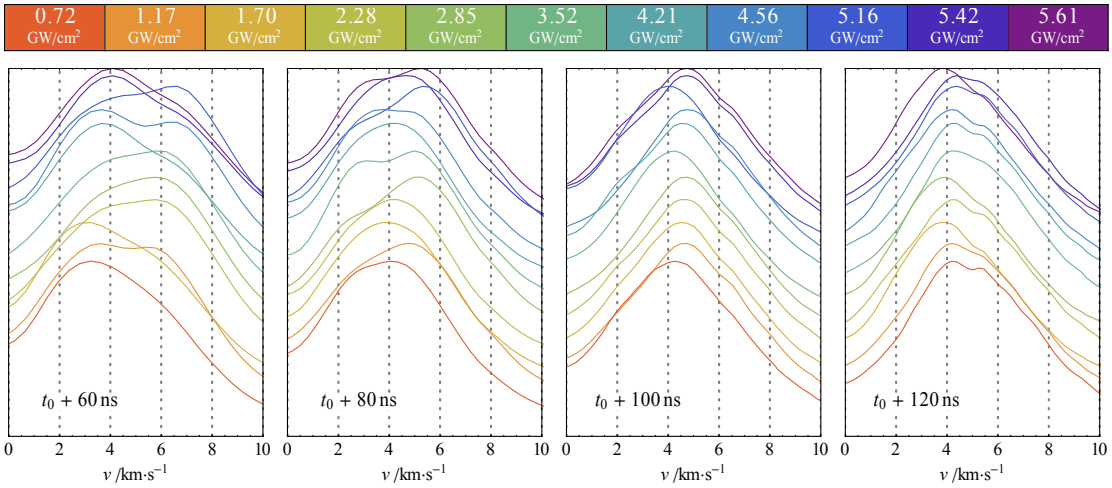

Figure 3.43: Spatial distribution of $(Zn^0)^*$ optical emission resulting from the 532 nm ablation of Zn *in vacuo*.

A further issue with the present data is the inaccuracy of the spatial profiles, which arises from the poor manufacturing tolerances of the target holder employed in the initial experiments: the axis of rotation deviated slightly from parallelism with the target surface normal, resulting in a periodic displacement (by 50–100 μm) of the point of origin. Although the faulty component was subsequently remanufactured to better tolerances, and the problem thereby eliminated, the distortion remains where there was insufficient time to repeat the experiments affected. The error incurred is relatively greatest for those species with the smallest displacements (thus lowest velocities), and amounts to several km/s. For Zn^0, it presents some difficulty in the interpretation of the results given that an error of this magnitude is comparable to the modal velocity of this species, although the velocity of $(Zn^0)^*$ resulting from ablation at 532 nm appears somewhat greater than that recorded subsequent to 355 nm irradiation. If the expansion of this species is predominantly thermally driven (as one might infer from the quasi-Maxwellian shape of the more accurate profiles obtained at 355 nm), such an observation is consistent with stronger heating of the nascent plasma given the λ^m dependence of the IBA cross-section (where $m = 2$–4 depending on the particular model, as discussed earlier). At any rate, such an argument cannot be viewed as definitive when considering the limited data on which it is based.

$(Zn^{1+})^*$

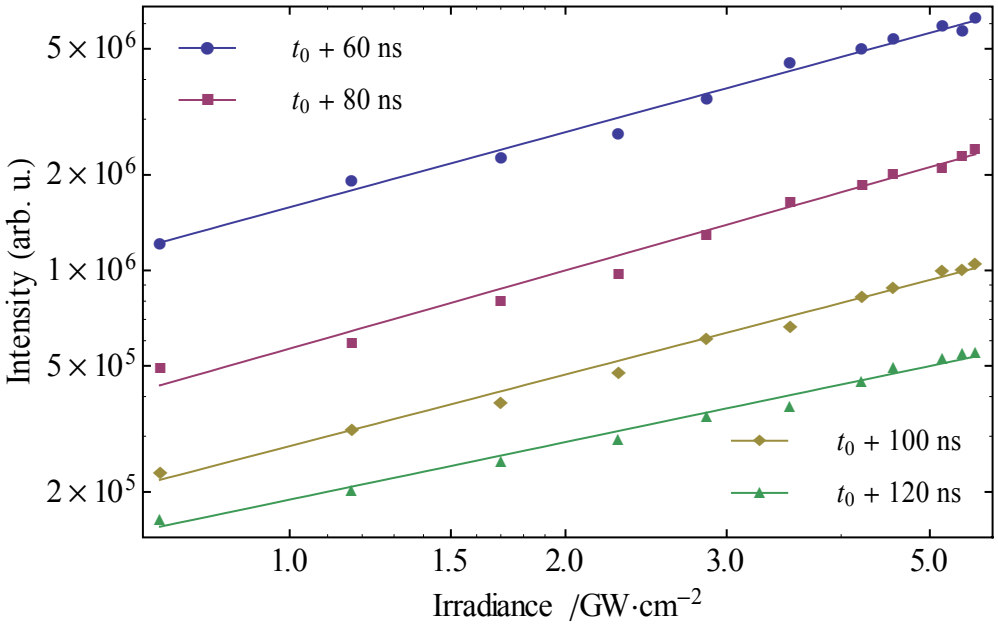

Figure 3.44: Variation of the optical emission yield of $(Zn^{1+})^*$ with laser irradiance, as recorded subsequent to the ablation of Zn *in vacuo* at 532 nm. The overlaid lines correspond to power laws per Equation 3.2.

Unlike $(Zn^0)^*$, the optical emission yield of $(Zn^{1+})^*$ exhibits substantially different irradiance scaling behaviour for 532 nm ablation in comparison to the situation at 355 nm, with the fitted power law exponents (Table 3.27) being smaller (≈ 0.8 vs. ≈ 1.0) at all time-gates. Additionally, there does not appear to be any threshold above which the rate of scaling is reduced, although (as in the previous section) it remains possible that such an observation would be made if the data were extended to higher irradiance. The dissimilar scaling behaviour of the ion yield relative to that of the neutral atom under a change of ablation wavelength is suggestive of a formation mechanism for this species whose efficiency scales with photon energy and is not readily saturated. Of the likely processes, such properties are most prominently exhibited by photoionization or multiphoton ionization, while it is known (from the presence of the associated emission lines) that there exist Zn atoms with energies near their ionization limit. The upper states of any of the observed $(Zn^0)^*$ transitions could be ionized by the absorption of one photon at either wavelength, whereas the lower states would require two 355 nm photons or either two or three photons at 532 nm. However, while such processes are quite likely to occur, they cannot directly be invoked to explain the discrepancy in the $(Zn^{1+})^*$ yields, because the upper states

involved in determining this are a further 14 eV above the Zn^{1+} ground state. The difference between having absorbed two or three photons in the ionization step is therefore probably insignificant.

Table 3.27: Fitted scale and exponent (according to Equation 3.2) for each of the trends indicated in Figure 3.44, corresponding to the dependence of the optical emission yield of $(Zn^{1+})^*$ on the irradiance at 532 nm for the ablation of Zn *in vacuo*.

t_g	$0.72 \leq I \leq 5.61$ GW/cm^2	
	Scale A	Exponent n
t_0 + 60 ns	14.275(31)	0.787(25)
t_0 + 80 ns	13.248(44)	0.819(35)
t_0 + 100 ns	12.539(26)	0.750(22)
t_0 + 120 ns	12.151(23)	0.603(21)

Other possibilities (which appear more likely in view of the arguments previously given for the dominance of inverse bremsstrahlung absorption) are that either the reflectivity of liquid Zn is greater in the visible than in the UV, or the photoelectron quantum yield and/or kinetic energy is reduced at the longer wavelength. It is difficult to draw conclusions with respect to the first of these since (as stated earlier) the high-temperature reflectance of Zn has apparently not been characterized. Nonetheless, the second proposition can be ruled out, since the work function of Zn (3.63 eV) is greater than the photon energy at either wavelength, so that thermionic emission will dominate. Moreover, if this were not the case, the photoelectron kinetic energy would be greater at 355 nm, so that it becomes difficult to rationalize the greater modal $(Zn^{1+})^*$ velocity observed presently (cf. Figure 3.45). However, even if reflectivity does not vary significantly from 355 to 532 nm, the optical penetration depth, which goes as the square root of wavelength, is a factor of 1.22 greater in the visible, and the volume over which incident radiation is distributed is correspondingly larger. The resulting diffuse heating implies that irradiation must continue for longer[u] before the surface approaches the critical temperature; but, during this time, a greater number of thermoelectrons will have been emitted, and the latter will have been heated much more strongly by IBA than at the shorter wavelength. Therefore, although plume formation at 355 nm is less subject to dissipative processes that result in a less

[u] Since the thermal diffusion rate is significant for metals under nanosecond-pulsed irradiation, the actual discrepancy is likely to be somewhat larger than the difference in the optical penetration depths suggests.

efficient utilization of laser energy, the surface field gradient is greater in the 532 nm case when phase explosion does occur.

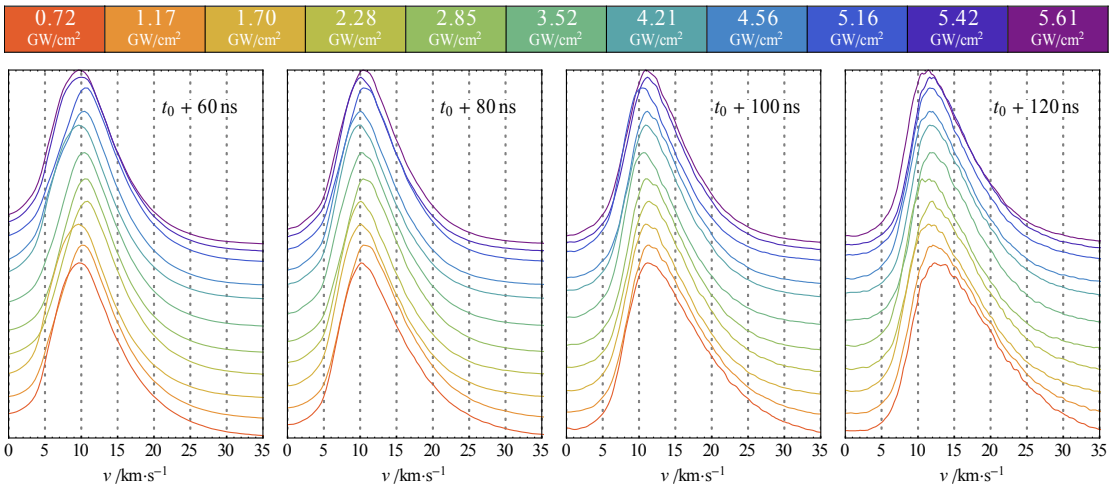

Figure 3.45: Spatial distribution of $(Zn^{1+})^*$ optical emission resulting from the ablation of Zn at 532 nm *in vacuo*.

$(Zn^{2+})^*$

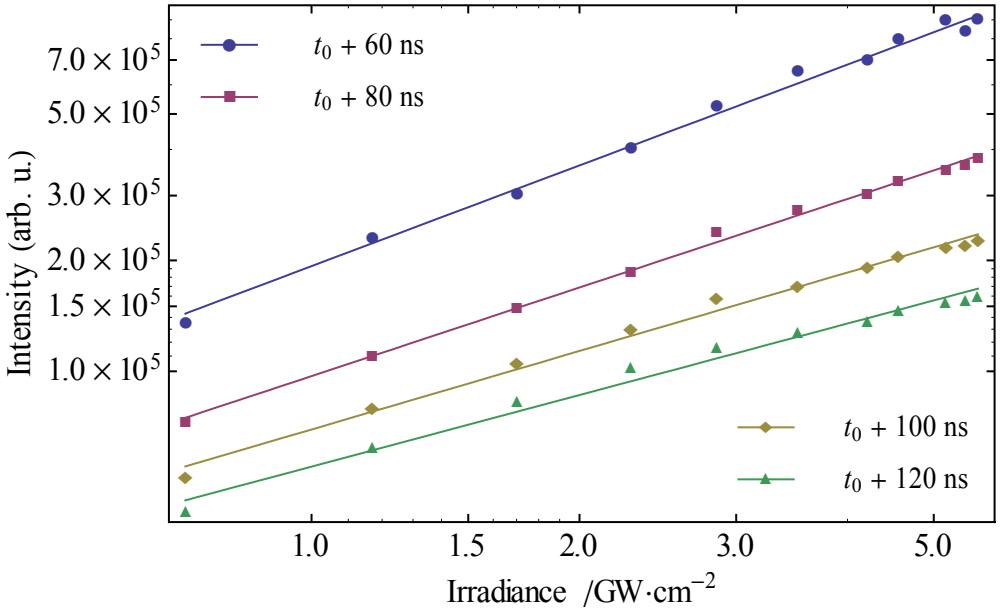

Figure 3.46: Variation with laser irradiance of the optical emission yield of $(Zn^{2+})^*$, as produced in the 532 nm ablation of Zn *in vacuo*. The overlaid line segments correspond to power laws per Equation 3.2.

Although perhaps not immediately clear due to the manner in which the data are presented here, it should be noted that the intensity of $(Zn^{2+})^*$ emission under 532 nm irradiation relative to that of $(Zn^{0})^*$ or $(Zn^{1+})^*$ is substantially greater than the

corresponding quantity at 355 nm. Indeed, from the fitted power laws, we find that the $(Zn^{2+})^*/(Zn^{1+})^*$ intensity ratio at 532 nm is approximately three to four times as large (depending on irradiance) as that at 355 nm. While this is as expected due to the stronger inverse bremsstrahlung absorption applicable in the visible region, knowledge of the relative quantities is important when considering the following results.

Table 3.28: Fitted scale and exponent (according to Equation 3.2) for each of the trends indicated in Figure 3.46, corresponding to the dependence of the optical emission yield of $(Zn^{2+})^*$ on the irradiance at 532 nm for the ablation of Zn *in vacuo*.

t_g	$0.72 \leq I \leq 5.61$ GW/cm^2	
	Scale A	Exponent n
t_0 + 60 ns	12.170(33)	0.909(25)
t_0 + 80 ns	11.483(16)	0.799(13)
t_0 + 100 ns	11.149(24)	0.708(20)
t_0 + 120 ns	10.917(28)	0.645(25)

The power law exponents are consistently smaller for than was seen previously in §3.3.1, which can be understood in terms of the same mechanism that was invoked to explain this effect for $(Zn^{1+})^*$. Due to the consistent observation of space charge–mediated dynamic acceleration, which requires an expanding plume, we suppose that $(Zn^{2+})^*$ is produced only in the hot dense plasma that is the result of field-assisted phase explosion. However, the maximum achievable $(Zn^{2+})^*$ population is strictly limited according to the duration for which irradiation continues after phase explosion occurs, the latter being delayed because of the more diffuse target heating mechanism operating at 532 nm. Since the laser pulses employed in the present work became shorter with increasing irradiance, it is easy to see that the $(Zn^{2+})^*$ yield must scale sub-linearly with the applied power density. Nonetheless, since the degree of dynamic acceleration possible *in vacuo* depends principally on the plasma temperature (which is constrained to be similar at both wavelengths given that phase explosion occurs spontaneously after a certain temperature is reached), it is similarly unsurprising that the velocity distributions do not differ significantly from those observed at 355 nm.

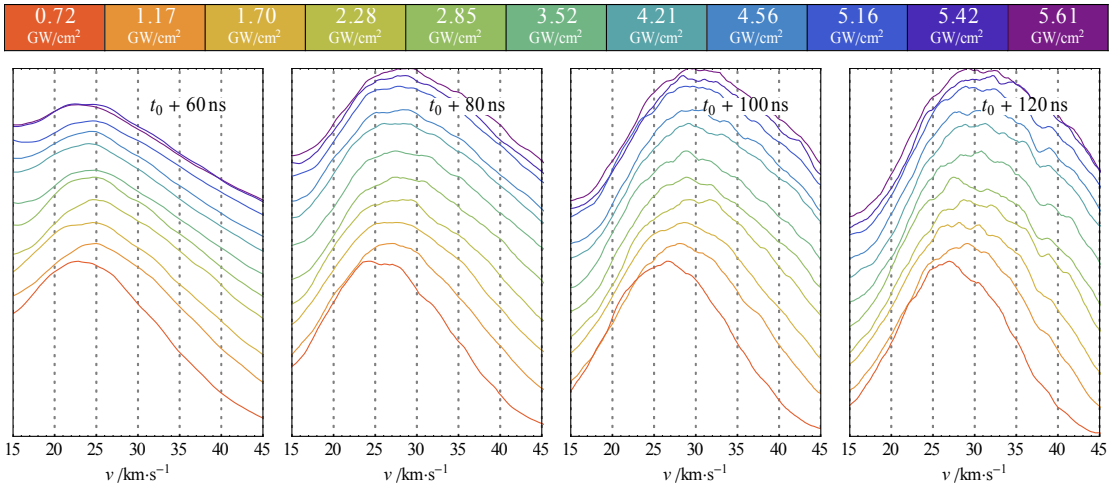

Figure 3.47: Spatial distribution of $(Zn^{2+})^*$ optical emission resulting from the 532 nm ablation of Zn *in vacuo*.

3.4.2 UNDER 50 MTORR O_2

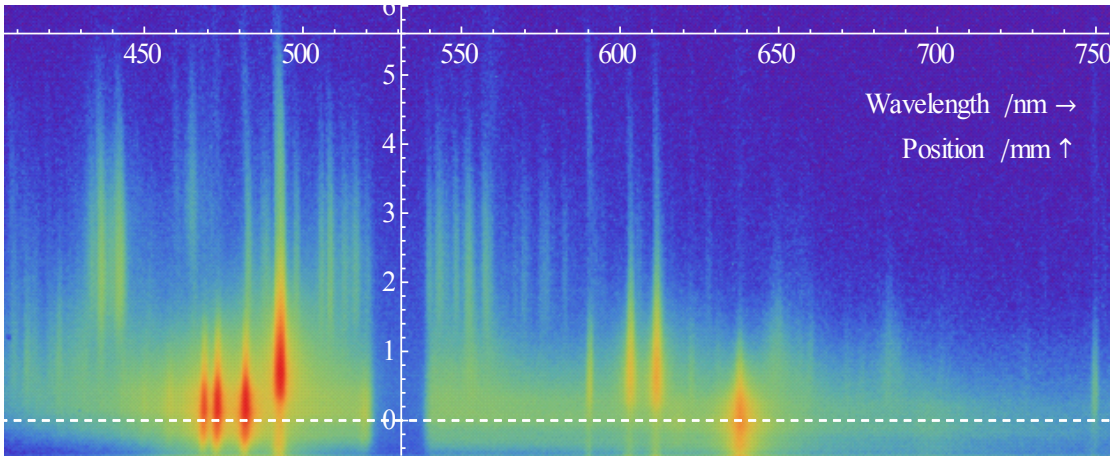

Figure 3.48: Spatiospectral image taken at $t_g = t_0 + 80$ ns subsequent to the 532 nm ablation of Zn under oxygen with $p(O_2) = 50$ mTorr and $I = 5.58$ GW/cm^2.

$(Zn^0)^*$

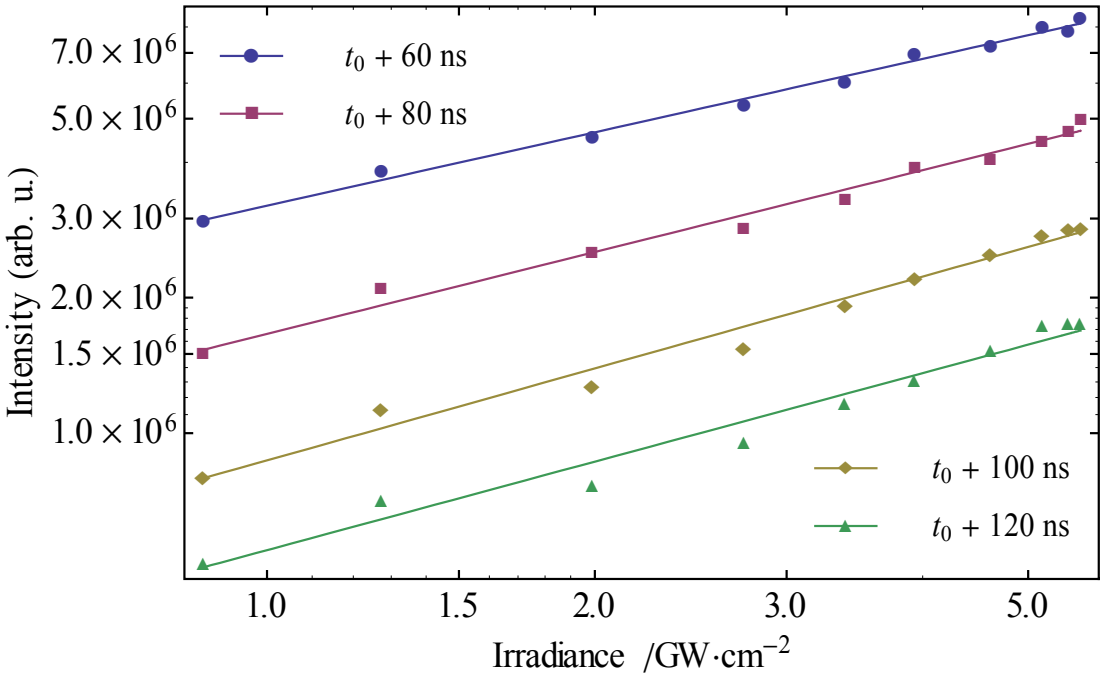

Figure 3.49: Variation with laser irradiance of the optical emission yield of $(Zn^0)^*$, as produced in the 532 nm ablation of Zn under oxygen with $p(O_2) = 50$ mTorr. The overlaid lines correspond to fitted power laws per Equation 3.2.

Although the influence of oxygen on $(Zn^0)^*$ yield is seemingly negligible for 355 nm ablation, the same does not appear to be true at 532 nm, with significantly lower power law exponents being recorded in the presence of the backing gas than *in vacuo* at all time-gates. Given that the primary mechanism of Zn^0 production appears to be phase explosion, we expect failure to reach the critical temperature of Zn to result in a reduced volume of ablated material owing to much slower normal evaporation, with a greater proportion of the laser energy being lost through heat conduction away from the irradiated area. Gragossian *et al.*[22] have studied the transition from evaporation to phase explosion in detail for Al and predicted a theoretical irradiance threshold of 1.22 GW/cm^2, while the present author has observed the same experimentally for Al at a slightly higher value of 1.86(9) GW/cm^2 at 532 nm. These values correspond reasonably closely, particularly when considering that their model assumed purely one-dimensional thermal conduction (directly into the target bulk) whereas clearly in reality some heat may also diffuse laterally. As already discussed, the onset of phase explosion seems likely to occur at lower irradiance for Zn than for Al, such that it is difficult to determine a threshold experimentally in the former case, but we may still

draw parallels with the better-characterized Al results in order to arrive at a qualitative explanation of the present observations. *In vacuo*, the fitted power law exponents for $(Al^0)^*$ are 0.29(4) below the phase explosion threshold and 0.61(3) above it; no similar situation (in the sense of a threshold signifying an *increase* in the exponent, characteristic of the onset of phase explosion) is encountered for Zn within the experimentally accessible irradiance range. Importantly, the introduction of oxygen during the ablation of Al leads to the disappearance of the threshold, producing instead a somewhat erratic trend with average exponent 0.46(2) (i.e., almost exactly intermediate between those attributed to vaporization and phase explosion) for $p(O_2) = 50$ mTorr.[v] Such behaviour is comparable to that of $(Zn^0)^*$ in the present case, with a substantial reduction in the fitted power law exponents under oxygen in relation to those obtained *in vacuo*; the mean values are 0.80(7) and 0.62(6), respectively, and the average difference is 0.18(2).

Table 3.29: Fitted scale and exponent (per Equation 3.2) for each of the trends indicated in Figure 3.49, corresponding to the dependence of the optical emission yield of $(Zn^0)^*$ on the irradiance at 532 nm for the ablation of Zn under oxygen at 50 mTorr.

t_g	$0.87 \leq I \leq 5.58$ GW/cm^2	
	Scale A	Exponent n
t_0 + 60 ns	14.980(14)	0.542(13)
t_0 + 80 ns	14.324(23)	0.604(20)
t_0 + 100 ns	13.676(31)	0.679(26)
t_0 + 120 ns	13.217(37)	0.654(23)

The question obviously arises as to why such a difference might be observed for ablation at 532 nm but not at 355 nm. A possible explanation for this apparent discrepancy is that, as reported by Gamal and Omar,[52] the optical breakdown threshold of oxygen (for nanosecond laser pulses) is substantially lower at 266 and 532 nm than it is at either 355 or 1064 nm. The inverse bremsstrahlung absorption cross-section is also larger for the longer wavelength, which may be especially important if breakdown proceeds by avalanche ionization subsequent to initial

[v] It is interesting to note, however, that the $(Al^{1+})^*$ optical emission yields are almost unaffected by the presence or absence of oxygen; a single trend (i.e., without any apparent threshold) is observed, and the exponents (≈ 0.55) do not differ noticeably between the two cases. This may indicate the importance of plasma etching as a secondary desorption process, and this possibility should be taken into account when considering the effect of the background gas on $(Zn^{1+})^*$, as in the next section.

photoelectron emission from Zn,[w] and furthermore implies stronger attenuation of 532 nm radiation by the resulting oxygen plasma. As a result, a reduced quantity of energy may be absorbed (alternatively, given competing heat conduction into the bulk, absorbed too slowly) by the target, such that the critical temperature of Zn is achieved either not at all, or only within a smaller volume. Although the power law exponents for Zn are reduced (relative to ablation *in vacuo*) by a similar amount as for Al, the absolute values are still larger than those obtained below the phase explosion threshold for the latter material. If ablation in this regime is primarily due to normal evaporation, this may be justified by the higher density and lower thermal conductivity of Zn in relation to Al (58.8 vs. 117 W m^{-1} K^{-1} for the liquids), such that more material is present within the irradiated volume and heat losses into the bulk are lower.

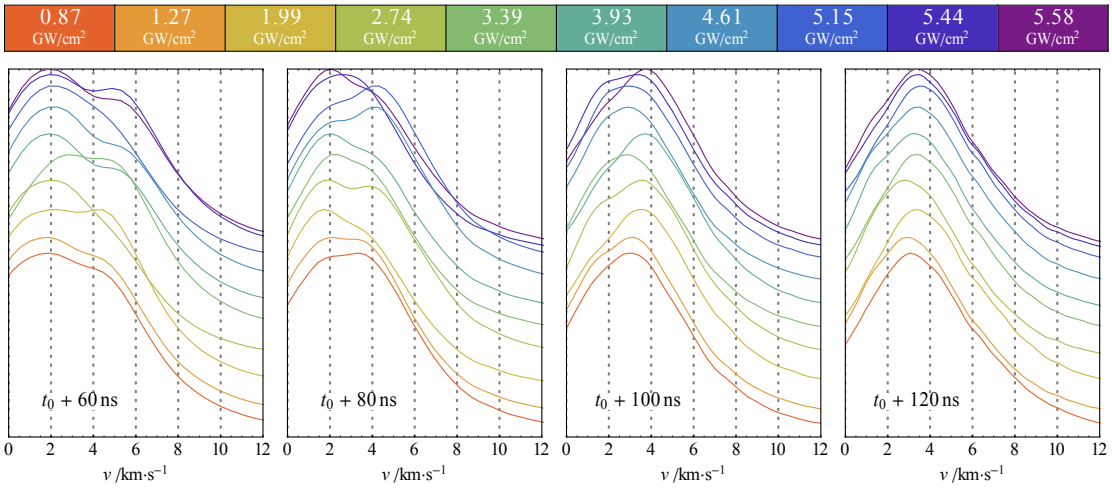

Figure 3.50: Spatial distribution of $(Zn^0)^*$ optical emission resulting from the 532 nm ablation of Zn with $p(O_2)$ = 50 mTorr.

[w] According to the previous authors, breakdown occurs by direct photoionization of O_2 at approximately 100 GW/cm^2. Although the figures quoted in this work are *mean* irradiance, such intensities are not likely to occur even as peak values in the present experiment. However, the quantities presented by Gamal and Omar were derived theoretically and are therefore likely to be more accurate in a relative than absolute sense, especially if initial ionization occurs *via* a different mechanism. This would not necessarily invalidate their kinetic model (and so the predicted wavelength-dependence), but may substantially reduce the effective breakdown threshold.

$(Zn^{1+})^*$

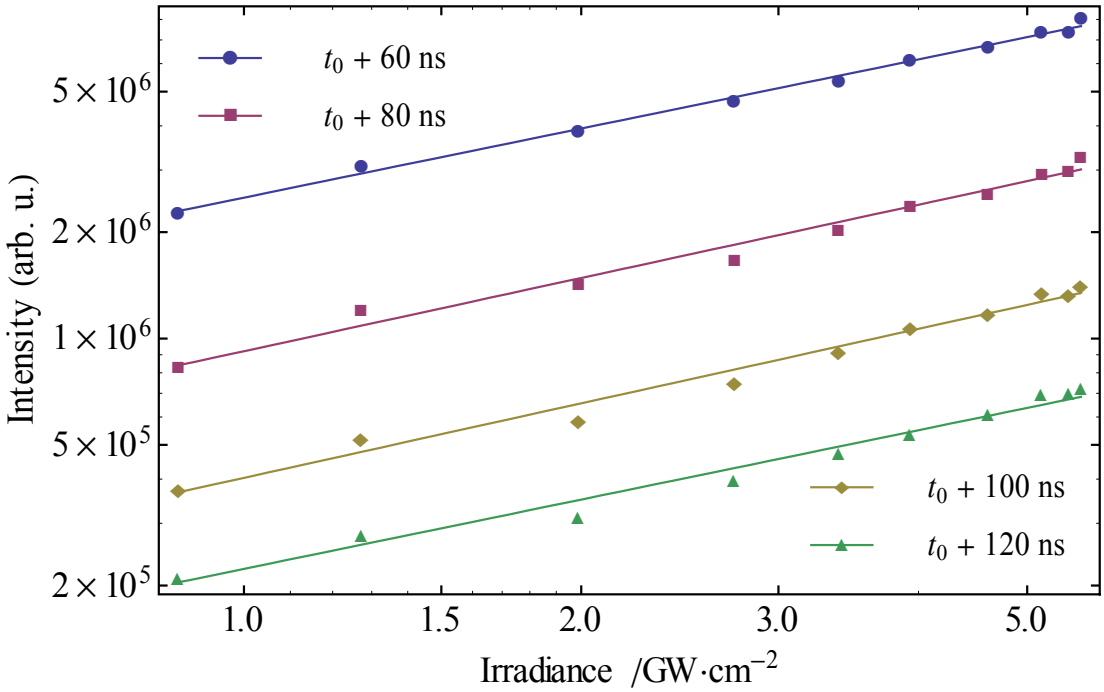

Figure 3.51: Variation with laser irradiance of the optical emission yield of $(Zn^{1+})^*$, as produced in the 532 nm ablation of Zn under oxygen with $p(O_2) = 50$ mTorr. The overlaid line segments correspond to power laws per Equation 3.2.

$(Zn^{1+})^*$ exhibits a response to the presence of oxygen similar to that of $(Zn^0)^*$, with the power law exponents being markedly decreased relative to their values *in vacuo*. Despite the prior argument that this may be due to an enhancement of the relative importance of normal evaporation, the velocity distributions are essentially unaffected by the ambient gas, remaining indicative of field-assisted phase explosion; indeed, as the modal velocities are practically unchanged, the strength of the surface field also does not appear to have been appreciably modified. Since the dynamics of plasma formation and plume evolution are apparently identical *in vacuo* and under oxygen, it seems likely that an irradiance-dependent proportion of the incident power is simply lost before reaching the target.

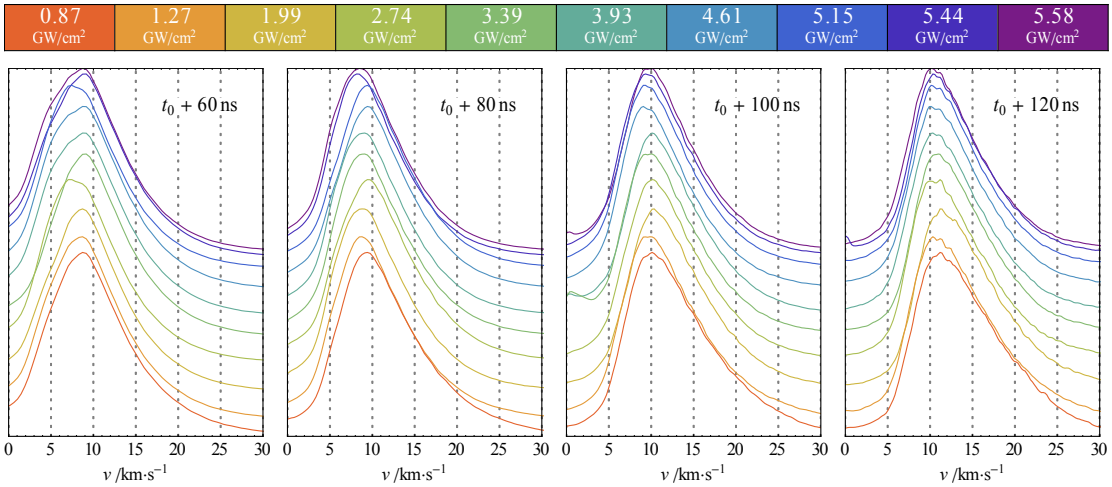

Figure 3.52: Spatial (velocity) distribution of $(Zn^{1+})^*$ optical emission resulting from the 532 nm ablation of Zn under $p(O_2)$ = 50 mTorr.

Given these observations, it is probable that (as suggested above) avalanche ionization of the backing gas results in plasma formation along the laser beam path some distance away from the target surface, thus absorbing and/or scattering radiation that would otherwise have contributed to the formation of excited-state Zn species. Since the avalanche multiplication factor directly depends on the electric field gradient, which itself varies with (the square root of) irradiance, it appears reasonable that the extent of the attenuation should scale with the latter, as seen here. Because this process does not qualitatively affect the Zn plasma plume, however, we refrain from further discussion here.

Table 3.30: Fitted scale and exponent (according to Equation 3.2) for each of the trends indicated in Figure 3.51, corresponding to the dependence of the optical emission yield of $(Zn^{1+})^*$ on irradiance for the ablation of Zn at 532 nm under $p(O_2)$ = 50 mTorr.

t_g	$0.87 \leq I \leq 5.58$ GW/cm²	
	Scale A	Exponent n
t_0 + 60 ns	14.734(15)	0.650(13)
t_0 + 80 ns	13.733(30)	0.689(26)
t_0 + 100 ns	12.908(33)	0.700(28)
t_0 + 120 ns	12.314(32)	0.652(28)

3.5 EFFECT OF INCREASED OXYGEN PRESSURE

Supplementary experiments were performed in which Zn was ablated at 532 nm with ambient oxygen pressure $p(O_2) > 50$ mTorr. A maximum $p(O_2) = 500$ mTorr was

chosen in order to avoid the onset of turbulent flow (as reported by Abdelli-Messaci *et al.*[53] in the ablation of ZnO with $p(O_2) \geq 750$ mTorr), which presents particular difficulties for a one-dimensional imaging experiment. Observations at pressures in the range $50 > p(O_2) > 100$ mTorr did not reveal substantial differences compared to the $p(O_2) = 50$ mTorr case, with the optical emission yields of Zn^{2+} and Zn^{3+} for a given irradiance simply being further suppressed relative to the experiments discussed in §3.4.2. However, for $p(O_2) \geq 100$ mTorr, a blast wave was observed to form resulting from the compression of the quasi-static background gas by the rapidly expanding ablation plasma, with the position of the shock front readily apparent due to substantial structured and continuum optical emission from the shocked gas (Figure 3.53).

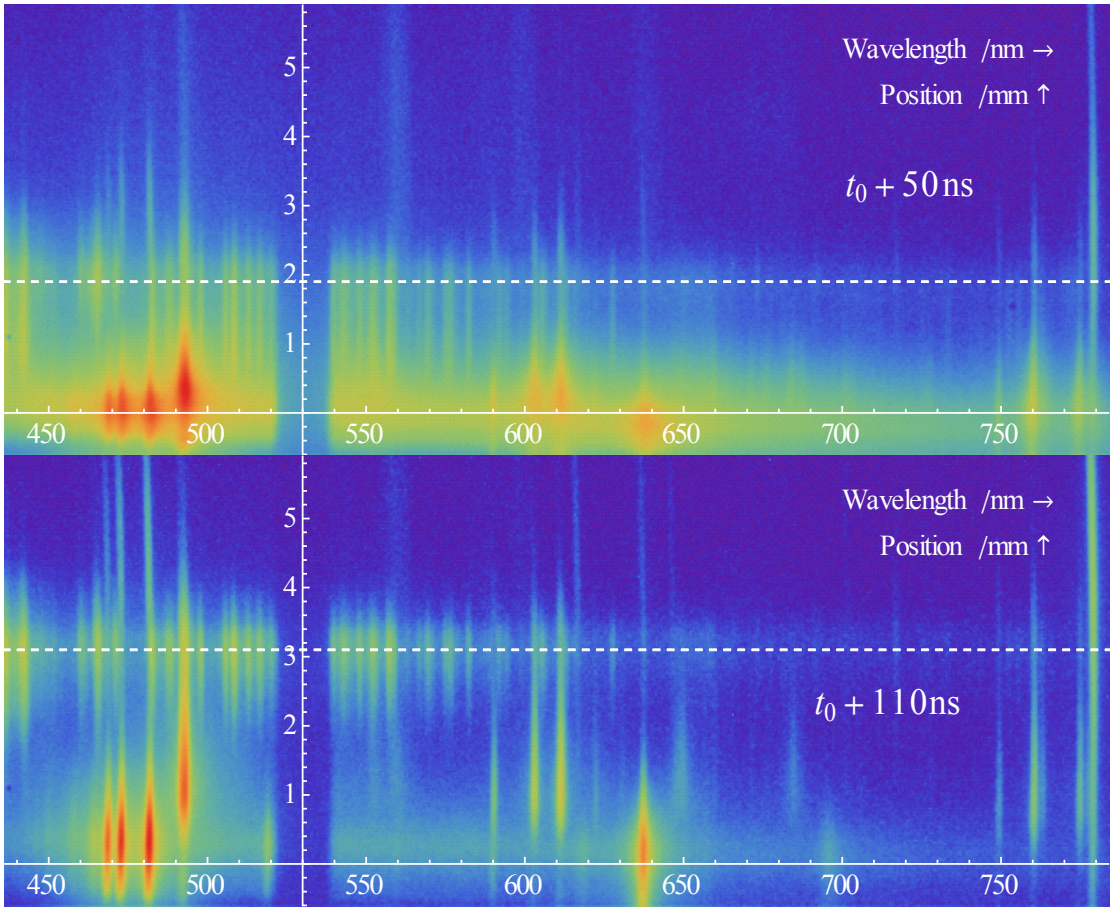

Figure 3.53: Images of Zn ablated under 500 mTorr O_2 taken at $t_g = t_0 + 50$ ns and $t_0 + 110$ ns after ablation with 532 nm radiation at an irradiance of ≈ 5.4 GW/cm^2 (≈ 49 J/cm^2). The position of the shock front is marked with a dashed line.

The molecular emission observed outside of the blast wave around 560 nm (Figure 3.54) can be identified from band-head positions as the overlapped $(v + 1, v)$

progression of the $b\ ^4\Sigma_g^- \rightarrow a\ ^4\Pi_u$ (first negative) system of O_2^+, with the weaker (v, v) and (v, $v + 1$) progressions being observed at ≈ 600 and ≈ 640 nm, respectively. A simulation constructed in Western's PGOPHER software,[54] employing molecular constants given by Albritton *et al.*[55] for the (1, 0) and (2, 1) bands, closely matches the experimental spectrum, thus confirming this assignment. Furthermore, the simulation indicates the rotational temperature of O_2^+ as 325±10 K, which is suggestive of electron (rather than ion) impact as the likely excitation mechanism due to evidently limited accompanying energy transfer to the background gas. The stronger (1, 0) band has been studied in this way by Terrell *et al.*,[56] who found an electron energy threshold of 18.2 eV, with the excitation cross section steeply rising to a maximum of 3.1×10^{-17} cm^2 at around 100 eV. In contrast, the cross section (at the same electron energy) for excitation of the 777 nm O^0 triplet emission is 4.3×10^{-18} cm^2 according to Itikawa *et al.*[57], yet the O^0 lines are observed with very much greater intensity and a notably different spatial distribution (cf. §3.5.1/§3.5.2) than the molecular emissions.

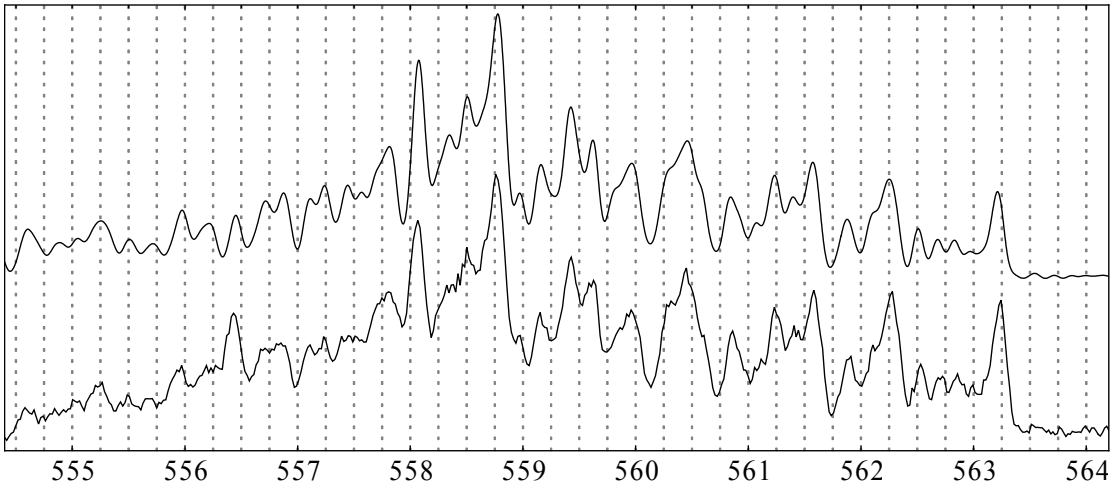

Figure 3.54: Spectrum of the ($v + 1$, v) progression of the $b\ ^4\Sigma_g^- \rightarrow a\ ^4\Pi_u$ system of O_2^+, observed outside of the blast wave and probably excited by electron impact ionization. The upper curve is the simulation, constructed in PGOPHER using constants given by Albritton *et al.*; the lower curve is the experimental spectrum.

In explaining this discrepancy, we note that Zn species are observed to penetrate a substantial distance into the background gas, with Zn^{1+} emission around 492 nm evident (albeit weakly) throughout the entire spatial extent of the image even at $t_g = t_0 + 50$ ns. Furthermore, the relative intensity of the Zn^0 468/472/481 nm triplet emission ahead of the shock front increases with time, and the spatial distribution of

this species is apparently similar to that of O^0. We therefore conclude that these observations are indicative of a recombinative "cascade" whereby highly energetic multiply charged Zn ions undergo repeated collisional electron capture in the presence of O_2. It is unclear, however, whether Zn^{3+} is the most highly charged ion produced in the present experiments, or indeed whether the partitioning of total energy between translational kinetic energy and electronic excitation is uniform in the known species, given that individual ions are not observed. Nevertheless, these putative highly energetic ions certainly cannot represent more than a small fraction of the ablation products due to the evidently limited momentum they impart to the gas ahead of the shock front.

Despite the identification by Chertihin and Andrews of the ZnO molecular product of Zn ablation under oxygen,[58] and Wicke's observation of broad-band visible ZnO chemiluminescence subsequent to the reaction of laser-ablated Zn with N_2O,[59] we find no evidence of ZnO molecular emission in the present experiments. However, this is unlikely to be indicative of the non-existence of this product, since the chemiluminescent reaction channel is thought by Wicke to represent a minor pathway, and the relatively high pressure in the interaction region probably also contributes to collisional quenching in the present case.[x] Furthermore, the ZnO molecule is only weakly bound, having dissociation energy $D_0 = 1.61$ eV according to Clemmer *et al.*,[60] while the corresponding ions are only slightly more stable, with $D_0(ZnO^+) = 1.67$ eV (Clemmer *et al.*) and $D_0(ZnO^-) = 2.24$ eV (Fancher *et al.*[61]), such that its stability is likely to be marginal in the highly energetic environment currently under consideration. Since these dissociation limits are apparently too small to support Wicke's report of chemiluminescence (requiring a bond energy of at least 2.8 eV), it is worth noting the more recent work of Boughdiri *et al.*, who re-considered inter-state correlation to arrive at a new dissociation limit 3.59 eV above the $^1\Sigma^+$ ground state.[62]

[x] The collision frequency in oxygen at 325 K and 500 mTorr is 5.9×10^6 s^{-1}, which is too small for significant quenching to occur over the timescale of the experiment. However, it is likely to be much higher at the interface between the expanding plasma and the background gas due to compression and heating of the ambient medium by the impact of energetic ablation products (see following sections).

3.5.1 VARYING PRESSURE; CONSTANT IRRADIANCE

Oxygen pressure was varied between 0 and 500 mTorr while maintaining a fixed irradiance of ≈ 5.4 GW/cm^2 (fluence ≈ 49 J/cm^2). Figure 3.55 shows the variation with pressure of the optical emission spatial profiles for $(Zn^{2+})^*$ and $(Zn^{3+})^*$, these being the species for which emission at the shock front was most strongly differentiated from that otherwise occurring in the ablation plume. Due to its origin as a dynamical, collective phenomenon, the position at which the shock wave initially forms is not entirely clear; indeed, the concept of a well-defined origin may not be particularly physically meaningful in this case. The velocities indicated in Figure 3.55 are, therefore, the result of placing the origin at the target surface, and as such indicate not the propagation velocity of the blast wave itself but rather that of ablated material as it reaches the shock front.

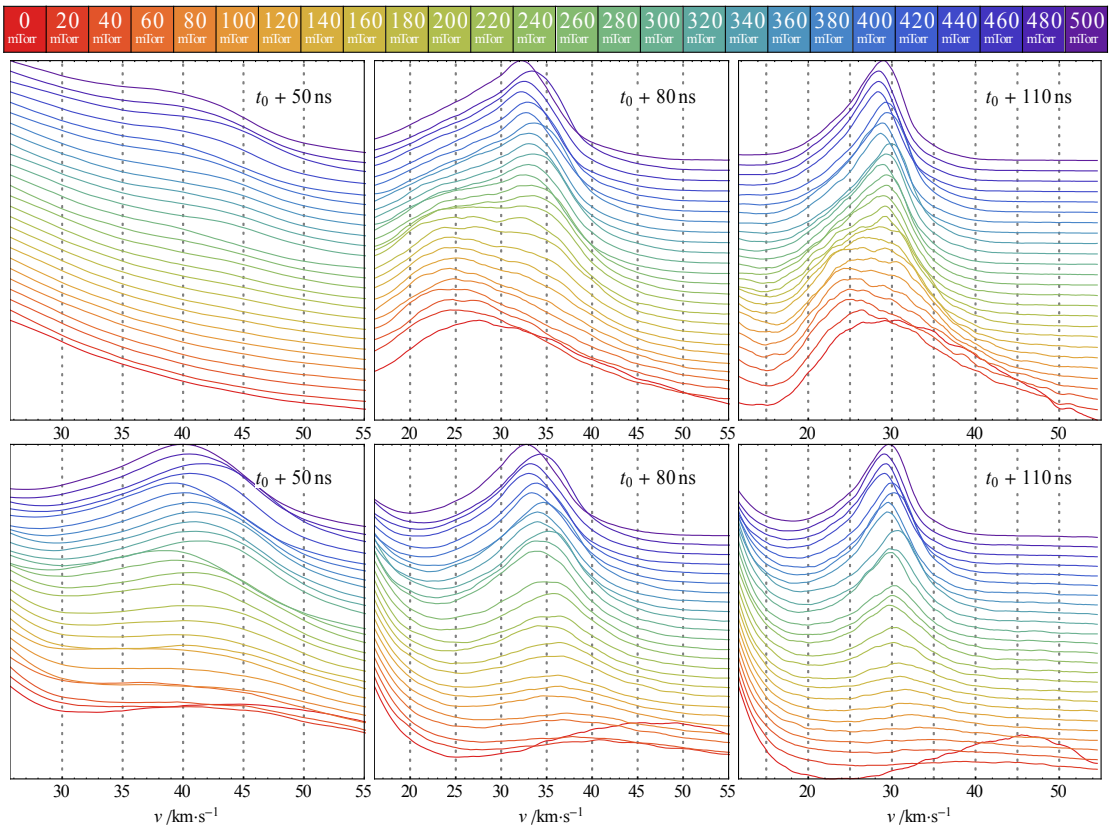

Figure 3.55: Velocity-space profiles for $(Zn^{2+})^*$ (above) and $(Zn^{3+})^*$ (below) emissions from the ablation of Zn under oxygen at various pressures.

It is clear from Figure 3.55 that momentum is transferred from the ablation plume to the background gas in the process of blast wave formation, with the fastest species contributing to the early compression of the ambient medium and the resulting shock

front propagating with an average velocity that is insufficient to prevent the impact of further energetic material. Figure 3.56 shows the absolute displacement of the shock at various times, demonstrating its approximately constant velocity of ≈ 20 km/s over the time interval $t = t_0 + 50$–80 ns. Additionally, enhanced $(O^0)^*$ emission can be observed just beyond that owing to $(Zn^{3+})^*$, the former most likely being formed by the impact of, or charge-transfer reactions with, highly charged Zn ions, as discussed above. However, it is not clear whether the enhancement ahead of the apparent position of the shock front is the result of further such processes occurring within the shocked gas, or merely indicative of the collisional excitation of oxygen atoms already present.

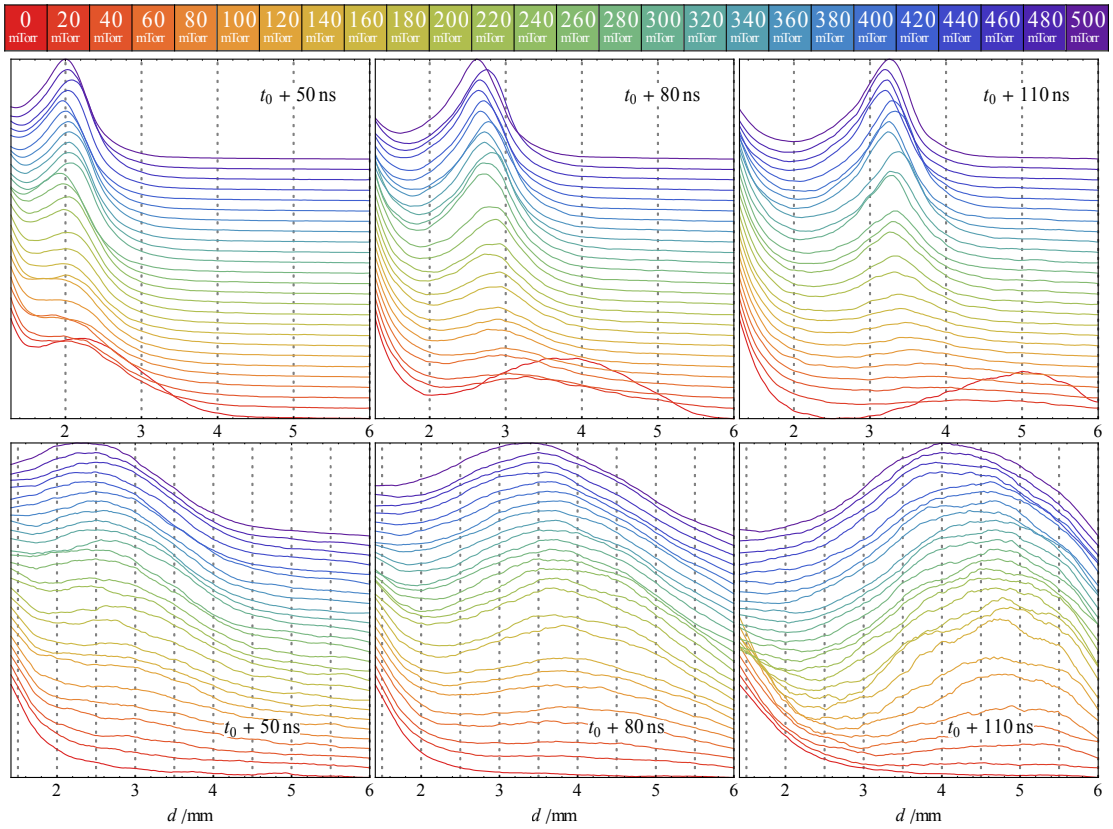

Figure 3.56: Position-space profiles for $(Zn^{3+})^*$ (above) and $(O^0)^*$ (below) emissions from the ablation of Zn under oxygen at various pressures.

The constancy of the blast wave velocity, despite varying pressure, is also readily apparent in Figure 3.55 and Figure 3.56. While this observation is consistent with the weak dependence on pressure of all relevant parameters as suggested by Chen *et al.*,[39] it is perhaps surprisingly so given that their model is stated to be valid only in the first 40 ns (due to Rayleigh-Taylor instability and three-body recombination) and

relies on the non-reactivity of the background gas. While the present experiments were deliberately conducted at a pressure low enough to avoid Rayleigh-Taylor instability, we nonetheless conclude that the effect of the other processes exerts a relatively minor influence on overall dynamics for the ablation of Zn under O_2.

3.5.2 VARYING IRRADIANCE; CONSTANT PRESSURE

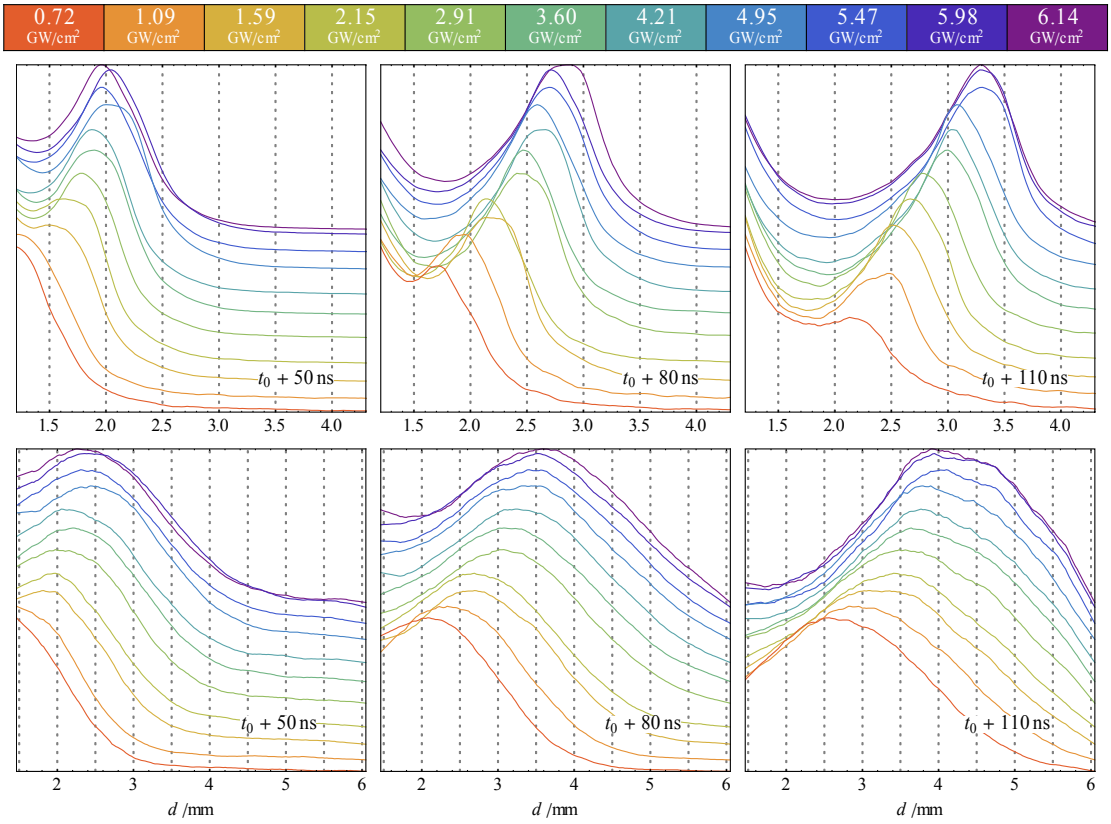

Figure 3.57: Position-space profiles for $(Zn^{3+})^*$ (above) and $(O^0)^*$ (below) emissions from the ablation of Zn at $p(O_2)$ = 500 mTorr with varying irradiance.

The effect of varying irradiance is demonstrated in Figure 3.57. While the influence of this parameter was not investigated by Chen *et al.*, Reddy[63] has shown that an interpretation in terms of the Sedov-Taylor solution for an infinitely strong spherically symmetric explosion holds acceptably well, although laser-produced shocks are in general not spherically symmetric due to the presence of the target. The radius R of the shock front according to this model is given by

$$R = \left(\frac{E}{\rho_0} \right)^{1/5} t^{2/5} \qquad \text{Equation 3.14}$$

where E is a function of the deposited energy E_0 (with $E = 1.175\,E_0$ for diatomic gases), and ρ_0 is the density of the surrounding medium, which is equal to 8.75×10^{-4} kg/m^3 for oxygen at $p = 500$ mTorr and $T = 20$°C. From Equation 3.14 and the pulse energies given in Table 3.31, we may calculate the expected radius at any given time. These values are shown as vertical lines in Figure 3.58 alongside the measured spatial profiles of $(Zn^{2+})^*$ at $t_g = t_0 + 110$ ns.

Table 3.31: Correspondence between irradiance, FWHM pulse duration, fluence, and pulse energy for the experiments in which Zn was ablated at $p(O_2) = 500$ mTorr.

Irradiance /GW·cm^{-2}	FWHM duration /ns	Fluence /J·cm^{-2}	Pulse energy /mJ
6.14(26)	8.69(35)	53.3(7)	32.8(4)
5.98(33)	8.73(37)	52.3(1.7)	32.1(1.1)
5.47(21)	8.89(32)	48.6(6)	29.9(3)
4.95(18)	9.08(31)	44.9(6)	27.6(4)
4.21(14)	9.39(26)	39.5(7)	24.3(4)
3.60(16)	9.71(40)	34.9(4)	21.5(3)
2.91(11)	10.17(34)	29.6(4)	18.2(2)
2.15(7)	10.89(34)	23.4(3)	14.4(2)
1.59(6)	11.68(43)	18.6(2)	11.4(1)
1.09(5)	12.81(48)	14.0(2)	8.6(1)
0.72(4)	14.21(60)	10.3(3)	6.3(2)

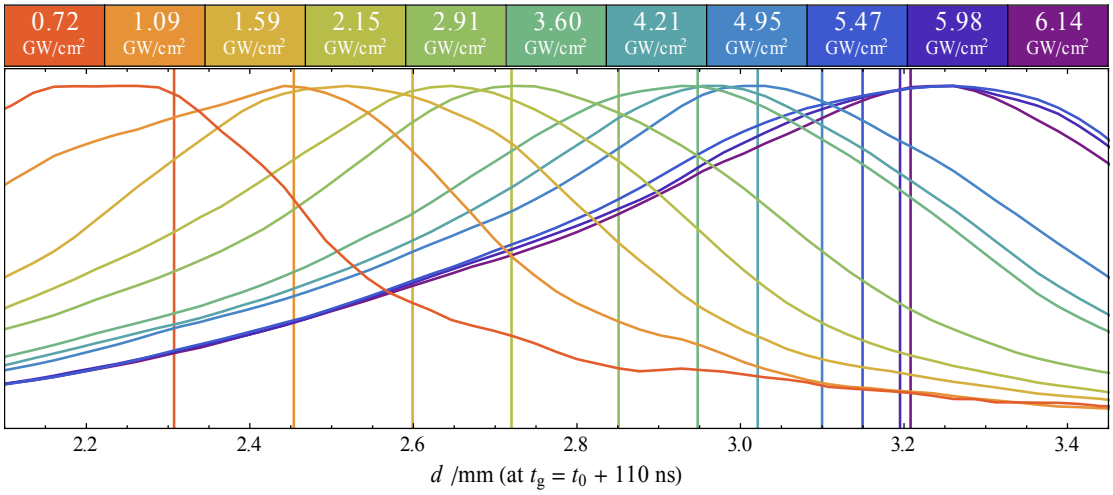

Figure 3.58: Comparison of the blast wave radius, as assessed by the $(Zn^{2+})^*$ optical emission spatial profiles, with the calculated values according to the Sedov-Taylor solution (vertical lines) for $t_g = t_0 + 110$ ns.

Despite the hemispherical blast wave geometry, finite background gas pressure, and non-instantaneous energy deposition, all of which may suggest the limited applicability of the Sedov-Taylor model to the present scenario, the predicted shock front radius is in reasonable agreement with the position of maximum of optical

emission intensity. By scaling the values of E for best fit, we find that approximately ⅔ of the laser pulse energy is absorbed by the plasma, which is somewhat greater than the value of around ½ predicted by Chen *et al.* for a 266 nm laser. This is likely due to greater inverse bremsstrahlung absorption at the longer wavelength, although Bogaerts and Chen[31] have shown that the absorption fraction also scales with irradiance, so that the use of a more involved model would be preferable in order to properly account for this effect. Furthermore, it is worth noting that all $(Zn^0)^*$ emission not assignable as the result of electron-ion recombination occurs inside the shock front, so it would appear that few neutral Zn atoms actually encounter the ambient environment. As such, the momentum carried by this species is not accounted for in the foregoing analysis, despite that the common thermal origin of the neutrals and singly positively charged ions implies that the former are more abundant. Although the absorption fraction of ⅔ is therefore an underestimate, we may nonetheless conclude that, given the much higher formation energies and hence relatively small populations of the higher ions, the majority of the total momentum is likely to be carried by Zn^{1+}.

3.6 REFERENCES

[1] "Accurately Measured Wavelengths of Zn I and Zn II Lines of Astrophysical Interest", D. Gullberg and U. Litzén, *Phys. Scr.* **61**, 652 (2000). DOI: 10.1238/physica.regular.061a00652.

[2] "Extensions to the spark spectra of zinc. I. Zinc II and zinc IV", A. M. Crooker and K. A. Dick, *Can. J. Phys.* **46** (10), 1241 (1968). DOI: 10.1139/p68-158.

[3] "The spark spectra of zinc. II. Zinc III", K. A. Dick, *Can. J. Phys.* **46** (11), 1291 (1968). DOI: 10.1139/p68-449.

[4] "A table of semiempirical *gf* values", R. L. Kurucz and E. Peytremann, *Smithsonian Astrophysical Observatory (SAO) Special Report #362* (1975). (a) *SAO/NASA Astrophysics Data System*, Harvard-Smithsonian Center for Astrophysics, Harvard University. Bibliographic code: 1975SAOSR.362.....K. (b) *VizieR Astronomical Catalogue Database*, Centre de Données Astronomiques, Université de Strasbourg. Catalogue number: VI/10.

[5] "Atomic spectral line list", R. Hirata and T. Horaguchi (1995).
(a) *VizieR Astronomical Catalogue Database*, Centre de Données Astronomiques, Université de Strasbourg. Catalogue number: VI/69.
(b) *Atomic Spectral Lines Database*, Laboratory for Quantum Optics, Korean Atomic Energy Research Institute. URL: http://amods.kaeri.re.kr/.

[6] "Energy Levels of Zinc, Zn I through Zn XXX", J. Sugar and A. Musgrove, *J. Phys. Chem. Ref. Data* **24** (6), 1803 (1995). DOI: 10.1063/1.555971.

[7] "Selected Tables of Atomic Spectra (Atomic Energy Levels and Multiplet Tables): O I", C. E. Moore (1976).
(a) *National Standard Reference Data Series*, United States National Bureau of Standards. Document reference: NSRDS 3, §7.
(b) *NIST Atomic Spectra Database*, United States National Institute of Standards and Technology. URL: http://physics.nist.gov/asd.

[8] "The spectrum of singly ionized oxygen, O II", I. Wenåker, *Phys. Scr.* **42** (6), 667 (1990). DOI: 10.1088/0031-8949/42/6/008.

[9] "A Compilation of Energy Levels and Wavelengths for the Spectrum of Singly–Ionized Oxygen (O II)", W. C. Martin, V. Kaufman, and A. Musgrove, *J. Phys. Chem. Ref. Data* **22** (5), 1179 (1993). DOI: 10.1063/1.555928.

[10] "Accurate wavelengths in O II", K. B. S. Eriksson, *J. Opt. Soc. Am. B* **4** (9), 1369 (1987). DOI: 10.1364/JOSAB.4.001369.

[11] "Electron density and temperature measurements in a laser produced carbon plasma", S. S. Harilal, C. V. Bindhu, R. C. Issac, V. P. N. Nampoori, and C. P. G. Vallabhan, *J. Appl. Phys.* **82** (5), 2140 (1997). DOI: 10.1063/1.366276.

[12] "Generalized multiphoton-ionization cross sections of the rare gases for 500-fs, 248.6-nm pulses", C. J. G. J. Uiterwaal, D. Xenakis, D. Charalambidis, P. Maragakis, H. Schröder, and P. Lambropoulos, *Phys. Rev. A* **57** (1), 392 (1998). DOI: 10.1103/PhysRevA.57.392.

[13] "Model for laser-induced thermal degradation and ablation of polymers", N. Arnold and N. Bityurin, *Appl. Phys. A* **68** (6), 615 (1999). DOI: 10.1007/s003390050950.

[14] "Smoothing and Differentiation of Data by Simplified Least Squares Procedures", A. Savitzky and M. J. E. Golay, *Anal. Chem.* **36** (8), 1627 (1968). DOI: 10.1021/ac60214a047.

[15] "Energies and quantities of ions in laser-produced metal plasmas", B. E. Paton and N. R. Isenor, *Can. J. Phys.* **46** (10), 1237 (1968). DOI: 10.1139/p68-157.

[16] "Ablation of solids by femtosecond lasers: Ablation mechanism and ablation thresholds for metals and dielectrics", E. G. Gamaly, A. V. Rode, B. Luther-Davies, and V. T. Tikhonchuk, *Phys. Plasmas* **9** (3), 949 (2002). DOI: 10.1063/1.1447555.

[17] "Space charge corrected electron emission from an aluminum surface under non-equilibrium conditions", W. Wendelen, B. Y. Mueller, D. Autrique, B. Rethfeld, and A. Bogaerts, *J. Appl. Phys.* **111** (11), 113110 (2012). DOI: 10.1063/1.4729071.

[18] "Space-charge–induced acceleration of ions emitted by laser-irradiated surfaces", A. J. Peurrung, J. P. Cowin, G. Teeter, S. E. Barlow, and T. M. Orlando, *J. Appl. Phys.* **78** (1), 481 (1995). DOI: 10.1063/1.360631.

[19] W. M. Haynes and D. R. Lide (eds.), *CRC Handbook of Chemistry and Physics*, 92nd ed. (CRC Press, 2011). ISBN: 978-1-4398-5511-9. URL (online edition): http://www.hbcpnetbase.com/.

[20] "Experimental determination of laser-induced breakdown thresholds of metals under nanosecond Q-switched laser operation", L. M. Cabalín and J. J. Laserna, *Spectrochim. Acta B* **53** (5), 723 (1998). DOI: 10.1016/S0584-8547(98)00107-4.

[21] "Optical Properties of Zn", L. P. Mosteller, Jr. and F. Wooten, *Phys. Rev.* **171** (3), 743 (1968). DOI: 10.1103/PhysRev.171.743.

[22] "Laser ablation of aluminum from normal evaporation to phase explosion", A. Gragossian, S. H. Tavassoli, and B. Shokri, *J. Appl. Phys.* **105** (10), 103304 (2009). DOI: 10.1063/1.3131689.

[23] "Observation of nanosecond laser-induced phase explosion in aluminum", C. Porneala and D. A. Willis, *Appl. Phys. Lett.* **89** (21), 211121 (2006). DOI: 10.1063/1.2393158.

[24] "High-Temperature, High-Pressure Thermophysical Measurements on Liquid Zinc", C. Otter, G. Pottlacher, and H. Jäger, *Int. J. Thermophys.* **17** (5), 987 (1996). DOI: 10.1007/BF01441988.

[25] "The Critical Temperature of Aluminum", V. Morel, A. Bultel, and B. G. Chéron, *Int. J. Thermophys.* **30** (6), 1853 (2009). DOI: 10.1007/s10765-009-0671-6.

[26] "Comparison of the laser ablation process on Zn and Ti using pulsed digital holographic interferometry", E. Amera, P. Grena, A. F. H. Kaplana, M. Sjödahla, and M. El Shaer, *Appl. Surf. Sci.* **256** (14), 4633 (2010). DOI: 10.1016/j.apsusc.2010.02.063.

[27] "Thermal Ionization", *Math. Phys. Anal. Geom.* **7** (3), 239 (2004). DOI: 10.1023/B:MPAG.0000034613.13746.8a.

[28] "The Saha–Langmuir Equation and its Application", M. J. Dresser, *J. Appl. Phys.* **39** (1), 338 (1968). DOI: 10.1063/1.1655755.

[29] K.-H. Spatschek, *High Temperature Plasmas*, 2nd ed. (Wiley-VCH Verlag, Berlin, 2011). ISBN: 978-3-52-763812-3.

[30] "Laser Photoionization Spectroscopy of the Zinc Atom and the Study of Zinc Sulfide Evaporation", O. Tukhlibaev and U. Zh. Alimov, *Opt. Spectrosc.* **88** (4), 506 (2000). DOI: 10.1134/1.626828.

[31] "Effect of laser parameters on laser ablation and laser-induced plasma formation: A numerical modelling investigation", A. Bogaerts and Z. Chen, *Spectrochim. Acta B* **60** (9–10), 1280 (2005). DOI: 10.1016/j.sab.2005.06.009.

[32] "Measurements of electron energy distribution in tantalum laser-generated plasma", L. Torrisi, D. Mascali, R. Miracoli, S. Gammino, N. Gambino, L. Giuffrida, and D. Margarone, *J. Appl. Phys.* **107** (12), 123303 (2010). DOI: 10.1063/1.3429242.

[33] "Cu^0, Cu^+, and Cu_2 from excimer-ablated copper", R. W. Dreyfus, *J. Appl. Phys* **69** (3), 1721 (1991). DOI: 10.1063/1.347218.

[34] "Parametric study of ion acceleration in a one-dimensional plasma expansion using the particle-in-cell simulation", T. Nedelea and H. Urbassek, *Phys. Rev. E* **69** (5), 056408 (2004). DOI: 10.1103/PhysRevE.69.056408.

[35] "High-order multiphoton ionization at metal surfaces by laser fields of moderate power", S. Varró and F. Ehlotzky, *Phys. Rev. A* **57** (1), 663 (1998). DOI: 10.1103/PhysRevA.57.663.

[36] "On the excitation mechanism of the He-Zn laser", L. A. Riseberg, and L. D. Schearer, *IEEE J. Quantum Electron.* **7** (1), 40 (1971). DOI: 10.1109/JQE.1971.1076546.

[37] "Cadmium Spectra", A. G. Shenstone and J. T. Pittenger, *J. Opt. Soc. Am.* **39** (3), 219 (1949). DOI: 10.1364/JOSA.39.000219.

[38] "Laser ablation of Cu and plume expansion into 1 atm ambient gas", Z. Chen and A. Bogaerts, *J. Appl. Phys.* **97** (6), 063305 (2005). DOI: 10.1063/1.1863419.

[39] "Effect of ambient pressure on laser ablation and plume expansion dynamics: A numerical simulation", Z. Chen, D. Bleiner, and A. Bogaerts, *J. Appl. Phys.* **99** (6), 063304 (2006). DOI: 10.1063/1.2182078.

[40] "Accelerated Expansion of Laser-Ablated Materials Near a Solid Surface", K. R. Chen, J. N. Lebœuf, R. F. Wood, D. B. Geohegan, J. M. Donato, C. L. Liu, and A. A. Puretzky, *Phys. Rev. Lett.* **75** (25), 4706 (1995). DOI: 10.1103/PhysRevLett.75.4706.

[41] "The Only Stable State of O_2^- Is the X $^2\Pi_g$ Ground State and It (Still!) Has an Adiabatic Electron Detachment Energy of 0.45 eV", K. M. Ervin,

I. Anusiewicz, P. Skurski, J. Simons, and W. C. Lineberger, *J. Phys. Chem. A* **107** (41), 8521 (2003). DOI: 10.1021/jp0357323.

[42] "High-resolution photodetachment spectroscopy from the lowest threshold of O^-", A. Joiner, R. H. Mohr, and J. N. Yukich, *Phys. Rev. A* **83** (3), 035401 (2011). DOI: 10.1103/PhysRevA.83.035401.

[43] "Gas-Phase Reactions of Transition-Metal Ions with Molecular Oxygen: Room-Temperature Kinetics and Periodicities in Reactivity", G. K. Koyanagi, D. Caraiman, V. Blagojevic, and D. K. Bohme, *J. Phys. Chem. A* **106** (18), 4581 (2002). DOI: 10.1021/jp014145j.

[44] "High-Temperature Vaporization Behavior of Oxides II. Oxides of Be, Mg, Ca, Sr, Ba, B, Al, Ga, In, Tl, Si, Ge, Sn, Pb, Zn, Cd, and Hg", R. H. Lamoreaux, D. L. Hildenbrand, and L. Brewer, *J. Phys. Chem. Ref. Data* **16** (3), 419 (1987). DOI: 10.1063/1.555799.

[45] "The Thermal and Elastic Properties of Zinc Oxide-Based Ceramics at High Temperatures", G. G. Gadzhiev, *High Temperature* **41** (6), 778 (2003). DOI: 10.1023/B:HITE.0000008333.59304.58.

[46] "Studies of the plume accompanying pulsed ultraviolet laser ablation of zinc oxide", F. Claeyssens, A. Cheesman, S. J. Henley, and M. N. R. Ashfold, *J. Appl. Phys.* **92** (11), 6886 (2002). DOI: 10.1063/1.1518782.

[47] "Simple Theoretical Estimates of the Schottky Constants and Virtual-Enthalpies of Single Vacancy Formation in Zinc-Blende and Wurtzite Type Semiconductors", J. A. Van Vechten, *J. Electrochem. Soc.* **122** (3), 419 (1975). DOI: 10.1149/1.2134226.

[48] "Mass spectrometry and photoionization studies of the ablation of ZnO: ions, neutrals, and Rydbergs", R. E. Leuchtner, *Appl. Surf. Sci.* **127–129**, 626 (1998). DOI: 10.1016/S0169-4332(97)00716-2.

[49] "The interaction of 193-nm excimer laser irradiation with single-crystal zinc oxide: Positive ion emission", E. H. Khan, S. C. Langford, J. T. Dickinson, and L. A. Boatner, *J. Appl. Phys.* **111** (6), 063101 (2012). DOI: 10.1063/1.3691939.

[50] "Insight into electronic mechanisms of nanosecond-laser ablation of silicon", W. Marine, N. M. Bulgakova, L. Patrone, and I. Ozerov, *J. Appl. Phys.* **103** (9), 094902 (2008). DOI: 10.1063/1.2903527.

[51] "Field emission study of the specificity of zinc oxide polar surfaces (0001) and $(000\,\bar{1})$. Work function and hydrogen adsorption.", J. Marien, *physica status solidi (a)* **38** (2), 513 (1976). DOI: 10.1002/pssa.2210380211.

[52] "Study of the electron kinetic processes in laser-induced breakdown of electronegative gases over an extended wavelength range", Y. E. E.-D. Gamal and M. M. Omar, *Radiation Phys. Chem.* **62** (5), 361 (2001). DOI: 10.1016/S0969-806X(01)00216-X.

[53] "Fast Imaging of Laser-induced Plasma Emission from a ZnO Target", S. Abdelli-Messaci, T. Kerdja, S. Lafane, and S. Malek, *Spectrochim. Acta B* **64** (10), 968 (2009). DOI: 10.1016/j.sab.2009.07.039.

[54] PGOPHER, a program for simulating rotational structure, version 7.1 (2010), C. M. Western, University of Bristol. URL: http://pgopher.chm.bris.ac.uk/.

[55] "An analysis of the O_2^+ $b^4\Sigma_g^-$ – $a^4\Pi_u$ First Negative band system", D. L. Albritton, A. L. Schmeltekopf, W. J. Harrop, R. N. Zare, and J. Czarny, *J. Mol. Spec.* **67** (1), 157 (1977). DOI: 10.1016/0022-2852(77)90037-6.

[56] "The near-ultraviolet and visible emission spectrum of O_2 by electron impact", C. A. Terrell, D. L. Hansen, and J. M. Ajello, *J. Phys. B: At. Mol. Opt. Phys.* **37** (9), 1931 (2004). DOI: 10.1088/0953-4075/37/9/013.

[57] "Cross Sections for Collisions of Electrons and Photons with Oxygen Molecules", Y. Itikawa, A. Ichimura, K. Onda, K. Sakimoto, and K. Takayanagi, *J. Phys. Chem. Ref. Data* **18** (1), 23 (1989). DOI: 10.1063/1.555841.

[58] "Reactions of laser-ablated Zn and Cd atoms with O_2: Infrared spectra of ZnO, OZnO, CdO, and OCdO in solid argon", G. V. Chertihin and L. Andrews, *J. Chem. Phys.* **106** (9), 3547 (1997). DOI: 10.1063/1.473441.

[59] "Dynamics of the chemiluminescent oxidation of zinc atoms by nitrous oxide", B. G. Wicke, *J. Chem. Phys.* **78** (10), 6036 (1983). DOI: 10.1063/1.444620.

[60] "Reaction of Zn^+ with NO_2. The gas-phase thermochemistry of ZnO", D. E. Clemmer, N. F. Dalleska, and P. B. Armentrout, *J. Chem. Phys.* **95** (10), 7263 (1991). DOI: 10.1063/1.461403.

[61] "Zinc oxide and its anion: A negative ion photoelectron spectroscopic study", C. A. Fancher, H. L. de Clercq, O. C. Thomas, D. W. Robinson, and K. H. Bowen, *J. Chem. Phys.* **109** (19), 8426 (1998). DOI: 10.1063/1.477505.

[62] "Revisiting the nature of the ZnO ground state: Influence of spin–orbit coupling", S. Boughdiri, B. Tangour, C. Teichteil, J.-C. Barthelat, and T. Leininger, *Chem. Phys. Lett.* **462** (1), 18 (2008). DOI: 10.1016/j.cplett.2008.06.091.

[63] "Self-similar solutions of laser produced blast waves", K. P. J. Reddy, *Pramana—J. Phys.* **46** (2), 153 (1996). DOI: 10.1007/BF02848231.

CONCLUSIONS AND FURTHER WORK

4.1 CONCLUSIONS

Despite having found quite limited application in the literature to date, time-, space-, and wavelength-resolved optical emission spectroscopy appears, based on the present results, to be a powerful tool that can contribute significantly to the analysis of laser plasma. In contrast to time-of-flight schemes (which reflect the plume composition and energetics only for $t \to \infty$), the instantaneous spatial emission profiles available using this technique provide dynamical information that can greatly facilitate an understanding of the processes governing plume formation and evolution.

Under all circumstances considered within the present work, electronically excited neutral zinc atoms were found to possess a shifted quasi-Maxwellian distribution of velocities peaking at around ≈ 2–3 km/s and with apparent temperature on the order of 10 eV. Given that the intensity of $(Zn^0)^*$ optical emission also scaled roughly with the square root of irradiance, this was understood to signify the formation of this species primarily *via* a phase explosion mechanism. The transition between the normal evaporation and phase explosion regimes was, however, not clearly discernible for a Zn target (unlike for Al[a]) since it fell below the minimum irradiance employed here ($\lesssim 1$ GW/cm^2). Despite the markedly different thermal and electronic properties of ZnO with respect to Zn, comparable $(Zn^0)^*$ emission scaling behaviour was observed also in the case of a ZnO target. Notably, the irradiance corresponding to the onset of $(Zn^0)^*$ emission (the appearance threshold) was found to be lower for ZnO (0.25 GW/cm^2) than Zn (0.39 GW/cm^2), thus ruling out a mutual origin due to normal evaporation; a spurious similarity between the two materials resulting from redeposition of Zn onto the ZnO surface therefore also appears unlikely. Rather, these observations are most probably indicative of the thermochemical decomposition of the oxide at temperatures in excess of its melting point.[b]

[a] The onset of phase explosion was clearly observable in aluminium at around 2 GW/cm^2 for 532 nm irradiation and ≈ 6 GW/cm^2 at 355 nm. Since no detailed discussion of aluminium plasma has been presented here, we provide these values for comparison only.

[b] Phase explosion occurs for $T \approx T_c$, where the critical temperature of Zn is about 3 600 K. As the thermal conductivity and volumetric heat capacity of ZnO are quite similar to the corresponding

Relative to (Zn^0)*, electronically excited Zn ions were observed with substantially greater translational kinetic energies, which moreover increased very strongly with charge state. Modal velocities were 7–8 km/s (16–21 eV) for (Zn^{1+})*; ≈ 25 and ≈ 40 km/s (≈ 200 and ≈ 550 eV) for (Zn^{2+})* produced from Zn and ZnO targets, respectively; and ≈ 40 and ≈ 50 km/s (≈ 550 and ≈ 850 eV) for (Zn^{3+})* ablated from Zn (only) under 50 mTorr of oxygen and *in vacuo*. These remarkably large energies are apparently the result of a thermal space-charge–induced dynamic acceleration process, whereby hot electrons partially escaping from the plasma form a persistent space charge layer at the expansion front and thus generate an electric field that acts on charged species present in the plume. Because the presence of multiply charged ions compensates the electron space charge, the accelerating field is maintained while sufficient thermal energy is available; very high terminal velocities can therefore be achieved on account of the prolonged common motion of the electrons and ions. It would appear from the spatial profiles presented in this work that all such acceleration occurs within the first 50 ns, and is most likely limited by the rapid cooling associated with adiabatic expansion. The introduction of ambient oxygen (which might be expected to confine the plume and thus increase the observed acceleration), however, tends to limit the maximum kinetic energy imparted due to its reactivity toward electronically excited Zn ions, thus acting to reduce the ionization degree and inhibiting the formation of a space charge layer. In addition to its direct effect during the expansion phase, the presence of oxygen (by promoting electron-ion recombination) most probably also inhibits inverse bremsstrahlung absorption and thus lessens the degree of plasma heating. This effect may also partly explain the dramatically reduced (Zn^{2+})* and (Zn^{3+})* optical emission yield under these conditions, although further experiments at different oxygen pressures and under inert gas (such as argon) are most likely necessary in order to establish the practical importance of this mechanism versus the alternative propositions of either collisional or reactive quenching. Nonetheless, it is known with certainty that IBA (specifically, rather than e.g. MPI) plays an important role in the production of the higher charge states due to their increased relative yield under longer-wavelength irradiation.

---

values for (liquid) metallic Zn, a similar temperature should be achieved in each case, which will almost certainly exceed the melting point of ZnO (≈ 2 248 K).

Results for $(Zn^{1+})^*$ suggested behaviour in some sense intermediate between that of $(Zn^0)^*$ and the higher ions, being more varied than the excited atoms with respect to target material while depending less strongly on the presence or absence of an oxygen atmosphere than $(Zn^{2+})^*/(Zn^{3+})^*$. It is clear from the velocity distributions that the mechanism of $(Zn^{1+})^*$ production at high irradiance is predominantly thermal; furthermore, the independence of the modal velocity of this species on irradiance is strongly indicative that it does not undergo (significant) dynamic acceleration and therefore is not formed in close proximity to the expansion front. Since clearly the $(Zn^{1+})^*$ velocities are Coulomb-shifted, its origin appears to be *via* a field-assisted phase explosion-type mechanism; indeed, the bimodal $(Zn^{1+})^*$ velocity distributions obtained for the ablation of a ZnO target at low irradiance provide strong evidence of both field-induced Zn^+ ion desorption and surface Coulomb explosion, with the latter being the major channel. These processes are overtaken with increasing irradiance, however, by thermochemical decomposition in the field induced by thermionic and photoelectron emission. Due to the obvious physical distinction between phase explosion of liquid Zn and surface Coulomb explosion of solid ZnO, the fact that the $(Zn^{1+})^*$ appearance threshold was similar under all conditions (Zn ablated *in vacuo*, 0.45 GW/cm^2; Zn under oxygen, 0.49 GW/cm^2; ZnO *in vacuo*, 0.42 GW/cm^2) is seemingly a matter of coincidence.

We hence arrive at a consistent overall description of laser-induced zinc and zinc oxide plasma and the corresponding ablation process. Initially, no plasma exists, and radiation is directly incident upon the target, which is thereby rapidly (super-)heated; thermo- and photoelectron emission result in the formation of a space charge layer above the surface. These electrons couple strongly to the laser field, gaining sufficient energy to collisionally ionize the sparse vapour; the nascent plasma thus formed most probably plays an important role in further target heating (particularly in the case of sub-bandgap excitation) due to its strong contribution to radiation absorption *via* inverse bremsstrahlung. At high irradiance, surface temperatures of several thousand kelvin are achieved relatively early in the laser pulse, so that Zn and ZnO approach their respective critical temperatures and undergo explosive phase transitions (whether thermochemical or purely thermodynamic). Desorption of the surface layer, which possesses a net positive charge as a result of prior electron emission, is assisted

by the electric field gradient, which may easily amount to some MV/cm; the density of the plasma is hence rapidly increased, which significantly enhances its rate of heating due to IBA, especially at the expansion front. Neutral Zn atoms, which of course are not subject to Coulomb acceleration, remain close to the target surface; the core of the plasma, which contains mostly Zn^{1+} formed by avalanche and thermal ionization, as well as electron–ion recombination of the higher ions, lies ahead of these. At moderate irradiance (several GW/cm^2), the plasma is sufficiently dense ($\approx 10^{21}$ electrons/cm^3) that it absorbs essentially all of the laser energy subsequently provided. At this stage, the space charge layer consists of hot electrons partially escaping from the plasma, with the thermally induced field producing a charge-state-dependent dynamic acceleration resulting in an essential fractionation between the various ion populations. Substantial translational kinetic energy is thus imparted to Zn^{2+} and (particularly) Zn^{3+}, although this process is self-limiting after several tens of nanoseconds due to the cooling associated with adiabatic expansion, which causes the collapse of the accelerating field. Thereafter, each component of the plume expands independently until it either impinges on a solid surface (*in vacuo*) or undergoes collisional thermalization with the surrounding medium.

4.2 SUGGESTIONS FOR FURTHER WORK

Due to time limitations, it has been impossible (or only partially possible) to perform a number of additional experiments that would either assist the interpretation of the results presented in this thesis or provide useful additional information. In the opinion of the author, further research into the current topic would benefit from attention to the following issues.

4.2.1 LINE SHAPE/INTENSITY MEASUREMENTS

It is of great importance for the understanding of laser plasma behaviour to obtain accurate measurements of the electron and ion densities and temperatures, which are quantities central to the physical description of all plasmas. In the present work these values have been only very approximately estimated, although more direct determination may be possible based on relative transition probabilities and spectral line profiles under conditions for which local thermal equilibrium (LTE) models can be considered valid. The applicability of this assumption is accepted (at least as an approximation) by many authors despite the extreme temperature, density, and

electromagnetic field gradients characterizing plasmas formed by laser ablation, with both (Saha-)Boltzmann excitation/ionization temperatures and electron densities calculated from measured Stark shifted/broadened lines commonly reported in the literature, for example by Shaikh *et al.*[1] However, Griem[2] has established conditions for the existence of LTE that suggest these diagnostics are unlikely to provide either qualitative insight or useful quantitation in the present case, especially for ions: initially the plasma is sufficiently dense, but the spatial and temporal gradients of density and temperature are too large, whereas after a period of expansion the opposite situation holds. Jonkers and van der Mullen[3] have discussed the validity of the excitation temperature in circumstances for which the ion mobility is large compared to that of the neutral species, concluding that:

> "[I]n most … helium plasmas this temperature is hardly related to any plasma quantity [and] strongly depends on the ionisation energies of the levels used [in its determination], rather than on the electron temperature. … Since due to the specific atomic structure of helium only a limited amount of excited levels can be observed, always more or less the same excitation temperature is found."

Since the Zn^0 and Zn^{1+} populations are markedly spatially separated and the first ionization potential of Zn (9.4 eV) is much smaller than that of He (24.6 eV), this discouraging appraisal most likely applies even more robustly to laser-induced Zn plasmas (and indeed those of other transition metals or their oxides). Nonetheless, it may still be of interest to examine the spatial variation in the excitation temperature of the neutral species (the physical meaning of which, however, will need to be considered carefully) and estimate the electron density near the target surface according to the Zn^0 emission line shapes. To this end, the use of these diagnostic techniques has been discussed at length by Aragón and Aguilera,[4] while Dimitrijevic and Sahal-Bréchot[5] have given Stark parameters for Zn^0. It should be noted that accurate quantitation of the $(Zn^0)^*$ spectral profiles will be hindered by the effects of collisional broadening and self-absorption due to ground-state or metastable (lowest-lying triplet) Zn atoms, and also requires the determination of the instrument function (which is itself nontrivial); high-resolution measurements of the line shifts will therefore probably be more fruitful. In principle, definitive values could be obtained for the electron temperature and density through Thomson scattering measurements, as have been performed by Nedanovska *et al.*;[6] or, alternatively, a collisional-radiative model could be constructed and the inverse problem solved,[7]

as demonstrated for laser-induced Zn plasma by O'Connell *et al*.[8] However, these are substantial undertakings and would require considerable experimental and theoretical effort prior to yielding results. Furthermore, any diagnostic method reliant on emission spectroscopy to recover absolute number densities must also consider the plasma geometry and the volumetric distribution of emitting species, as discussed in the next section.

4.2.2 PROJECTION INTEGRAL INVERSION

As the astute reader might observe, the optical emission spatial profiles presented in this thesis are in fact the projections of integrated emission intensity onto the detector image plane, and therefore do not correspond directly to the distribution of $(Zn^{n+})^*$ along the surface normal at the ablated location. The inversion of projection integrals is an ill-posed problem in general, and certain assumptions must be made about the plasma geometry in order to obtain a unique result. Most authors have chosen to assume spherical symmetry,[9] largely due to its relationship with the Abel integral, the inverse of which can be stated analytically for certain distribution functions and otherwise efficiently obtained numerically by means of the Fourier–Hankel transform.[10] More recently, Shabanov *et al.* have studied the case of an ellipsoidal plasma,[11] which corresponds to the well-known model of Anisimov *et al.*[12] for the adiabatic expansion of a laser ablation plume into vacuum. The one-dimensional images obtained in this work differ from most reports available in the literature, which concern two-dimensional data. Projections of lower dimensionality incur reduced computational effort, so that more involved geometric models may be employed, but also imply a less completely specified model and so require stronger assumptions to be made. We discuss below one possible formulation of the inverse problem and outline some unresolved difficulties in its solution.

Dribinski *et al.*[13] have provided some useful discussion, in the context of photofragment ion imaging (a technique widely used in the study of chemical reaction dynamics), of a method for Abel inversion by expansion in a basis of projection integrals of Gaussian functions. Although their presentation assumes spherical symmetry and a significantly different experimental geometry than applies to the present work, these details are not critical and we proceed in a similar fashion but considering instead the observation of a forward-biased ellipsoidal plasma

perpendicular to the direction of expansion. For measurements restricted to a plane coinciding with the central axis of the plasma, the ellipsoid reduces to an ellipse, i.e.

$$r = \frac{d}{\sqrt{\cos^2\theta + n^2 \sin^2\theta}} \qquad \text{Equation 4.1}$$

where d is the expansion distance, n is an ellipticity parameter, and r and θ are the (polar) coordinates, with the origin located at the point of ablation. Transforming this ellipse into a shell with Gaussian (radial) cross-section and $\cos^m\theta$ angular dependence,[c] we obtain:

$$\Omega(r,\theta) = \frac{\cos^m\theta}{\sigma\sqrt{2\pi}} \exp\left[-\frac{1}{2\sigma^2}\left(r - \frac{d}{\sqrt{\cos^2\theta + n^2\sin^2\theta}}\right)\right]^2$$

Equation 4.2

with σ being the shell thickness. Ω should be normalized for any given d (i.e., each shell should contain an equal quantity of material); this can be done exactly in r, but not in θ, giving a normalization factor of:

$$\begin{aligned} N(d;n;m) &= \int_{-\pi/2}^{\pi/2} d\theta \int_0^\infty dr\, \Omega(r,\theta) \\ &= \int_0^{\pi/2} \cos^m\theta \left[1 + \operatorname{erf}\left(\frac{d}{\sigma\sqrt{2\cos^2\theta + 2n^2\sin^2\theta}}\right)\right] d\theta \end{aligned}$$

Equation 4.3

where the remaining integral is tractable only for $n = 1$ and $m = 0$ (corresponding to the spherical case) and must be calculated numerically otherwise.[d]

[c] The relationship between m and θ_{FWHM} is $m = \log 2/(\log \sec \theta_{FWHM})$, or $\theta_{FWHM} = \operatorname{arcsec}(\sqrt[m]{2})$.

[d] A perturbative solution was attempted by Taylor expansion around the spherical solution, but the resulting series is not analytic (the terms diverge with alternating signs). Alternative approaches, such as expansion in a different basis, or the use of Padé approximants, might prove more successful.

Transforming Equation 4.2 into Cartesian coordinates, with z being the axis along the target surface normal and x that along the direction of observation, we have

$$\hat{\Omega}(z,x) = \Omega\big(r(z,x),\theta(z,x)\big)\begin{vmatrix} \partial r/\partial z & \partial r/\partial x \\ \partial\theta/\partial z & \partial\theta/\partial x \end{vmatrix}$$
$$= \Omega\left(\sqrt{z^2+x^2}, \arccos\left\{\frac{z}{\sqrt{z^2+x^2}}\right\}\right)\left|\frac{1}{\sqrt{z^2+x^2}}\right|$$

Equation 4.4

(where the explicit expression in terms of z and x is omitted for brevity). The normalized projections of $\hat{\Omega}$ along x, i.e. the basis functions, are then given by:

$$\beta(z;d;n;m) = 2\int_0^\infty \hat{\Omega}(z,x)dx \Big/ N(d;n;m) \qquad \text{Equation 4.5}$$

which is integrated numerically for values of z running over the extent of the image, with σ chosen according to the spatial resolution; that is, the complete basis matrix $\mathbf{B}(n;m)$ is given by the outer product

$$\mathbf{B}(n;m) = \beta(d\times z;n;m) : \{\beta(d_i;z_j;n;m) \mid d_i \in d, z_j \in z\}.$$

Equation 4.6

Since these expressions alone may not provide adequate geometric insight, we present as Figure 4.1 a plot over part of the half-space $x = 0 \rightarrow \infty$ of some values of $\hat{\Omega}$ with the corresponding projections β.

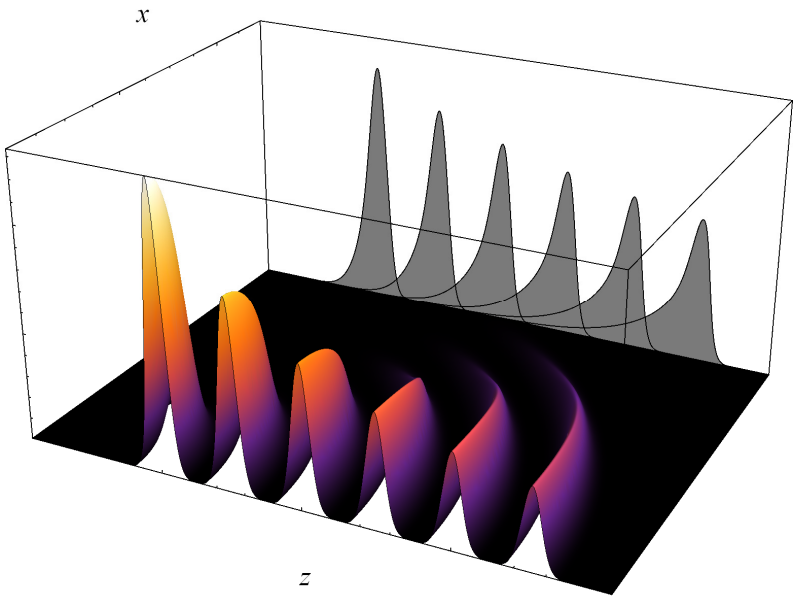

Figure 4.1: elliptical shells Ω and their projections β for $n = 3$ and $m = 50$ ($\theta_{FWHM} = 30°$) plotted for six different values of d.

Inversion of the image data (i.e., transformation from z- into d-space) is now straightforward, and can be accomplished (for example) by means of the singular value decomposition $\mathbf{B}(n;m) = \mathbf{U}\,\mathrm{diag}(\Sigma)\,\mathbf{V}^{\mathrm{T}}$, with diag($\Sigma$) the diagonal matrix of the singular values. The inverted image is then found as:

$$I(d) = I(z)\,\mathbf{V}\,\mathrm{diag}[\Sigma_i / (\Sigma_i^{\,2} + q^2)]\,\mathbf{U}^{\mathrm{T}} \qquad \text{Equation 4.7}$$

where q is a regularization parameter (Tikhonov factor) used to improve the condition number of the inverse problem and thus the robustness of its solution to noise. An example of the result of this procedure is given below.

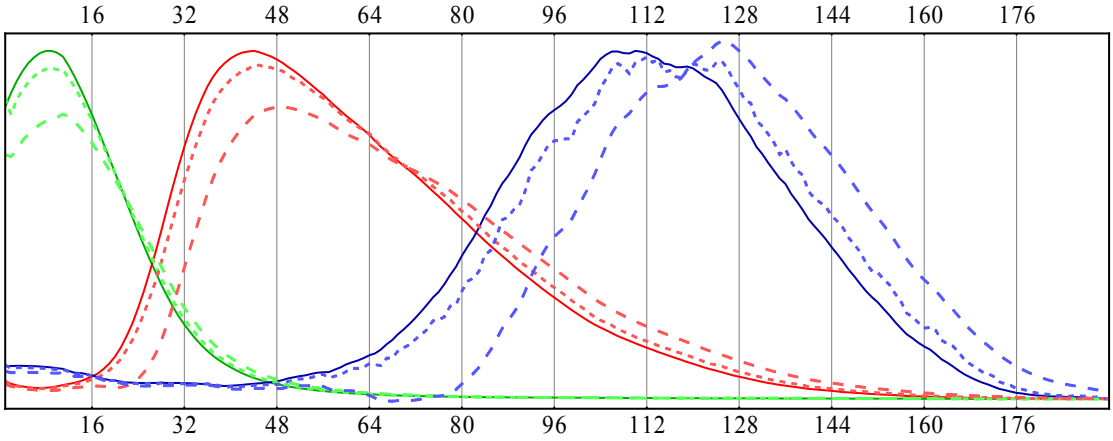

Figure 4.2: spatial profiles for (Zn^{0})* (green), (Zn^{1+})* (red), and (Zn^{2+})* (blue), where the curves for each species have been independently normalized prior to inversion. Solid lines are the measured profiles; dashed lines are the profiles in *d*-space transformed using Anisimov bases constructed for $n = 2$ and $m = 50$ (short dashes) and $n = 3$ and $m = 25$ (long dashes). The horizontal scale is pixel number.

Figure 4.2 demonstrates the central difficulty associated with the present approach: the *d*-space profiles depend sensitively on the geometric parameters used in the construction of the basis, reasonable values for which are far from obvious. For $n = 2$ and $m = 50$, only minor differences are apparent between the measured and inverted data, while with $n = 3$ and $m = 25$, the spatial profile of (Zn^{2+})*, in particular, is strongly shifted to the right and possesses a larger area relative to those of (Zn^{0})* and (Zn^{1+})*.[e] Additionally, it is plausible that the expansion geometry is species- (and possibly time-) dependent, which will further complicate the choice of a suitable basis. We may nonetheless conclude with certainty that the expansion is not (hemi)spherically symmetric, since such an assumption yields unphysical negative intensities for the leftmost part of the transformed (Zn^{1+})* and (Zn^{2+})* profiles in which no optical emission is observed. Thus, although decomposition in an Anisimov basis is clearly an improvement (in the sense of flexibility and, potentially, representational accuracy) over the commonly applied Abel inversion techniques, further work is required in order to ensure the quantitative correctness of the approach. As a result, the spatial profiles presented in this work have been given as measured (i.e., in *z*-space), despite that this is most likely not strictly correct, in order to avoid arbitrariness in their interpretation. Furthermore, it is worth emphasizing that

[e] The reason for the shift is obvious, but it should also be noted that the scaling is a necessary and physically meaningful consequence of the normalization of the basis functions.

the above formulation of the problem does not consider the possibility of an optically thick plasma, which will require the use of modified basis functions, and more generally, the method developed here is merely one possible (fairly simple) means to its solution that should not be considered either necessary or authoritative.

4.2.3 TIME-OF-FLIGHT MEASUREMENTS

Owing to time constraints, it has not been possible to supplement the optical emission measurements presented here with ion yield/time-of-flight data obtained under equivalent conditions. This comparison would be particularly valuable in case the species monitored spectroscopically (which possess substantial electronic excitation that is also strongly increasing with charge state) are not representative of the bulk of the ablated material in their relative abundance or distribution of velocities. The response of typical ion detectors (channel electron multipliers) is relatively uniform toward all charged particles, so that ion yields measured in this fashion will be more representative of the ablation plume composition than (uncalibrated) optical emission yield, and absolute kinetic energy distributions are readily obtained from the temporal variation of ion current.[f] Furthermore, since the energy distribution of prompt electrons may be measured directly by this method, such measurements may assist in the elucidation of the mechanism by which the plasma initially becomes electrically polarized and the behaviour of the higher charge states, for which we propose a space-charge–mediated dynamic acceleration process. Amoruso *et al.*[14] have previously reported the results of such an experiment for Al, while Yakovlev and Fedorov[15] and Deng and Eberly[16] have provided theoretical accounts of how prompt electrons might obtain strongly hyperthermal translational energies, through the formation of a layer of enhanced electron density at metallic surfaces under laser irradiation and by above-threshold ionization, respectively.

[f] However, since this approach does not provide species resolution, care should be taken in the interpretation of the resulting data. In particular, it is more difficult to deal with the effect of electron-ion recombination, as observed e.g. for Zn^{1+} in the 355 nm ablation of Zn under oxygen, without the ability to distinguish the parent from the product ion. For this reason, and also because of the loss of dynamical information when the plume is observed only in its final state, results obtained through optical emission and ion time-of-flight experiments should be taken as complementary.

In addition to time-of-flight experiments, which can be accomplished only *in vacuo* or under very low background pressure if collisional losses are to be avoided, Langmuir probe measurements might also fruitfully be undertaken in order to gain a fuller understanding of the interaction of the laser plasma with the ambient medium. This may be especially important under conditions for which an ionization shock is formed, since the latter will most likely represent the primary mode of ion transport to the deposition substrate when the mean free path is small and a reactive process gas is employed. It is probably reasonable in such a case to assume that, several microseconds after ablation, nonequilibrium dynamical effects no longer dominate, so that the electron/ion density and temperature within the residual plasma may meaningfully be probed and the kinetics governing thermalization and recombination processes investigated. Such information would contribute significantly to understanding of pulsed laser deposition scenarios, of which even a comprehensive account of plume evolution within the first ≈ 100 ns is not fully descriptive. Ding *et al.* have performed Langmuir probe measurements of a recombining laser plasma,[17] and confirm that, with appropriate attention to the movement of the Debye sheath, the time-varying ion density can accurately be quantified under these circumstances.

4.2.4 ADDITIONAL LASER WAVELENGTHS

Since the present work has been limited for practical reasons to two wavelengths (i.e., 355 and 532 nm), further experiments employing a wider range of photon energies are probably worthwhile. Ablation with multiple wavelengths simultaneously (e.g., the unseparated Nd:YAG harmonics) might also be worth pursuing in case of the existence of synergistic effects, although interpretation of the results of such experiments may be challenging.

Laser radiation can readily be obtained at 266 and 1064 nm ($\hbar\omega$ = 4.66 and 1.17 eV), both of which may be expected to provide useful additional information by permitting diagnosis of competing phenomena *via* the known wavelength scaling laws for each process. The principal effects likely to be distinguishable by this means are multiphoton and inverse bremsstrahlung (IB) absorption, which depend inversely on wavelength; the former is expected to dominate at 266 nm and the latter at 1064 nm. According to a theoretical study by Bogaerts and Chen,[18] these (along with photoionization of electronically excited species) together represent the major

absorption mechanisms. However, the IBA cross-section also depends on the plasma density and temperature, and these parameters are themselves both nonstationary in time and space and vary with wavelength, so that the situation is rather complicated in practice. (Furthermore, at high density and temperature, as in the nascent plasma, nonlinear effects such as multiphoton IBA should be considered.) Therefore, if feasible, absorbance studies employing a consistently generated ablation plume may prove valuable in disambiguating the complex interdependence between the absorption processes and the plasma state variables. The use of a tuneable probe laser would additionally enable species in their electronic ground states to be excited and subsequently detected by optical emission, or the effect of resonant absorption and/or stimulated emission to be investigated.

4.2.5 ABLATION IN AN ELECTRIC FIELD

Given the importance of early polarization, and later the thermally induced self-field, in determining the properties and evolution of laser plasmas, it is somewhat surprising that few reports exist of ablation plume behaviour in the presence of an external (applied) electric field. For the purposes of the present work, both the target and the surrounding environment (i.e., the vacuum chamber) have been held at ground potential as a matter of convenience, although in principle an arbitrary (static or time-varying) bias of either polarity could be applied. By symmetry, the induced field has its major axis parallel to the target surface normal; it could thus be altered self-consistently by means of a planar electrode placed behind the target, given a sufficiently small dielectric constant of the latter and provided that the laser plasma was produced far enough from the edge that field curvature could be neglected. In this way, if Debye screening does not dominate, the total electric field could readily be augmented or diminished (or, indeed, completely cancelled or reversed) relative to the case studied here; and if plasma shielding is significant, such experiments might provide a reasonably straightforward means to the quantitation of its influence.

Control over the plasma field strength or polarity would permit further investigation of several dynamical effects that remain poorly understood, especially if a bias was applied only during either initial irradiation or the subsequent expansion. In particular, the mechanism of initial electric polarization is still somewhat uncertain, since space charge effects are expected to limit electron emission due to both thermal and

multiphoton ionization, but according to Wendelen *et al.*[19] these should be distinguishable from their scaling with irradiance otherwise. Furthermore, the influence of electron-ion recombination is unclear in general, with unambiguous evidence of this process observed in the present work only in the presence of O_2 at relatively high (≥ 100 mTorr) background pressure. Clearly, the probability of recombination is related to the degree to which electrons and ions are spatially collocated, and thus to the extent of thermal charge separation, an electrostatic barrier to (or enhancement of) which could be imposed in order to study its effect on the relative yields of different species. Moreover, the inferred space charge-mediated dynamic acceleration of ions is evidently (strongly nonlinearly) charge state–dependent; furthermore, if this process has been assigned correctly, there should exist a specific bias potential for which the modal kinetic energy of each species is maximized. It would therefore be of considerable interest to examine the variation of the ion energies under modification of the ordinary thermally generated electric field.

Because of the consistent orientation of the induced field for unperturbed laser plasmas produced in field-free conditions, few observations have been made of negative ions subsequent to laser ablation, even for target materials containing electronegative elements. Although these are almost certainly present, as in other plasma sources, they likely represent a minor and transient contributor to the overall composition of the plume, at least *in vacuo*, due to their experiencing a backward acceleration (in the moving frame of the expanding plume), which presumably leads to rapid recombination with ions of the more electropositive species. Esposito *et al.*[20] and Peláez *et al.*[21] have reported persistent O^- ions in the ablation of metal oxides under either N_2O or O_2, but ascribe this to electron capture by O atoms produced in the dissociation of the ambient gas rather than the observation of a primary ablation product. If it is possible to observe enhanced negative ion yield *via* a direct mechanism (or to constructively perturb the plasma composition and energetics in general) through ablation in an externally applied electric field, this may prove valuable both as an additional means of probing the physics of the plasma and in the context of pulsed laser deposition process control.

4.3 REFERENCES

[1] "Measurement of electron density and temperature of a laser-induced zinc plasma", N. M. Shaikh, B. Rashid, S. Hafeez, Y. Jamil and M. A. Baig, *J. Phys. D: Appl. Phys.* **39** (7) 1384 (2006). DOI: 10.1088/0022-3727/39/7/008.

[2] "Validity of Local Thermal Equilibrium in Plasma Spectroscopy", H. R. Griem, *Phys. Rev.* **131** (3), 1170 (1963). DOI: 10.1103/PhysRev.131.1170.

[3] "The excitation temperature in (helium) plasmas", J. Jonkers and J. A. M. van der Mullen, *J. Quant. Spectrosc. Radiat. Transfer* **61** (5), 703 (1999). DOI: 10.1016/S0022-4073(98)00059-4

[4] "Characterization of laser induced plasmas by optical emission spectroscopy: A review of experiments and methods", C. Aragón and J. A. Aguilera, *Spectrochim. Acta B* **63** (9), 893 (2008). DOI: 10.1016/j.sab.2008.05.010.

[5] "Stark broadening of neutral zinc spectral lines", M. S. Dimitrijević and S. Sahal-Bréchot, *Astron. Astrophys. Suppl. Ser.* **140** (2), 193 (1999). DOI: 10.1051/aas:1999417.

[6] "Investigation of magnesium laser ablated plumes with Thomson scattering", E. Nedanovska, G. Nersisyan, C. L. S. Lewis, and D. Riley, *Laser and Particle Beams* **30** (2), 259 (2012). DOI: 10.1017/S0263034612000018.

[7] "Experimental verification of a radiative model of laser-induced plasma expanding into vacuum", I.B. Gornushkin, A.Ya. Kazakov, N. Omenetto, B.W. Smith, and J.D. Winefordner, *Spectrochim. Acta B* **60** (2), 215 (2005). DOI: 10.1016/j.sab.2004.11.009.

[8] "Early stage optical emission in nanosecond laser ablation", G. O'Connell, I. Tobin, and J. G. Lunney, *Appl. Phys. A* **110** (3), 731 (2013). DOI: 10.1007/s00339-012-7226-6.

[9] "Abel inversion applied to a transient laser induced plasma: implications from plasma modeling", I. B. Gornushkin, S. V. Shabanov, and U. Panne, *J. Anal. At. Spectrom.* **26** (7), 1457 (2011). DOI: 10.1039/C1JA10044K.

[10] "Modified Fourier–Hankel method based on analysis of errors in Abel inversion using Fourier transform techniques", Shuiliang Ma, Hongming Gao, and Lin Wu, *Appl. Optics* **47** (9), 1350 (2008). DOI: 10.1364/AO.47.001350.

[11] "Radiation from asymmetric laser-induced plasmas collected by a lens or optical fiber", S. V. Shabanov, I. B. Gornushkin, and J. B. Winefordner, *Appl. Optics* **47** (11), 1745 (2008). DOI: 10.1364/AO.47.001745.

[12] "Gas dynamics and film profiles in pulsed-laser deposition of materials", S. I. Anisimov, D. Bäuerle, and B. S. Luk'yanchuk, *Phys. Rev. B* **48** (16), 12076 (1993). DOI: 10.1103/PhysRevB.48.12076.

[13] "Reconstruction of Abel-transformable images: The Gaussian basis-set expansion Abel transform method", V. Dribinski, A. Ossadtchi, V. A. Mandelshtam, and H. Reisler, *Rev. Sci. Instrum.* **73** (7), 2634 (2002). DOI: 10.1063/1.1482156.

[14] "Emission of prompt electrons during excimer laser ablation of aluminum targets", S. Amoruso, M. Armenante, R. Bruzzese, N. Spinelli, R. Velotta, and X. Wang, *Appl. Phys. Lett.* **75** (1), 7 (1999). DOI: 10.1063/1.124259.

[15] "The Influence of the Surface Electron Layer on the Energy Spectrum of Photoelectrons", M. A. Yakovlev and M. V. Fedorov, *J. Exper. Theor. Phys.* **95** (4), 705 (2002). DOI: 10.1134/1.1520602.

[16] "Multiphoton absorption above ionization threshold by atoms in strong laser fields", Z. Deng and J. H. Eberly, *J. Opt. Soc. Am. B* **2** (3), 486 (1985). DOI: 10.1364/JOSAB.2.000486.

[17] "Effects of rapidly decaying plasmas on Langmuir probe measurements", G. Ding, J. E. Scharer, and K. L. Kelly, *J. Appl. Phys.* **84** (3), 1236 (1998). DOI: 10.1063/1.368189.

[18] "Effect of laser parameters on laser ablation and laser-induced plasma formation: A numerical modelling investigation", A. Bogaerts and Z. Chen, *Spectrochim. Acta B* **60** (9–10), 1280 (2005). DOI: 10.1016/j.sab.2005.06.009.

[19] "Space charge corrected electron emission from an aluminum surface under non-equilibrium conditions", W. Wendelen, B. Y. Mueller, D. Autrique, B. Rethfeld, and A. Bogaerts, *J. Appl. Phys.* **111** (11), 113110 (2012). DOI: 10.1063/1.4729071.

[20] "Negative ions: The overlooked species in thin film growth by pulsed laser deposition", M. Esposito, M. Bator, M. Döbeli, T. Lippert, C. W. Schneider, and A. Wokaun, *Appl. Phys. Lett.* **99** (19), 191501 (2011). DOI: 10.1063/1.3660399.

[21] "Relevance and formation mechanisms of negative ions upon ablation of Al_2O_3", R. J. Peláez, C. N. Afonso, J. Chen, M. Esposito, T. Lippert, D. Stender, and A. Wokaun, *J. Phys. D: Appl. Phys.* **45** (28), 285402 (2012). DOI: 10.1088/0022-3727/45/28/285402.